Advanced Nanostructured Concepts in Solar Cells using III-V and Silicon-Based Materials

by

Som Nath Dahal

A Dissertation Presented in Partial Fulfillment
of the Requirements for the Degree
Doctor of Philosophy

Approved July 2011 by the
Graduate Supervisory Committee:

Christiana Honsberg, Chair
Stephen Goodnick
Ronald Roedel
Fernando Ponce

ARIZONA STATE UNIVERSITY

August 2011

ABSTRACT

As existing solar cell technologies come closer to their theoretical efficiency, new concepts that overcome the Shockley-Queisser limit and exceed 50% efficiency need to be explored. New materials systems are often investigated to achieve this, but the use of existing solar cell materials in advanced concept approaches is compelling for multiple theoretical and practical reasons. In order to include advanced concept approaches into existing materials, nanostructures are used as they alter the physical properties of these materials. To explore advanced nanostructured concepts with existing materials such as III-V alloys, silicon and/or silicon/germanium and associated alloys, fundamental aspects of using these materials in advanced concept nanostructured solar cells must be understood. Chief among these is the determination and predication of optimum electronic band structures, including effects such as strain on the band structure, and the material's opto-electronic properties.

Nanostructures have a large impact on band structure and electronic properties through quantum confinement. An additional large effect is the change in band structure due to elastic strain caused by lattice mismatch between the barrier and nanostructured (usually self-assembled QDs) materials. To develop a material model for advanced concept solar cells, the band structure is calculated for single as well as vertical array of quantum dots with the realistic effects such as strain, associated with the epitaxial growth of these materials. The results show significant effect of strain in band structure. More importantly, the band diagram of a vertical array of QDs with different spacer layer thickness show significant

change in band offsets, especially for heavy and light hole valence bands when the spacer layer thickness is reduced. These results, ultimately, have significance to develop a material model for advance concept solar cells that use the QD nanostructures as absorbing medium.

The band structure calculations serve as the basis for multiple other calculations. Chief among these is that the model allows the design of a practical QD advanced concept solar cell, which meets key design criteria such as a negligible valence band offset between the QD/barrier materials and close to optimum band gaps, resulting in the predication of optimum material combinations.

ACKNOWLEDGMENTS

First of all, I would like to thank my advisor, Dr. Christiana Honsberg, for her support, guidance and encouragement until I earned my Ph.D. I, indeed, appreciate her for her guidance on making plans and executing those throughout my work. It has been my great honor and privilege working with her. Additionally, I would also like to thank other committee members, Dr. Stephen Goodnick, Dr. Ronald Roedel and Dr. Fernando Ponce for their time and consideration on my thesis. I am grateful to Dr. Stuart Bowden for his guidance on silicon solar cell fabrication and characterization. I would like to acknowledge Prof. Henry Glyde at the Department of Physics and Astronomy, University of Delaware, Newark, DE for being my co-advisor for the time being when I started working with Dr. Honsberg.

I want to acknowledge Dr. Nikolai Faleev, Dr. Clarence Tracy and Mr. William Dauksher for their help and guidance on materials and device characterization of III-V alloys and silicon based devices for solar cells.

I would like to acknowledge Dr. Keun-Yong Ban and Kunal Ghosh at solar power laboratory (SPL) as brilliant colleagues. I benefited many things from their deep understanding of experimental procedures and solar cell device physics. I want to acknowledge Dr. Stephen Bremner who helped me understand the advanced nanostructured concepts in solar cells with useful discussions. In addition; I want to thank Adam Bailey and Jongwon Lee, at SPL in Arizona State University. I am grateful to brilliant colleagues Mr. Sean Jacobs, Dr.

Balakrishnam Jampana and Dr. Michael Levy in Solar Power Program back in University of Delaware.

Especially, I would like to thank my parents and parents- in-law back in Nepal. I could not get my degree done without their endless support, encouragement and their affection. Finally, this work wouldn't be complete without patience and love of my wife Rameshwari Ghimire and my daughters Sushin and Udayaa.

TABLE OF CONTENTS

Page

CHAPTER Page

LIST OF TABLES

LIST OF FIGURES

Figure Page

Chapter 1

INTRODUCTION

1.1 Motivation

The world total energy consumption is expected to rise by 50% in the next three decades from 500 quadrillion (10^{15}) British thermal unit (BTU) to 750 Quadrillion BTU in 2035 [1]. Most of the energy demand is met by burning oil and coal, which emit tremendous amounts of greenhouse gases. To solve the energy demand and the energy-related environmental and social crises, the renewable share of the energy production and consumption need to be ramped up. In the US, only about 8% of the total energy consumption is supplied from renewable sources and out of that, only 0.02% is the contribution of solar photovoltaic (PV) [2]. Despite the tremendous amount of energy falling on the earth's surface as solar radiation (~1 kW/m^2), the share of solar electricity is almost negligible in world energy consumption due to comparatively higher price of solar generated electricity.

A key element in increasing the viability of photovoltaics (PV) is to increase its efficiency. A higher efficiency technology can improve the cost of electricity (COE in $/kWh) by reducing several cost components of a photovoltaic system. In a higher efficiency system, solar cell material costs are reduced since a higher efficiency technology produces more power per gram of material; area-related material costs (such as glass, encapsulation materials, etc) become lower since fewer of these materials are needed for the same amount of power; and area-related balance of system costs (including wiring, installation, land area,

mounting structures, etc), are substantially reduced as a smaller system area is needed for the same power. The reduction of these costs has a dramatic impact of PV costs. For example, in single junction crystalline silicon solar cells, about 50% cost of the solar electricity comes from that of wafer. While thin film technologies have a lower $/W cost, the lower efficiencies in thin film devices mean that the cost of electricity (COE) is similar to silicon technologies. Further, at present efficiencies, module costs comprise a substantial cost component, and because cost reductions in glass are unlikely, cost reduction via increased efficiency are compelling. A solar cell with less material and high efficiency always drives to the low price in the long run. To generate solar electricity that is cost competitive with other forms of energy, new approaches to increase efficiency are needed.

From detailed balance calculations[3,4,5], efficiency is inherently linked to the existence of materials that have not only ideal band gaps but also electronic properties (minority carrier diffusion length, absorption, etc.) that allow high collection and open circuit voltages (V_{oc}). Tandem solar cells require multiple such materials. The higher the number of materials with optimum band gaps, the higher the theoretical efficiency. Triple junction solar cells are hitting material-related restrictions in efficiency due to the lack of lattice-matched materials with optimum band gaps. This leads to the search for either new materials (e.g., InGaN), new substrates (e.g., bonded layer approaches), or the use of nanostructures to change the electronic properties.

The dependence of efficiency on number of materials with optimum band gaps may be circumvented by using advanced concepts such as multiple exciton generation [6], hot carrier [7] and intermediate bands [5].These approaches require either entirely new materials or nanostructure approaches. The attempts to find new "bulk" materials with optimum band gaps for some of these concepts, particularly intermediate band solar cells, result in suggestions of complex oxides [8] and/or transition metal complexes [9]. While such new materials may be appropriate for longer-term approaches, the entry of new materials in to the PV industry has historically been slow and the large infrastructure embedded in the large existing production lines is likely to provide an additional barrier to the rapid uptake of new materials. Consequently, a critical need for a path to higher efficiencies is to use nanostructures consisting of materials that are compatible with current fabrication technology and infrastructures.

Nanostructures from existing materials such as III-V and their alloys, silicon and germanium can be tuned to have proper band gaps and material properties (e.g., band structure, absorption, etc.) as required by the detailed balance calculations. In addition to this, already matured processing technology of silicon germanium alloys and the success of III-V nanostructures in light emitting diode (LED) and laser devices indicate that these materials are viable for advanced nanostructure concepts in solar cells.

The realization of ultra high efficiency solar cells from nanostructured materials depends critically on the ability to design nanostructures and predict

optimum performance on nanostructured solar cells. This work addresses fundamental issues in the design of such nanostructured solar cells. Specifically, the work develops the framework that allows the identification of optimum material/nanostructure combinations taking into account realistic impacts on band structure, particularly strain-related effects. The goal is to find material combinations (quantum dot/barrier materials), which, taking into account realistic effects such as strain, quantum dot shape and size, give efficiencies as close as possible to the ideal intermediate band solar cell, which has an efficiency of 63.2% under maximum concentration[5]. This is accomplished by calculating the quantum dot (QD) band structure for every tertiary material combination of common III-V materials, under strained growth or relaxed growth conditions, on available substrates (GaAs, InP, InAs, etc), and then calculating the detailed balance efficiencies for this band structure.

The work presented here is focused strongly on quantum dot materials, primarily for intermediate band approaches but the approach and the calculation methodology developed here can also be applied for nanostructured tandems, multiple exciton generation and hot carrier solar cells. The following sections provide an overview of the how cost is a driver in the development of ultra-high efficiency solar cells, followed by an overview of approaches which can be used to realize such high efficiencies. The last section in Chapter 1 overviews the steps necessary to achieve the goal of the thesis and the first step in the realization of such efficiencies via nanostructures – namely the development of the tools to

identify optimum materials for a given approach - and its application to intermediate band solar cells.

1.2 Importance of efficiency

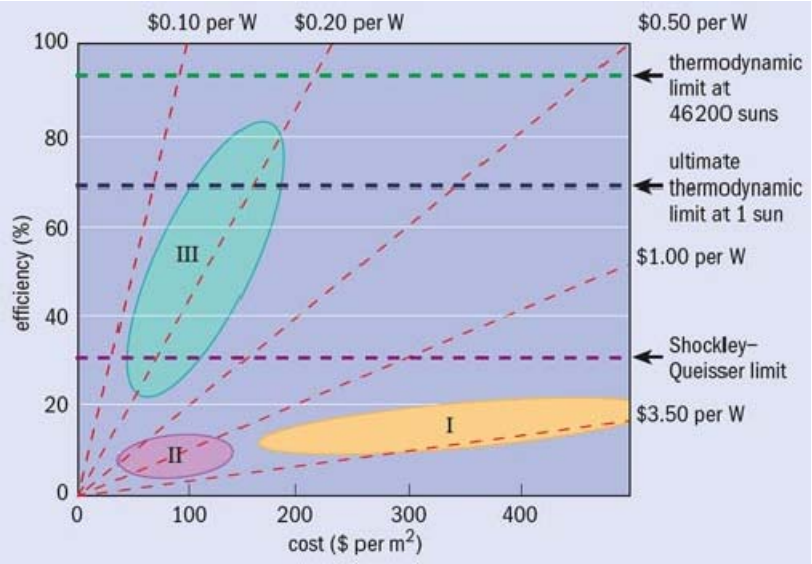

Fig. 1.1 Efficiency vs. cost for the three different generations of solar cells [10]

Photovoltaic technology is often divided into several groupings (also called generations) [10]. The maximum efficiency of the first generation single junction crystalline silicon solar cells (in laboratory) has been reported to be 24.7%, [11] which is 85% of its maximum attainable efficiency (29.8%) at AM1.5 [12].The second generation technologies that contain thin film solar cells can offer comparatively lower material related costs with lower efficiency, as shown in Fig.1.1. The third generation concepts, whose focus is on high efficiency, can be obtained either with series of stack of single junction devices to match the energy of photons in solar radiation (e.g., tandems) or with the implementation of

nanostructures and the quantum mechanical phenomena associated with them [13].

From the approximate analysis of efficiency vs. cost of the three different technologies (single junction silicon (I), thin film(II) and advanced concept(III) solar cells [10]), shown in Fig.1.1, it is clear that the third generation devices made from advanced technologies and materials promise high efficiency at low cost. The efficiency enhancement in next generation advanced concept devices comes from the loss minimization related to single junction solar cells.

1.3 Efficiency limit and loss mechanisms in single junction solar cells

The efficiency of single junction solar cell is limited by different loss mechanisms as shown in Fig.1.2. Solar spectrum contains photons with energy range of about 0.5 eV to 3.5 eV. Out of these, photons with energy less than the band gap are not absorbed by the material, while high energy photons lose their energy as heat when the excited carrier relax to band edge (labeled as 1 and 2 respectively, in Fig.1.2). These two effects alone limit the conversion efficiency of single junction solar cell to 44% (AM 1.5G, maximum concentration). Loss mechanisms of type 4 and 5 (Fig.1.2) are inevitable in single junction solar cells.

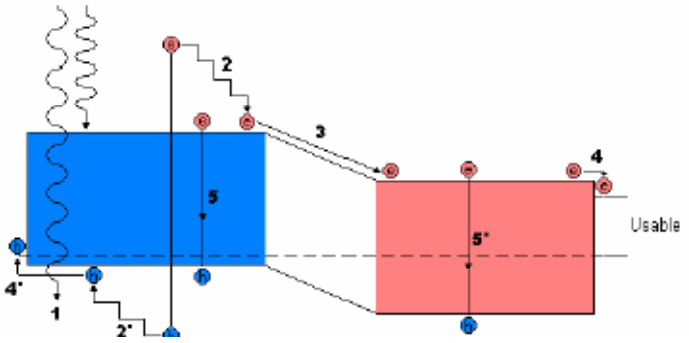

Fig 1.2 Major loss processes in single junction solar cells (1) loss of low energy photons, (2) thermalization loss of high energy photons, (3) voltage loss at the junction, (4) contact voltage loss.

Despite the fact that the theoretical efficiency of single junction devices (AM 1.5 including Auger recombination and free carrier absorption) is limited to 29% [12], due to abundance of raw materials to produce silicon on earth's crust; it's interesting physical properties such as the band gap being close to the optimum value, comparatively easy doping to get both n- and p-type materials; and the mature processing technology in microchip industry, the commercial market of the solar cells is dominated by single junction silicon technology. However, since silicon is an indirect band gap material, the thickness of the device has to be relatively high to absorb significant fraction of above band gap photons without well designed light trapping techniques. The advanced concept devices with nanostructures use less material, which saves the material related cost.

The goal of third generation solar cells is to overcome the Shockley-Queisser limit [14], ultimately reaching the maximum thermodynamic limit in

efficiency of 70% at one sun and 86% under maximum concentration. Realization of some of the advanced concept solar cells with the potential efficiencies greater than 50% rely on nanostructures. Short overviews of these high efficiency devices/concepts with the significance of nanostructures are briefly presented in the following section.

1.4 High efficiency solar cells

Approaches to achieve high efficiency solar cells rely on the ideas that overcome the Shockley-Queisser limit by avoiding the energy loss of high energy photons (labeled as 2 and 2' in Fig.1.2) and absorbing the photons that have energy lower than the band gap (labeled as 1 in Fig.1.2). One way to minimize the energy loss of high-energy photons without losing low energy photons is the use of a stack of single junction solar cells with different band gaps. On the other hand, in advanced concept devices such as hot carrier and multiple exciton generation solar cells, the energy loss of electron hole pairs generated by high energy photons can be suppressed and utilized either to enhance the photo voltage or to enhance the photocurrent. The enhancement in photocurrent in comparison to single junction device can be achieved by utilizing energy lost in the relaxation process to generate two or more electron hole pairs whereas the enhancement in photo voltage can be achieved by collecting the high energy carriers before they relax to the band edges. In addition to this, the loss of photons with energy less than the band gap can be avoided by using a material which has an intermediate band located in between the conduction and valence band of a semiconductor. All of these approaches require suppressed carrier relaxation rate which can be

achieved in nanostructures. In the following subsections, the author discusses the high efficiency approaches which require nanostructures either as absorbing or as transport medium with emphasis on multiple transition solar cells which is the main component of this dissertation.

1.4.1 Multijunction Solar cells

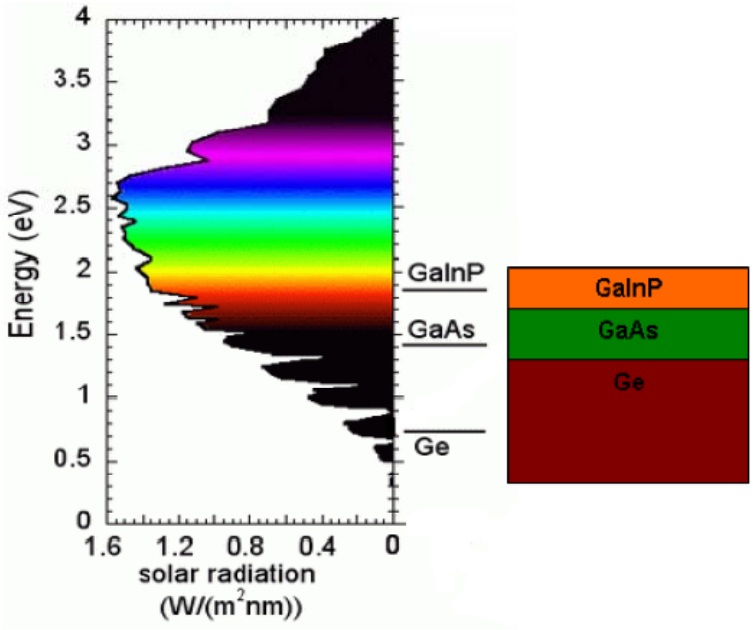

Fig. 1.3 Schematic of triple junction solar cell

The theoretical detailed balance efficiency of a three junction tandem solar cells is 52% at one sun (63% for maximum concentration) [15] and the highest recorded three junction tandem efficiencies are 42.3% at 406 suns (AM1.5D) [16] and 43.5% at 418 suns [17]. The most common triple junction solar cells are lattice matched structure containing Ge as the bottom cell with GaAs in the middle and GaInP as the top cell as shown in Fig. 1.3. The major limiting factor

to get the triple junction solar cells with efficiencies higher than the reported values is the availability of the materials that are lattice matched to the common substrates that are used to fabricate these cells. The material that have optimum band gap combinations obtained from detailed balance calculations are not lattice matched to the substrate and the strain due to lattice mismatch in these structures leads to defects causing the degradation in cell performance. However, the self-assembled quantum dots of III-V materials, which have strain modified band gaps can fill in the gaps of the materials to achieve the efficiency close the optimum.

Also, as the triple junction technology is reaching efficiency close to 45%, multijunction devices with four and five junctions are getting attention of researchers all around the world. The detailed balance efficiency calculations indicate the need of 1 eV materials for monolithic (current matched) four and five junction devices [4]. For example, for future generation monolithic tandem solar cells, the lattice mismatch between the higher band gap materials grown at the top of the lower band gap materials causes significant defect density resulting in the degradation in the efficiency of the overall device. To overcome the issues related to the availability of lattice matched 1 eV materials in four and five junction current matched tandem solar cells, a lattice mismatched or metamorphic growth is a viable option. In this case, nanostructured self-assembled quantum dots [18] and quantum wells [19,20] that have thickness/size tunable band gaps can be useful for spectral tuning.

1.4.2 Multiple exciton generation solar cells

In multiple exciton generation solar cells, the electron-hole pairs generated by the photons with energy at least two times the band gap release their extra energy to generate other excitons. This phenomenon, also called as impact ionization [21], is responsible for multiple exciton generation. The limiting efficiency of a solar cell working under this principle is 85.9% for the band gap of 48 meV [6] under maximum concentration of AM0 solar spectrum and 44% at 1 sun for E_G =0.735 eV [10,22]. In bulk materials, due to the requirement of crystal momentum conservation together with energy conservation, the threshold energy for the impact ionization is higher than that required by the energy conservation alone. For example in bulk silicon the total quantum yield of only 125% was obtained for a photon of energy 4.8 eV [23]. Furthermore, the rate of impact ionization has to compete with the rate of carrier relaxation by electron-phonon scattering. To obtain the meaningful effect of carrier multiplication in solar cells, impact ionization rate should be maximized. In nanocrystals such as quantum dots, in which the momentum conservation is not required, a very efficient carrier multiplication effect has been reported [24]. Ultimate challenges for the realization of the solar cells that are based on carrier multiplication are finding out materials and structures that have efficient impact ionization and the collection of photo-generated carriers from quantum dot to the external circuit.

1.4.3 Hot carrier solar cells

The physical concept of hot carrier solar cells is based on extracting the carriers from the absorbing medium before they relax to the band edge via phonon

emission (the carriers are still 'hot'). The extraction of the hot carriers depends mainly on two factors: (i) the carriers have to traverse the cell quickly and (ii) the cooling rates of the carriers have to be slow. The hot carriers should be collected from the absorbing medium with selective energy contacts [25]. Quantum dot nanostructures can be implemented in hot carrier solar cells both as absorber and as the energy selective contacts. The discrete density of states in these structures suppresses the carrier cooling in comparison to that of bulk materials [26]. Also, the confined energy states in nanostructures such as quantum wells, wires and dots can be used as energy selective resonant levels of very small width which transmits a very small energy window of hot carriers reflecting the rest of the carriers back to absorber[27]. The extraction of 'hot' carriers enhances the open circuit voltage and hence the efficiency. The limiting efficiency of hot carrier solar cells is predicted to be 85% [7] which is very close to 86.8%, the efficiency of quantum converters optimally matched to the narrow portion of solar radiation.

1.4.4 Multiple transition solar cells

Multiple transition solar cells require the existence of intermediate states (bands) in the previously forbidden energy gap of a conventional semiconductor material. This intermediate band (IB) facilitates the absorption of low energy photons while maintaining the high open circuit voltage that is determined by the quasi Fermi level separation corresponding to the conduction and valence band of the high band gap material. For this to happen, the quasi Fermi levels corresponding to intermediate bands (E_{FI}) should be optically coupled but

electrically isolated from the quasi Fermi level of valence (E_{FV}) and conduction (E_{FC}) bands [3]. Wolf [28] first pointed out the idea of using the energy states in the band gap to absorb sub-band gap photons and calculated the efficiencies using empirical methods. Luque and Marti [5] calculated the detailed balance efficiency limit for intermediate band solar cell (using black body radiation and assuming a zero width intermediate band) to be 63% at the optimum band gaps at E_G=1.95eV, E_{IC}=0.71eV and E_{IV}=1.24eV, as shown in the Fig.1.4.

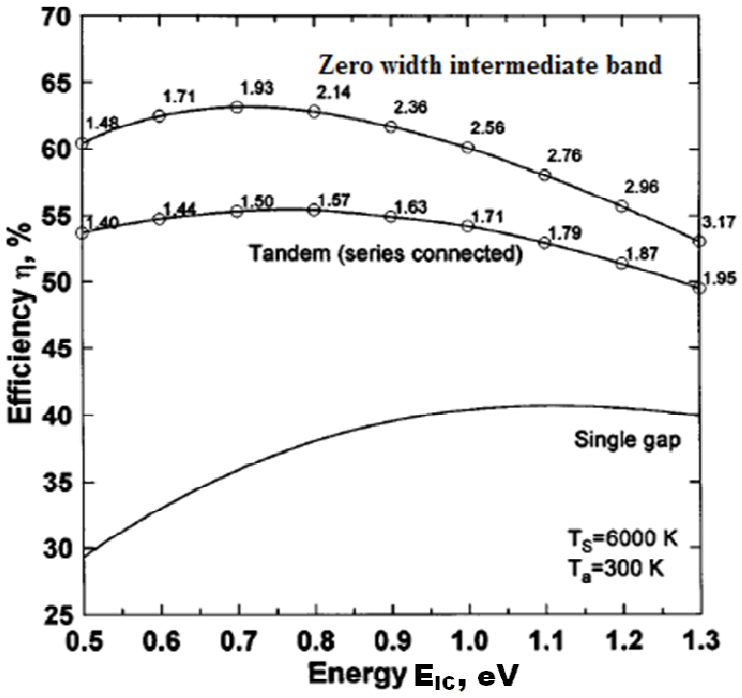

Fig. 1.4 Efficiency limit of an intermediate band solar cell, two terminal tandem solar cell (for the tandem the x-axis values are for the bottom cell, E_{g1}) and a cell with a single band gap (taken from [5]).

In intermediate band solar cells (IBSCs), a material with an IB is situated in the intrinsic region in between the p-type and n-type conventional

semiconductors as shown in Fig.1.5. The IB material should consist of at least one band inside the band gap of conduction band (CB) and valence band (VB).

Researchers around the world are actively looking for and researching on some of the bulk [29,30,31] and molecular materials [32], which have the potential of having an appropriate IB for IBSCs. Until now, to the knowledge of this author, none of these materials have been used as effective IB materials in an intermediate band solar cell.

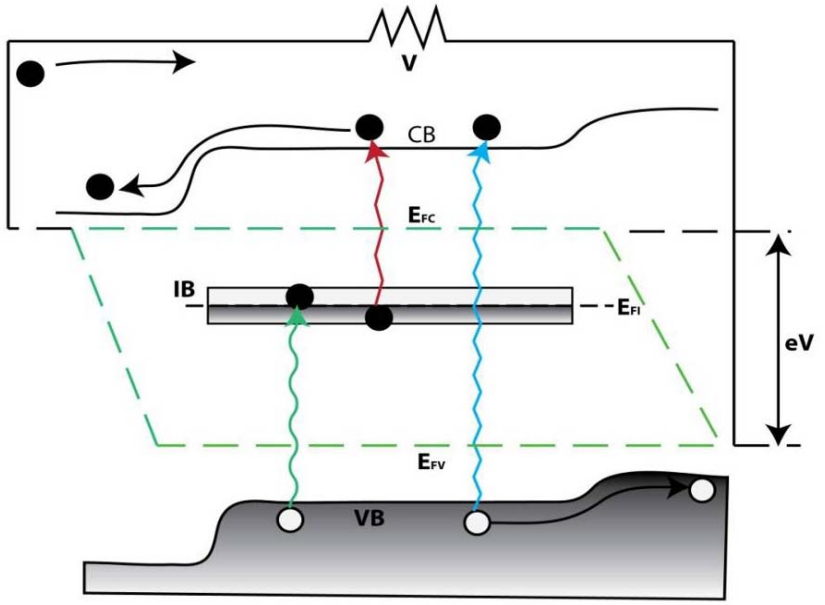

Fig. 1.5 Schematic of the photon absorption process and quasi-Fermi level split in an IB solar cell.

Nanostructures such as quantum well, wires and dots have been proposed as candidate materials for IBSC [33]. In these structures, a nanocrystal of a low band gap material is surrounded by a high band gap material in 1, 2 and 3

dimensions yielding a quantum well, wire and a dot respectively. The confined states in the conduction (Valence) band of a quantum well, wire or dot materials act as an intermediate state that can facilitate the absorption of sub band gap photons. But due to the continuum of k vectors of carriers in a non-confined direction, the quantum well and wires do not have the density of states suitable for maintaining the quasi-Fermi level, as shown in Fig.1.6. The nanocrystal quantum dots, due to their delta function like density of states, can be the suitable candidate materials for maintaining the quasi Fermi level of an intermediate band made by those confined states[34].

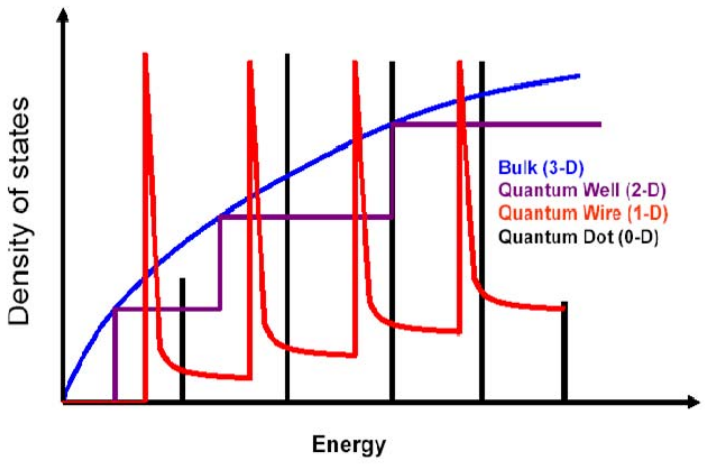

Fig. 1.6 Schematic of density of states of different confinement compared with that of bulk semiconductor.

In quantum dots, the confined states in the conduction or valence band can act as intermediate states, and if the separation between the quantum dot nanocrystals is small enough such that there is significant overlapping of the wave functions among neighboring dots they form a band which can act as an

intermediate band as shown in Fig.1.7. For the application of quantum dots in IBSCs, the well developed Stranski-Krastanov (SK) growth can be used to fabricate the QDs through precisely controlled epitaxial methods using molecular beam epitaxy (MBE) or metalorganic chemical vapor deposition (MOCVD).

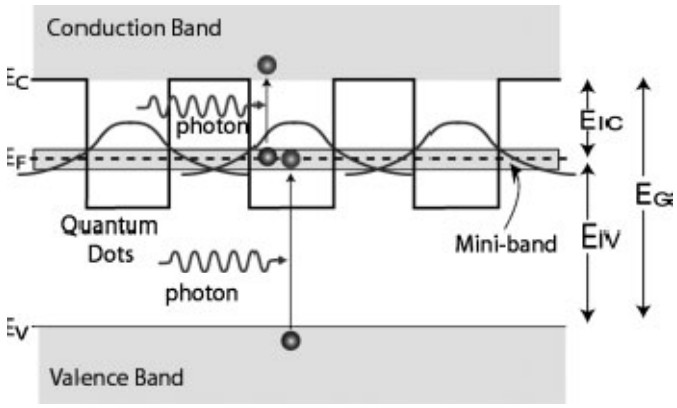

Fig. 1.7 Schematic diagram of intermediate band material with the intermediate band formed by the overlap of quantum dot wave functions.

In the SK growth mechanism, the lattice mismatch between the heterostructure materials plays a significant role to control the shape, size and the uniformity of the quantum dots, together with the growth conditions such as the flux ratio and temperature of the substrate. The dots can be well aligned along the vertical direction and the thickness of the barrier layers can be well controlled in these growth schemes. Thus, by controlling the thickness of the barrier layer in the vertical direction, the formation of intermediate band can be achieved [35].

Among the different issues and challenges in the multiple transition solar cells with QDs as intermediate band material, one of them is to develop a proper material model considering the realistic effects associated with the growth conditions. One of the realistic effects is to include the effect of elastic strain to

determine the energy band parameters of the QDs and the barrier materials. Previous research (theoretical and experimental) in quantum dot solar cells or quantum dot intermediate solar cells revolves around InAs/GaAs and InGaAs/GaAs [36,37,38,39,40] which are not the optimum material combinations for quantum dot intermediate band solar cells QDIBSCs. The essence of the work presented in this dissertation is to find out the optimum nanostructured material combinations for multiple transitions solar cells that have the potential of having photovoltaic conversion efficiency higher than 50%. The material search performed in this work includes some realistic effects such as strain associated with the epitaxial growth of these structures.

1.5 Dissertation Outline

The discussion above highlights the necessity of nanostructured materials in the realization of ultra-high efficiency solar cells. This dissertation addresses a fundamental need in the development of such nanostructured materials, namely the ability to design and predict an optimum nanostructure material and configuration which can be implemented. Such a design process involves the calculation of the band parameters taking the realistic effects such as strain into account, the insertion of these band parameters into detailed balance models, and the search among existing material space for optimum material configurations and different nanostructure shape and sizes

In this dissertation, to investigate the advanced nanostructured concepts for ultra-high efficiency with the existing materials such as III-V and their alloys

together with silicon germanium nanostructures, some of the realistic effects associated with the growth of these materials (particularly, self-assembled quantum dots) are assessed. In chapter 2 of this dissertation, the author formulates the methodology to calculate the strain distribution in and around a single and vertically aligned quantum dots. Using this formulation, different strain components due to single and coupled quantum dots (QDs) are calculated and presented for a few material systems based on III-V heterostructures. Finally, the chapter concludes discussing the significance of strain calculations for the investigation of nanostructured concepts for advanced solar cells.

In chapter 3, the author revisits the empirical methods for band structure calculation. A thorough revision of the k•p method is presented together with its formulation to account the effect of strain in the band structure. The k•p method is used to calculate the band edge alignment of quantum dot heterostructures. The effect of strain on band structure in and around a single and vertically aligned array of QDs is calculated for a few III-V heterostructrues and Ge/Si QD/barrier materials. In addition, this chapter reviews the formulation of effective mass method and its use to calculate the confined electronic states of quantum dots. The results on band structure are presented and discussed for InAs QDs grown on GaAs [001] substrate with GaAs and GaAsSb matrices. The chapter concludes with the analysis of the results and their significance in developing a material model for advanced concept solar cells from the existing material systems.

Chapter 4 is devoted to identify optimum materials by screening material combinations among III-V QD/barrier materials that have optimum band gaps for detailed balance efficiency higher than 40%. Using the effect of strain on band structure, a search for material combinations is performed among III-V material systems given design constraints such as typically achieved QD shape and size, minimum and maximum strain to achieve Stranski-Krastanov growth, and a negligible valence band offset (VBO).

Chapter 5 is concludes the work presented in this dissertation discussing the significance and implementation of this work to different advanced concept solar cell technologies.

Chapter 2

ELASTIC STRAIN DUE TO LATTICE MISMATCH

2.1 Introduction

Ultra-high efficiency advanced concept solar cells require new materials with appropriate band gaps. For example, the efficiency of multijunction solar cells depends on the materials with band gaps that are close to the optimum values obtained from detailed balance efficiency calculations. As shown in Fig.2.1, the limitations on materials that are lattice matched to commonly used substrates such as germanium (Ge) and gallium arsenide (GaAs) impose limitations on the viable options for optimum band gap materials. Thus, for high efficiency multijunction devices with the materials of optimum band gaps, the management of lattice mismatch becomes critical issue. In addition to this, the strain due to lattice mismatch causes change in the band structure of materials and in their optoelectronic properties.

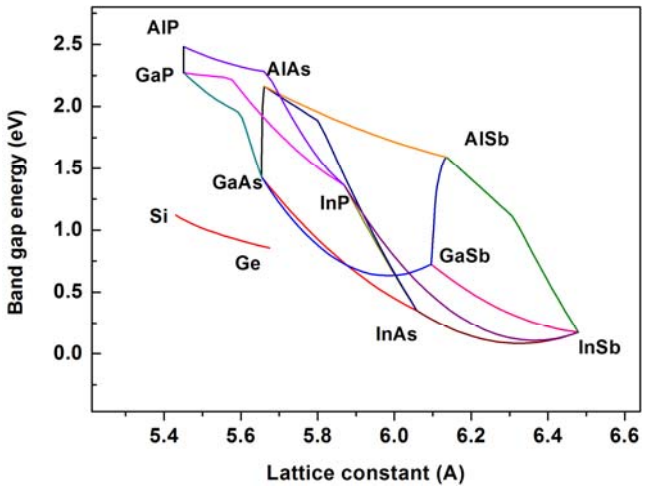

Fig.2.1 Band gap vs lattice constant of III-V and Si,Ge and their alloys.

On the other hand, for ultrahigh efficiency concepts such as multiple exciton generation, hot carrier and multiple transitions solar cells, nanostructures are essential. The nanostructures grown by epitaxial methods have significant strain incorporated in the material, which causes a change in band structure. This band structure modification, in turn, strongly affects the performance of optoelectronic devices based on these QD heterostructures as active layers in the device. Thus, knowledge of the strain distribution due to lattice mismatch is essential for the further modeling of the device containing these heterostructures.

Quantum dots (QDs) are proposed as one of the candidates as an intermediate band material for intermediate band solar cells [41]. One of the ways that is commonly used for the fabrication of quantum dots is through the epitaxial growth of semiconductor materials that have higher lattice constant than that of the materials used as substrate/buffer. When a material with a higher lattice constant than that of the substrate is epitaxially grown on the substrate, the deposited material copies the crystal structure and acquires the lattice constant of the substrate for the first few monolayers. For example when InAs, which has a higher lattice constant (0.6058 nm) than GaAs (0.5653 nm), is deposited on a GaAs substrate, it acquires the lattice constant of GaAs for few monolayers. The InAs material, in this case, is compressively strained (i.e. the lattice of InAs is compressed to accommodate itself to the smaller GaAs lattice constant). The epitaxial layer accumulates strain with its thickness. When its thickness increases the strain energy is released by formation of defects and dislocations or by the formation of quantum dots free of dislocations. In the mechanism of strain release

without defect formation, part of the accumulated strain energy is released by the reorganization of surface materials in which the grown material starts to accumulate at specific spots on the surface starting a three dimensional growth that starts the formation of quantum dots. The thickness at which the 2D growth is unstable either leading defects or QD formation, is called critical thickness, t_c. This growth mode in which the 3D growth occurs at the top of the wetting layer is called Stranski-Krastanov growth. This mechanism of formation of 3D islands causes the lattice distortion in and around the QDs. The strain distribution caused by lattice distortion in the system substantially changes the electronic band structure and hence the optoelectronic properties of the devices made of the QD heterostructures as active layer. Thus, knowledge of strain distribution is essential for the further modeling of the device containing these heterostructures.

Particularly, epitaxially grown self-assembled QDs are probable candidate materials for intermediate band solar cells (IBSCs) [33]. To investigate the feasibility of these nanostructures for IBSCs, the strain distribution due to lattice mismatch is investigated. The results of strain distribution are used to calculate the band structure and ultimately to develop a material model for QD IBSCs in subsequent chapters of this dissertation. As these nanostructures have small absorption cross section [42], a stack arrays of QDs is essential to get significant absorption of solar radiation. Due to this, and also due to the fact that the intermediate band can be formed due to the overlapping of the wave functions of closely spaced QDs, a vertical array of QDs is also considered here for the study of strain distribution.

This chapter starts with the review of the methods used for the calculation of the strain distribution in and around a single quantum dot as well as vertical array of quantum dots and then presents the strain distribution calculated by using an analytical method based on continuum theory of elasticity. Specifically, section 2.1 reviews different methods used to calculate elastic strain due to the lattice mismatch between the QD and the matrix materials. Section 2.2 presents the results of the elastic strain distribution in and around a single quantum dot. Section 2.3 determines the strain distribution of a vertical QD array. This section starts with the explanation of the methodology that is used here to calculate the strain distribution in a vertical QD array. Together with the methodology, the results of strain distribution of vertical QD array with different barrier layer thickness are calculated and compared to that of single quantum dot. Section 2.4 concludes the chapter with a discussion of the impact of the results on specific materials and device structures focusing on InAs/GaAs system because of their relevance to advanced concept approaches. However, the methods and approaches are applicable to a wide range of nanostructured materials and concepts and can be applied to any quantum dot/substrate (matrix) material systems.

2.2 Calculation of strain distribution

The methods of calculation of strain in and around self-assembled quantum dots can be categorized, mainly, in two groups namely, continuum elasticity model and atomistic models. The continuum elasticity model assumes the validity of Hooke's law of linear elasticity. It can be applied for both isotropic and anisotropic materials. In the continuum elasticity model, the strain

distribution due to lattice mismatch in and around the quantum dot can be solved analytically [43,44,45,46,47] by a Green's function method or numerically using finite difference [48] or finite element [49,50] methods. In atomistic models the elastic energy of the strained system is expressed in terms of bond bending and stretching and the total elastic energy is minimized to obtain the relative positions of the lattice sites[51,52,53].

Each model has its advantages and disadvantages. For example, in continuum elasticity models the stress and strain field can be obtained in analytical form, which can provide insight on the strain distribution in and around the quantum dots. On the other hand, some of the assumptions such as isotropy in elastic constants, imposed on the continuum model lead to the loss of details of the calculations in atomic scale. For example, for very thin films (about 2 monolayers (ML)) the continuum elasticity model is less accurate and at the dot barrier interfaces the strain expressions tend to diverge. On the other hand, the atomistic models deal with the displacement of each atom in the calculation domain. Thus, even applying symmetry in the calculations, the problem becomes computationally expensive but the results are more accurate especially at the dot/matrix interface for very thin layer. In Continuum methods, the calculations are computationally less intense. The calculations can be performed and the results can be expressed in any coordinate system depending on the symmetry of QD shape and most importantly, it can be applied to determine the strain distribution of large systems such as quantum dot array. Since photovoltaics requires the use of larger nanostructured systems to achieve substantial

absorption, the merits of continuum theory outweigh its shortcomings and the results are almost same as the one obtained from atomistic theory. Consequently, for this work, continuum theory of elasticity is used to calculate the strain distribution due to lattice mismatch between the dot and substrate/barrier material. The following sections describe each of these approaches in more detail, focusing more heavily on continuum theory of elasticity.

2.2.1 Valence force field method

Despite the computational complexity, due to the accuracy on the results of strain distribution, particularly at matrix/QD interfaces, the valence force field (VFF) method is extensively used to calculate the elastic strain distribution in and around self-assembled quantum dots. In this method, the elastic energy of the material is expressed in terms of few body potentials between the atoms in the crystal. Considering the interaction only up to nearest neighbors, the atomistic valence force field (VFF) method of Keating [54] and Martin [55] can be used to express the elastic energy of the system in terms of bond stretching and bending. The strain energy, in this approach, is written as [56],

$$U_{st} = \sum_{ij} U_2(r_i - r_j) + \sum_{ijk} U_3\left(\theta_{ijk}\right) \tag{2.1}$$

$$\begin{aligned} U_{st} = {} & \frac{1}{4}\sum_{ij} \frac{3\alpha_{ij}}{4\left(d_{ij}^0\right)^2}\left[\left(R_i - R_j\right)^2 - (d_{ij}^0)^2\right]^2 \\ & + \frac{1}{4}\sum_{i}\sum_{j,k>i} \frac{3\beta_{i,jk}}{4d_{ij}^0 d_{ij}^0}\left[\left(R_j - R_i\right).\left(R_k - R_i\right) - \cos(\theta_0) d_{ij}^0 d_{ij}^0\right]^2 \end{aligned} \tag{2.2}$$

In equation (2.2), d_{ij}^{0} and θ_0, respectively, are the ideal bond lengths and angle between atoms i and j of binary constituents. R_i, R_j and R_k are the position of the atoms i, j and k respectively. In the summation, i runs over all atomic positions of the calculation domain and j and k run over only the nearest neighbor sites of ith atom. In this equation, α and β are the bond stretching and bending constants for given materials. For zincblende crystals, $\cos(\theta_0)$ =-1/3. The strain tensor is obtained by minimizing the potential defined in equation (2.2). While this is a computationally demanding method for quantum dot heterostructures, because the displacement of each atom due to lattice mismatch has to be taken into account, it is nevertheless extensively applied [51,56,57,58] to calculate the strain. However, for a system containing a vertical array of more than two quantum dot layers, the computational complexity of this method causes it to be discarded. For the calculation of the strain field due to an array of quantum dots and their effect on band structure a comparatively simplistic method based on continuum theory of elasticity is used.

2.2.2 Green's function method based on continuum theory of elasticity

The key advantage of the continuum theory of elasticity is lower computational expense with almost the same accuracy as the VFF method to calculate stress and strain field in and around the QD. In this method, the calculation domain is considered to be an elastic continuum and the strain distribution in and around the QD is obtained by solving the equilibrium equation of elasticity or minimizing the elastic energy of the domain. This method has

some shortcomings such as; the atomistic details are lost and the results are less accurate at very thin layers of atomistic dimensions; and the strain fields at interfaces and vertices of the QD and matrix where the value of particular strain component is changing rapidly, are less accurate. Despite the shortcomings, continuum elasticity models have been experimentally verified to be valid for layers as thin as couple of monolayer [59]. For simple geometries such as spherical, cuboidal [60], and even pyramidal [46], truncated pyramidal [46,47] and conical [61] shaped quantum dots, analytical expressions for strain distribution in real space can be obtained.

The method used in this work to find out the expressions for stress and strain distribution is based on Eshelby's work [62] on the calculation of strain field of an inclusion within an infinite isotropic elastic medium. The analytical expressions presented in this dissertation for the strain distribution for pyramid and truncated pyramid shaped quantum dots provide an insight for the strain field due to point inclusion in an infinite and semi infinite isotropic elastic medium. The stress and strain fields due to a lattice mismatched inclusion in an infinite medium are derived in this sub-section. For the derivation of elastic stress and strain in and around a quantum dot, this work follows the approaches of references [47] and [63].

In the analytical method, the equilibrium expression

$$\frac{\partial \sigma_{ij}}{\partial r_j} + F_j = 0, \qquad r = (x, y, z) \;\; i, j = x, y, z \tag{2.3}$$

is solved for the specific shape of quantum dot with proper boundary conditions. In equation (2.3), $\sigma_{ij}(r)$ are the stress tensors and $F_j(r)$ is the force per unit volume at point r in the calculation domain. To be more explicit, the $\sigma_{ij}(r)$ component of the stress is the force along the direction j and perpendicular to the surface with i axis at point r. In Cartesian coordinates, $\sigma_{12}(r)$ ($\sigma_{xy}(r)$) is the force along OY direction in the plane OX=a (for cubic crystal). This specific stress causes a shear strain. $F_j(r)$ is the force along jth direction at a point r. The stress tensor is related to the strain tensor, ε, by Hooke's law of linear elasticity as,

$$\sigma_{ij} = \sum_{k=1}^{3}\sum_{l=1}^{3} C_{ijkl}\varepsilon_{kl} \tag{2.4}$$

In equation (2.4), C_{ijkl} ($i,j,k,l = x,y,z$) are the elastic constants which are also called 'stiffness constants'. These constants characterize the elastic properties of the materials. These four index elastic constants, C_{ijkl}, can be written in more concise two index form, C_{jk}, (j,k =1,2,…,6), which connects the stress and strains with 6x6 matrix as,

$$\begin{bmatrix}\sigma_1\\ \sigma_2\\ \sigma_3\\ \sigma_4\\ \sigma_5\\ \sigma_6\end{bmatrix} = \begin{bmatrix} C_{11} & C_{12} & C_{13} & C_{14} & C_{15} & C_{16}\\ C_{21} & C_{22} & C_{23} & C_{24} & C_{25} & C_{26}\\ C_{31} & C_{32} & C_{33} & C_{34} & C_{35} & C_{36}\\ C_{41} & C_{42} & C_{43} & C_{44} & C_{45} & C_{46}\\ C_{51} & C_{52} & C_{53} & C_{54} & C_{55} & C_{56}\\ C_{61} & C_{62} & C_{63} & C_{64} & C_{65} & C_{66}\end{bmatrix}\begin{bmatrix}\varepsilon_1\\ \varepsilon_2\\ \varepsilon_3\\ \varepsilon_4\\ \varepsilon_5\\ \varepsilon_6\end{bmatrix} \tag{2.5}$$

In this notation (also called Voigt's notation), the stress and strain components in equation (2.4) are expressed as,

$$\begin{pmatrix} \varepsilon_{11} & \varepsilon_{12} & \varepsilon_{13} \\ \varepsilon_{21} & \varepsilon_{22} & \varepsilon_{23} \\ \varepsilon_{31} & \varepsilon_{32} & \varepsilon_{33} \end{pmatrix} \Leftrightarrow \begin{pmatrix} \varepsilon_1 & \frac{1}{2}\varepsilon_6 & \frac{1}{2}\varepsilon_5 \\ \frac{1}{2}\varepsilon_6 & \varepsilon_2 & \frac{1}{2}\varepsilon_4 \\ \frac{1}{2}\varepsilon_5 & \frac{1}{2}\varepsilon_4 & \varepsilon_3 \end{pmatrix} \tag{2.6}$$

$$\begin{pmatrix} \sigma_{11} & \sigma_{12} & \sigma_{13} \\ \sigma_{21} & \sigma_{22} & \sigma_{23} \\ \sigma_{31} & \sigma_{32} & \sigma_{33} \end{pmatrix} \Leftrightarrow \begin{pmatrix} \sigma_1 & \sigma_6 & \sigma_5 \\ \sigma_6 & \sigma_2 & \sigma_4 \\ \sigma_5 & \sigma_4 & \sigma_3 \end{pmatrix} \tag{2.7}$$

Out of these 36 components of C_{ij}, in cubic crystals such as GaAs, InAs etc. with the coordinate axes(X,Y,Z) chosen along the edges of the unit cell, only 3 components , C_{11}, C_{12} and C_{44} are non zero [64]. From (2.5),

$C_{1111}=C_{2222}=C_{3333}\equiv C_{11}$,

$C_{1122}=C_{1133}=C_{2233}\equiv C_{12}$ and

$C_{1212}=C_{1313}=C_{2323}\equiv C_{44}$. All other elements are zero. Thus, the matrix of elastic constants in (2.5) reduces to,

$$\begin{bmatrix} C_{11} & C_{12} & C_{12} & 0 & 0 & 0 \\ C_{12} & C_{11} & C_{12} & 0 & 0 & 0 \\ C_{12} & C_{12} & C_{11} & 0 & 0 & 0 \\ 0 & 0 & 0 & C_{44} & 0 & 0 \\ 0 & 0 & 0 & 0 & C_{44} & 0 \\ 0 & 0 & 0 & 0 & 0 & C_{44} \end{bmatrix} \tag{2.8}$$

In this stiffness matrix (2.8), with the definition $C_{12}\equiv\lambda$, $C_{44}\equiv G$ and $C_{11}= \lambda+2G$, the generalized stress strain relation is written as,

$$\sigma_{ij} = 2G\varepsilon_{ij} + \lambda\delta_{ij}\varepsilon_{nn} \tag{2.9}$$

In equation (2.9) λ and G are Lame's constants, and G is also referred as shear modulus. The strain is related to stress as,

$$\varepsilon_{ij} = \sum_{k=1}^{3}\sum_{l=1}^{3} S_{ijkl}\sigma_{kl} \tag{2.10}$$

In this equation the constants S_{ijkl} are called compliance constants and have same symmetry properties as that of C_{ijkl} in equation (2.4). For [001] growth direction, for cubic crystals such as GaAs, InAs etc., the elastic constants; Young's modulus, E, and Poisson ratio, ν, can be obtained from these stiffness and compliance constants as,

$$E = \frac{1}{S_{11}} = \frac{\left(C_{11} - C_{12}\right)\left(C_{11} + C_{12}\right)}{\left(C_{11} + C_{12}\right)} \tag{2.11}$$

$$\upsilon = -ES_{12} = \frac{C_{12}}{\left(C_{11} + C_{12}\right)} \tag{2.12}$$

With the basic definition of stress strain relations and the different elastic constants, the methodology of the calculation of stress distribution due to lattice mismatch of the epitaxially grown material on a substrate/matrix is formulated below.

When force (stress) is applied to a crystal, the lattice points gets displaced from their positions, and if we know the relative displacements of each lattice site, the state of the crystal deformation can be described by the strain components:

$$\varepsilon_{ij} = \frac{1}{2}\left(\frac{\partial u_i}{\partial r_j} + \frac{\partial u_j}{\partial r_i}\right) \tag{2.13}$$

In expression (2.13), u_x, u_y, u_z are the relative displacements of the crystal lattice points along x, y and z-axes respectively. Since, ε_{ij} is a matrix, the diagonal elements represent extension (or contraction) per unit length along x, y and z and

the off-diagonal elements represent rotations (or shear). Substituting equations (2.9) and (2.13) into equation (2.3), we get:

$$G\nabla^2 u_i + (\lambda + G)\frac{\partial \varepsilon_{nn}}{\partial x_i} + F_i = 0 \qquad (2.14)$$

This equation is called Navier's equation of elasticity. With the body forces being zero, equation (2.14) can be written as,

$$G\nabla^2 u_i + (\lambda + G)\frac{\partial \varepsilon_{nn}}{\partial x_i} = 0 \qquad (2.15)$$

Equation (2.15) can be expressed in vector form as,

$$(\lambda + G)\nabla(\nabla \bullet \vec{u}) + G\nabla^2 \vec{u} = 0 \qquad (2.16)$$

In this equation, *u* is the vector field of lattice displacements. This vector field can be written in terms of scalar, Φ, and vector, Ψ, potentials as,

$$\vec{u} = \nabla\Phi + \nabla \times \vec{\Psi} \qquad (2.17)$$

With the substitution of *u* from (2.17) to (2.16) we get,

$$(\lambda + 2G)\nabla(\nabla^2\Phi) + G\nabla \times \nabla^2\vec{\Psi} = 0 \qquad (2.18)$$

Particular solutions of equation (2.18) are the functions that satisfy,

$\nabla^2\Phi = \text{constant}$ and $\nabla^2\vec{\Psi} = \text{constant}.$

A particular solution can be obtained with the choice of $\nabla^2\Phi = \text{constant}$, $\vec{\Psi}$=0, Here, the function Φ is called Lame's potential and can give the strain field. Any harmonic function can be used as Lame's potential that can satisfy Navier's equation and the resulting displacement field can be written as,

$$\vec{u} = \frac{1}{2G}\nabla\Phi \tag{2.19}$$

The Lame's potential for strain relaxation due to an inclusion in an infinite medium, can be written as [65]

$$\nabla^2\Phi(r) = \frac{1+\nu}{1-\nu}2G\varepsilon_0(r) \tag{2.20}$$

In equation (2.20), ν is Poission's ratio and $\varepsilon_0(r)$ is the initial misfit strain between two materials. The misfit strain is defined as, $\varepsilon_0 = \frac{a_{matrix} - a_{incl}}{a_{incl}}$,where a_{matrix} is the lattice constant of matrix material and a_{incl} is the lattice constant of the inclusion (in this case a quantum dot material). The solution of equation (2.20), using the analogy with Poisson's equation in electrostatics is obtained by using Green's function and can be expressed as,

$$\frac{1}{2G}\Phi(r) = -\frac{1+\nu}{1-\nu}\frac{1}{4\pi}\iiint_V g(r,r')\varepsilon_0(r')d^3r' \tag{2.21}$$

with $g(r,r') = \frac{1}{|r-r'|}$, where point *r'* lies inside the volume of the dot. The initial misfit strain ε_0 is assumed to be constant inside the dot volume for the calculations in this work. The Green function *g (r, r')* can be written as,

$$g(r,r') = -\frac{1}{2}\nabla \bullet \frac{r-r'}{|r-r'|} \tag{2.22}$$

Substituting the expression (2.22) of *g(r,r')* in equation (2.21) and using the Gauss' divergence theorem of volume integrals, equation (2.21) can be written in terms of surface integral as,

$$\frac{1}{2G}\Phi(r)=\frac{1+\nu}{1-\nu}\frac{1}{8\pi}\varepsilon_0\iint_S\frac{(r-r')}{|r-r'|}dS(r') \qquad (2.23)$$

The stress components, $\sigma_{ij}(r)$ can be obtained from (2.23) and can be expressed as,

$$\sigma_{ij}(r)=-\frac{\varepsilon_0 E}{8\pi(1-\nu)}\iint_S\frac{(i-i')\hat{i}+(j-j')\hat{j}}{|r-r'|^3}dS(r')+\delta_{ij}\frac{\varepsilon_0 E}{(1-\nu)}\iiint_V\delta(r-r')dV(r') \qquad (2.24)$$

In equation (2.24), i and j are unit vectors in i^{th} and j^{th} directions respectively, δ_{ij} is Kronecker delta function. The second term in equation (2.24) comes from evaluating the surface integral when r approaches the boundary r', the surface of the dot. The expression of stress distribution is obtained by integrating equation (2.24), which depends strongly on the shape of quantum dots. The shape, size, material composition and density of quantum dots are determined by different growth parameters such as lattice mismatch, growth rate, substrate temperature and many more.

The shape, composition and the dimension of these nanostructure materials influence the strain distribution in and around the quantum dot nanostructures and ultimately the optoelectronic properties of the device using these nanostructures as active components. Because the solution of the strain equations requires assumptions about the physical properties of the QD, the following section provides a brief discussion on the dependence of QDs shape size and composition on growth parameter and lattice mismatch.

2.3 Physical parameters of epitaxially grown QDs

In heteroepitaxial growth, the formation of self-assembled quantum dots is driven by the elastic strain due to lattice mismatch. In Stranski-Krastanov growth

mode, the layer by layer growth changes to island formation as schematically shown in Fig.2.2. The islands rest at the top of a 2D film called wetting layer. In the transition of growth mode from 2D to 3D, the strain is relieved by the increased surface energy of the 3D islands without formation of any defects or dislocations.

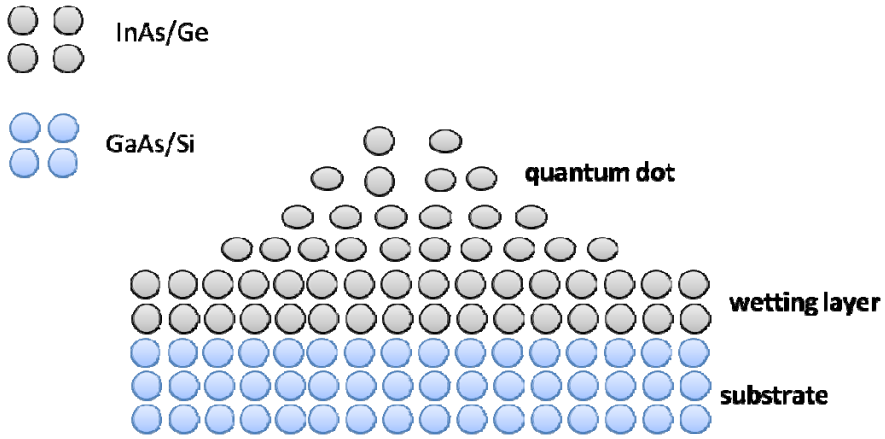

Fig. 2.2 Schematic diagram of the formation of quantum dots by Stranski-Krastanov growth.

In epitaxial growth using Molecular Beam Epitaxial (BME), atoms or clusters of atoms produced by heating up a solid source migrate in an ultra high vacuum (UHV < 10^{-10} torr) environment, and impinge on a hot substrate surface, where they can diffuse and eventually are incorporated into the growing film. In MBE, the molecular beams may be either from thermally evaporated elemental sources or from organic precursors (in gas-source MBE). The material sources have to be extremely pure and the entire process is done in an ultra high vacuum environment. In heteroepitaxial growth such as InAs on GaAs, or germanium on silicon the later (i.e., the substrate) is first heated to an appropriate temperature in an UHV to remove native oxide on the surface. In case of InAs on GaAs, arsenic

has higher vapor pressure (higher volatility than the Ga atoms) that's why there should be a constant supply of arsenic atoms to the surface of heated GaAs while it is being heated to remove oxygen. After the native oxide is removed (confirmed by the RHEED patters, change from hazy to streaky), the indium source is opened for InAs growth. Proper flux of indium (In) and arsenic (As) arriving on the surface of GaAs substrate bond with each other forming InAs. Experimentally, a change in RHEED profile from streaky to spotty is observed as an indication of the change of flat surface to well developed 3D islands. The shape, size, density and composition of the self-assembled quantum dots depend on several factors, which are listed and discussed below.

1. Lattice mismatch

For a given growth temperature, a smaller lattice mismatch between the substrate/buffer and QD material gives a thick wetting layer and smaller size quantum dots. The critical thickness of the QD formation decreases with the increase of lattice mismatch between the substrate/buffer material and the QD material. The ratio of height to lateral dimension of the QDs decrease (shorter QDs for same base width) with the decrease of strain [66]. It is seen, experimentally, that with the decrease of misfit strain between the substrate and QD material, the QD diameter slowly decreases and the height increases [67]. In the vertically stacked multilayer structures a gradual increase in the QD size from layer to layer has been observed due to the reduction in strain caused by the relaxation of strain in underlying layer of QDs[68]. However, this can be

overcome by depositing a lower amount of the dot materials in consecutive layers [69].

2. Growth rate

The growth rate has strong influence on the size and composition of QDs. The temperature and flux rate can be controlled to get the desired density and size of quantum dots up to certain range. It has been experimentally observed that smaller growth rate lead to larger dots with uniform size distribution [70] and reduced number density [71]. In addition to this, the lower growth rate gives QDs with higher In fraction and when the growth rate is increased both In and Ga can be incorporated from the wetting layer into the QD and indium fraction drops.

3. Growth temperature

Dot size increases as the growth temperature increases [72]. The higher the growth temperature, the higher will be the diffusion length of the impinging atoms on the surface. Thus a growth at comparatively higher temperature at given fluxes of In and As results larger quantum dots with better uniformity. This increase in volume of QD material at higher growth temperature is due to the incorporation of material from the wetting layer or by the Ga diffusion from GaAs substrate [73]. The growth temperature has a profound effect on shape and size of SiGe QDs as well. For general growth conditions, SiGe QDs on silicon have a bimodal shape and size distribution, comprising pyramid shaped small dots and multifaceted dome-shaped comparatively larger dots. For example, at a growth temperature of less than 500 ^{o}C, the pyramid shaped QDs are dominant in number

density while the number density of dome-shaped QDs dominates at growth temperature higher than 500^{o}C[74]

4. Coverage

With the increase in thickness of the capping layer, the QDs undergo strong shape and size evolution. Overgrowth transforms the pyramid shaped islands to truncated pyramid shaped [75]. For example, when the islands of SiGe are covered with Si, the SiGe atoms at the apex of pyramid and deposited Si are intermixed to reduce the surface energy to minimize strain [66]. Also, this mechanism dissolves the small islands. The shape and size of the QDs change significantly with the thickness of the coverage layer. As shown in Fig.2.3, the general trend is that the atoms from the QD top surface diffuse to the side of QD resulting in decrease in height and increase in base dimensions [76]. Due to this diffusion, the shape evolves to truncated pyramid, which is confirmed by cross-sectional scanning-tunneling microscopy [77,78].

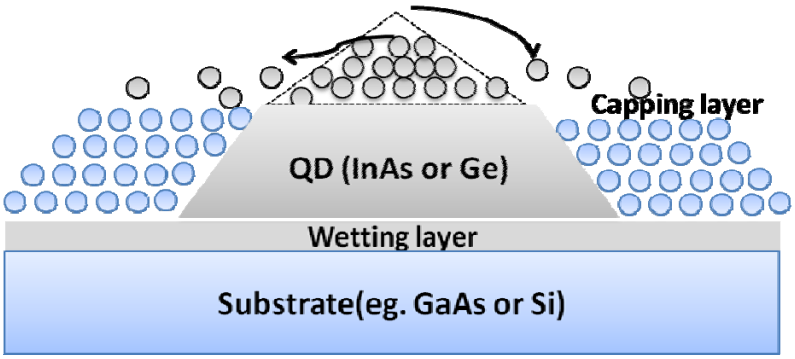

Fig. 2.3 Schematic of the shape evolution of quantum dot while capping.

The size of QD depends on the growth parameters such as substrate temperature, amount of material grown and arsenic flux pressure [79]. The higher substrate temperature causes larger diffusion length of ad-atoms. This, results into larger size of QDs. Thus the shape and size of the quantum dots depend on the material parameters and the growth conditions. The shape of quantum dots is reported to be as that of a lens, multifaceted dome, pyramid and truncated pyramid [47,78,80]. Based on the experimental reports in the literatures, the shape and size of the quantum dots is considered to be as that of a pyramid and truncated pyramid for the strain calculations in the following sections.

2.4 Elastic strain distribution due to a quantum dot in an infinite matrix

Given that the most common shapes of epitaxially grown QDs are pyramidal and truncated pyramidal, here we present the analytical expressions for pyramid and truncated pyramid shaped quantum dots. For a pyramid shaped (or truncated pyramid shaped) quantum dot with height h, truncation factor f ($0 \leq f \leq 1$, $f=1$ corresponds to a full pyramid) and base dimension a and b (rectangular base, for squared base $a=b$) the integration limit for integral (2.24) is:

$$\begin{aligned} -a\left(1-\frac{z}{h}\right) \leq x' \leq a\left(1-\frac{z}{h}\right) \\ -b\left(1-\frac{z}{h}\right) \leq y' \leq b\left(1-\frac{z}{h}\right) \\ 0 \leq z' \leq hf \end{aligned} \qquad (2.25)$$

With the z-axis along [001] crystallographic direction as growth direction and considering the origin of the Cartesian coordinate system at the center of the base of the pyramid, the stress components in (2.24) are obtained in analytical form.

The expressions of the stress components obtained by integrating equation (2.24) with the integration limit expressed in (2.25), are presented in appendix A using the same notation as in reference [46]. For simple geometries such as square based pyramid with aspect ratio 2 (the ratio between the base and the height, $B=2a$ and $h=a$), the expressions as a function of position along z-axis ($x=y=0$) are readily obtained and can be expressed in a comparatively simplistic form as [47],

$$\begin{aligned}\sigma_{xx} = \sigma_{yy} = 2\left[-\tan^{-1}\left(\frac{z-a}{|z-a|}\right)+\tan^{-1}\left(\frac{z}{\sqrt{2a^2+z^2}}\right)\right] \\ +\frac{1}{2}\left[\ln\left|\frac{\sqrt{2a^2+z^2}-a}{\sqrt{2a^2+z^2}-a}\right|-\ln\left|\frac{\sqrt{2a^2+z^2}-a}{\sqrt{2a^2+z^2}-a}\right|\right] \\ \frac{2}{\sqrt{3}}\left[\ln\left(\frac{(z-a)}{\sqrt{3}}+|z-a|\right)-\ln\left(\frac{-2a-z}{\sqrt{3}}+\sqrt{2a^2+z^2}\right)\right]\end{aligned} \tag{2.26}$$

$$\begin{aligned}\sigma_{zz} = 4\pi - 4\left[-\tan^{-1}\left(\frac{z-a}{|z-a|}\right)+\tan^{-1}\left(\frac{z}{\sqrt{2a^2+z^2}}\right)\right] \\ +\left[\ln\left|\frac{\sqrt{2a^2+z^2}-a}{\sqrt{2a^2+z^2}+a}\right|-\ln\left|\frac{\sqrt{2a^2+z^2}+a}{\sqrt{2a^2+z^2}-a}\right|\right] \\ \frac{4}{\sqrt{3}}\left[\ln\left(\frac{(z-a)}{\sqrt{3}}+|z-a|\right)-\ln\left(\frac{-2a-z}{\sqrt{3}}+\sqrt{2a^2+z^2}\right)\right]\end{aligned} \tag{2.27}$$

The strain components for isotropic elastic solid can be obtained from the stress components using Hooke's law as,

$$\varepsilon_{ij} = \frac{1}{E}\left[(1+\nu)\sigma_{ij} - \delta_{ij}\nu\sigma_{nn}\right] \tag{2.28}$$

From the diagonal components of strain tensor (ε_{ij}, $i=j$), the hydrostatic and the biaxial strains are defined as,

$$\varepsilon_h = \varepsilon_{xx} + \varepsilon_{yy} + \varepsilon_{zz} \tag{2.29}$$

$$\varepsilon_b = \varepsilon_{zz} - \frac{1}{2}\left(\varepsilon_{xx} + \varepsilon_{yy}\right) \tag{2.30}$$

These two strain components expressed in equation (2.29) and (2.30) can be coupled to energy band parameters such that the change in band structure due to strain can be calculated. The hydrostatic strain couples with the conduction band via conduction band deformation potential and the biaxial strain couples with valence band via valence band hydrostatic and shear deformation potentials. Detailed discussions of the effect of strain in the band parameters are the main content of chapter 3.

The equations above allow the calculation of strain profile (1D and 3D) for a truncated and full pyramid shaped QDs with parameters given in Fig.2.4. The material parameters used to calculate the strain distribution in and around QD, taken from reference [81], are listed in Table 2.1. The lattice constant and elastic constants of $GaAs_{1-x}Sb_x$ are obtained from linear interpolation of that of GaAs and GaSb.

Strain components (ε_{xx} and ε_{zz}) along a line perpendicular and passing through the center of the base of a pyramid shaped QD are presented in Fig. 2.5. In this figure, the results of strain distribution obtained from the method based on continuum theory of elasticity (this work) are presented together with the results of strain distribution calculated from VFF method [57] and finite difference method [58]. The size of the QD (base length 12 nm and height 6 nm) was taken to be same as the one in references [57] and [58] to compare the different methodologies. Despite the computational simplicity of the method used in this

work, the results are in very good agreement with the results of stain distribution obtained by Crusack et al. [57] using VFF method and Grundmann et al. [58] using finite difference (FD) method. The agreement of the results obtained from the analytical method and those obtained from other computationally expensive methods such as VFF and FD technique shows the validation of the technique used in this work and allows us to use computationally simple method. Computational simplicity is important since the strain calculations are required in the search of the III-V tertiary material space for optimum QD/barrier material combinations for intermediate band solar cells.

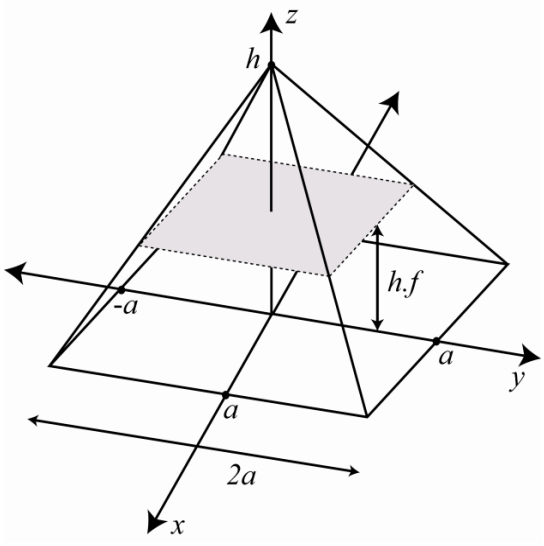

Fig. 2.4 Schematic diagram of the truncated pyramid shaped quantum dot assumed in the calculations.

Table 2.1 Material parameters used in calculation of strain distribution

parameters		InAs	GaAs	GaSb
Lattice Constant	a(^{o}A)	5.660	5.6533	5.6096
Elastic constants	C_{11}(GPa)	832.9	1221.0	884.2
	C_{12}(GPa)	452.6	566.0	402.6
	C_{44}(GPa)	396.0	600.0	432.2

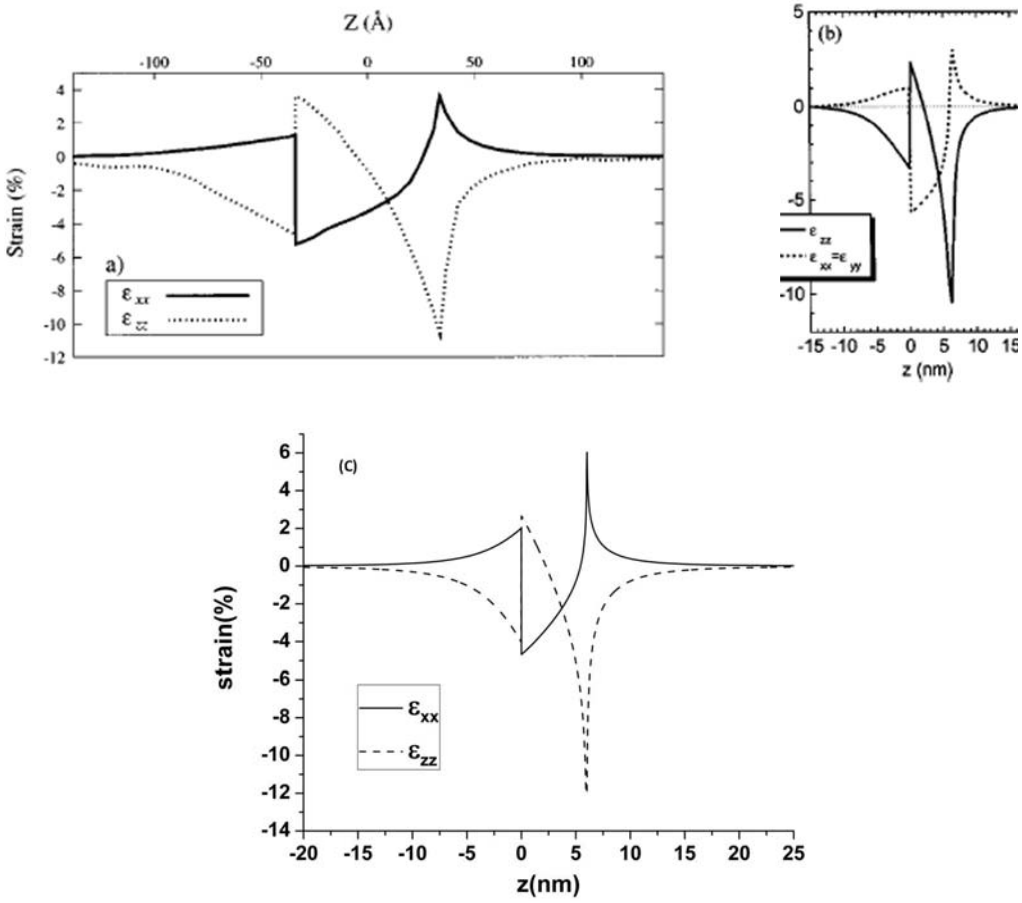

Fig. 2.5 Strain components ε_{xx} and ε_{zz} for a pyramid shaped QD along a line perpendicular and passing through the center of the base of pyramid: (a) obtained by Crusack [57] using VFF method (a) obtained by Grundmann [58] using FD method and (c) calculated by analytical method (this work).

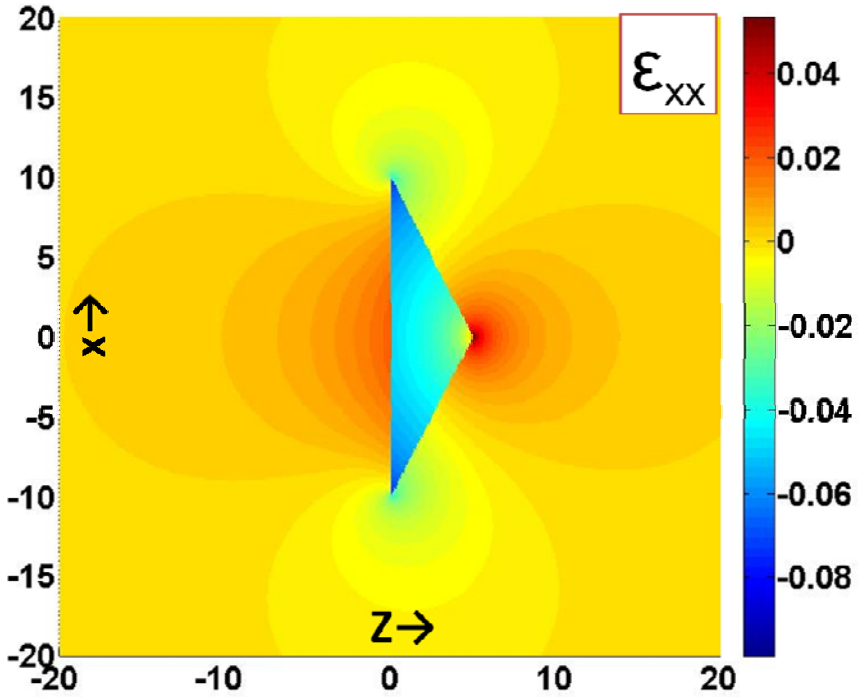

Fig. 2.6 Elastic strain (ε_{xx}) distribution of InAs QD buried in an infinite GaAs matrix (lattice mismatch 6.7%). A square based (a=20nm), 5nm tall full pyramid shaped QD.

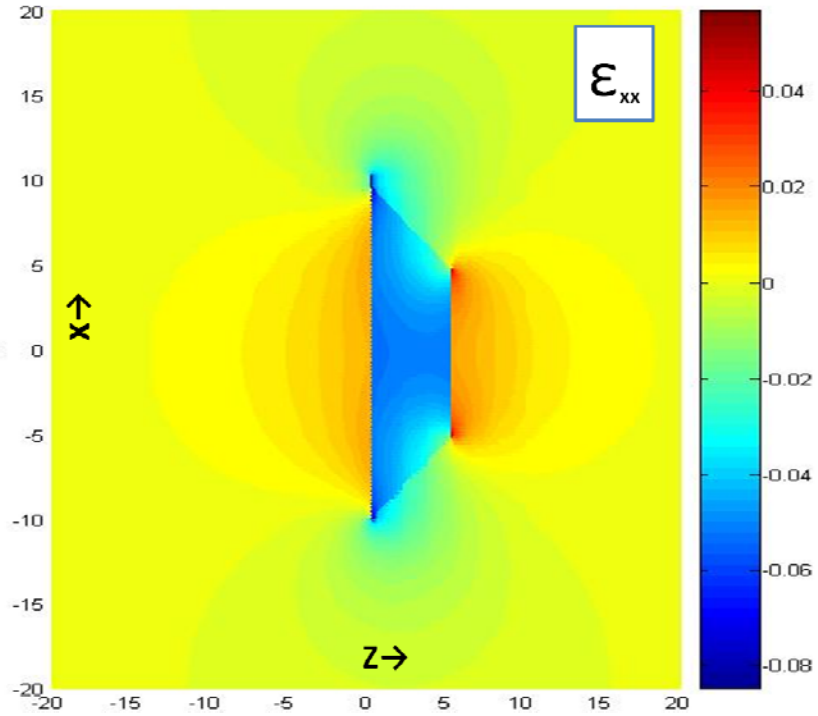

Fig. 2.7 Elastic strain (ε_{xx}) distribution of InAs QD buried in an infinite GaAs matrix (lattice mismatch 6.7%). A square based (a=20 nm), 5 nm tall truncated pyramid shaped QD.

From the Fig 2.6 and 2.7 (the result of ε_{xx}), it can be seen that the planar strain component (ε_{xx}) in case of InAs QDs grown on [001] GaAs substrate has compressive (-ve) value at the base of the dot in both full and truncated pyramid shaped quantum dots. It occurs because when the InAs is epitaxially grown on GaAs, the InAs grows at the lattice sites of the GaAs and have to acquire the lattice constant of the later. On the other hand, to compensate this, the lattice constant in the plane along the growth direction [001] increases causing the QD material to have tensile strain. Conversely, for GaAs material just below the base of QD, in plane lattice constant is increased and the lattice constant along the growth direction [001] is decreased. Except at the base of the QD structure, the

distribution of planar strain is different in these two cases. In case of truncated pyramid shaped QD, the planar strain component is always compressive inside whereas in case of full pyramid shaped QD, at the tip of the quantum dot, the stress force is mainly acting from the sides and is along the z direction. Therefore, at the tip of QD, the planar strain component is tensile.

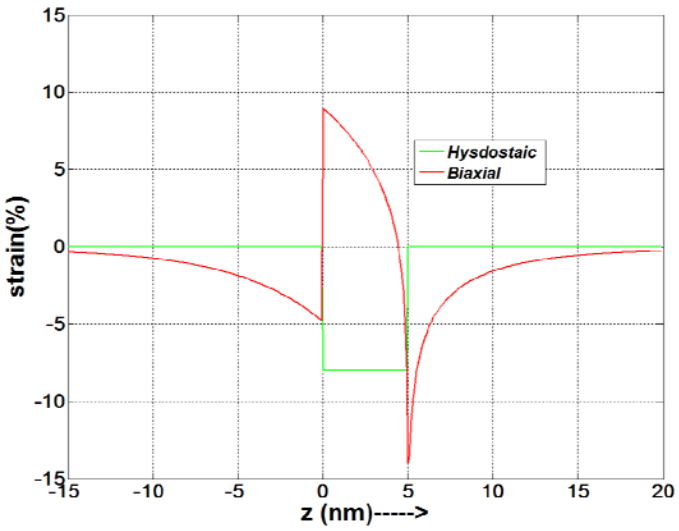

Fig 2.8 Hydrostatic and biaxial strain components of a full pyramid shaped InAs quantum dot grown on GaAs [001] substrate along the z axis (x=y=0) passing through the center of the base of the dot.

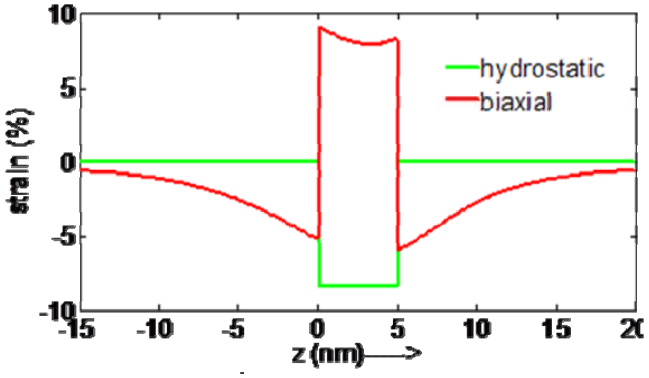

Fig.2.9 Hydrostatic and biaxial strain components of a truncated pyramid shaped InAs quantum dot grown on GaAs [001] substrate along the z axis (x=y=0) passing through the center of the base of the dot.

The hydrostatic and biaxial strains for full pyramid and truncated pyramid shaped quantum dots of base length 20 nm and height 5 nm (full height in case of full pyramid and truncated height in case of truncated pyramid shaped QDs) are presented in Fig.2.8 and 2.9 respectively. From these figures it is clear that the hydrostatic strain is constant inside the dot and biaxial strain has strong spatial variation in and outside the dot. The biaxial strain is positive everywhere inside the dot in truncated pyramid shaped case but changes to negative at the tip with very strong spatial variation in the case of pyramid shaped QD. This strain distribution at the tip of pyramid shaped QD explains the shape evolution of QD to truncated pyramid when a barrier material is deposited for QD coverage.

2.4.1 Summary for single QD strain calculations

Overall, the strain distribution of truncated and full pyramid shaped quantum dots was calculated and presented in this section. The strain distributions presented here are in a very good agreement with the results obtained from

sophisticated atomistic calculations [48, 51]. The hydrostatic and biaxial strains distributions presented here are implemented in chapter three to calculate the band structure of quantum dots with the effect of strain. Importantly, this computationally simple method allows the calculation of the strain distribution of vertical array of QDs which otherwise would be very difficult if not impossible with atomistic approaches.

2. 5 Elastic strain distribution of vertical array of quantum dots

It is well known that the quantum dots have relatively small absorption cross section [42,82] for both inter band and intra-band transitions. Therefore, particularly, in quantum dot infrared photo detector (QDIP) and quantum dot solar cells (QDSCs), multiple layers of quantum dots have to be stacked to get significant contribution of QDs in device performance. The optoelectronic properties of vertically stacked arrays of quantum dots must be calculated for their application as absorbing medium in QDSCs. The starting point for this is the analysis of the elastic strain distribution and its effect on the band structure of quantum dot super lattice. In this section, we investigate the strain distribution due to vertically stacked arrays of self-assembled quantum dots.

The distribution of elastic strain field due to coherently strained islands extends to the surrounding matrix. Thus, there is a strain field modulation at the surface of the material that is grown as covering layer at the top of the QDs. The strain field strongly affects the growth of QD material at the subsequent layer. The covering layer (let's say GaAs) directly above the QD (let's say InAs) has comparatively larger lattice constant (tensile strain) than the layer which doesn't

have QD below it. This variation in lattice constant of the surface of covering layer drives the vertical stacking of the quantum dots. Thus the InAs deposited on the GaAs coverage layer has preferential nucleation sites directly above the quantum dot in lower layer. In this section, we calculate the strain distribution due to vertical array of InAs quantum dots grown on [001] GaAs substrate with varying thickness of barrier layer in order to analyze the effect of vertical spacing on strain distribution. The strain profile of a single QD is also presented for comparison.

Previous works on calculation of strain distribution due self-assembled QD are focused for single QD [47,48]. Experimental studies on vertical array of SK QDs show the indication of electronic coupling when the vertical spacing between the dots is less than 10 nm [83,84,85] but for the strain coupling the separation between the dots can be as large as 20 nm [86,87].

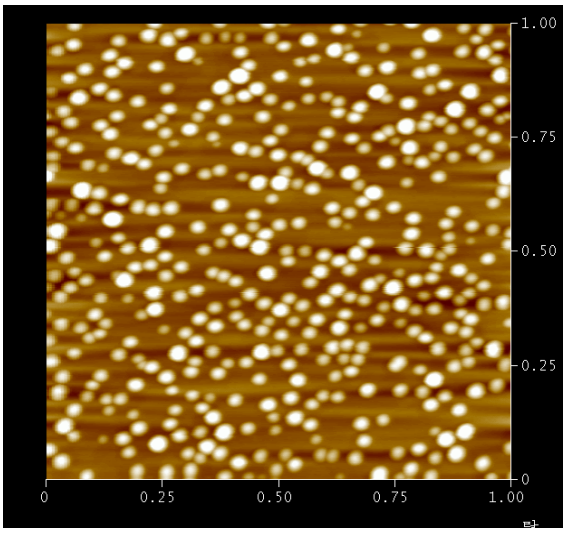

Fig.2.10 AFM image showing planar spacing, and size of InAs QDs grown on GaAsSb(Courtesy: K.Y Ban, Solar Power Lab, ASU).

For the calculation of strain distribution due to a vertically aligned array of quantum dots, the stress distribution due to each quantum dot is calculated from the analytical method based on continuum theory of elasticity as outlined in previous section 2.3. Since the elastic problem is linear, the stress field at each point in and around the QDs in the QD array is obtained by superposition of stress field due to each individual quantum dots in the structure. Then the corresponding strain components are obtained from the stress strain relations in equation (2.28). A five layered structure with different vertical spacing, *Hz*, (i.e., the spacing between the top of QD to the bottom of QD in two consecutive layers) as shown in Fig.2.11 is considered. Since the planar spacing between the QDs (*Lx*, in Fig.2.11) for normal growth conditions are reported to be about 50 nm and this is relatively large [88,89] for strain and electronic coupling among the QDs in a plane (see Fig. 2.10), here the calculations are focused only on the vertical spacing of the QD layers. The strain distributions ε_{xx}, ε_{zz} and the hydrostatic and the biaxial strains are calculated for different vertical spacing (*Hz*), keeping the shape and size of QDs to be same in all cases. For our calculations, as mentioned in previous section, we consider the both the pyramid and truncated pyramid shaped quantum dots with base length a= 20 nm and height h =5 nm (hf =5 nm, for truncated pyramid) respectively. The strain calculations are performed for spacer layer thickness between the dots (*Hz*) 3 nm, 5 nm, 7 nm and 10 nm. The minimum (3 nm) and maximum (10 nm) values of spacer layer thickness for this work are chosen on the basis of experimental results which show that (i) at thickness greater than 10 nm there is no guarantee of vertical ordering [87] and

(ii) for the spacer layer thickness less than 3 nm, the dots are so defective [86] that they have deleterious effect on device. With the above mentioned spacing layer thicknesses and the base dimensions, the strain distributions of both the truncated and full pyramid shaped quantum dots is calculated and analyzed. The results of the strain distribution (hydrostatic and biaxial strains) obtained in this section are used as input parameters to calculate the band edge alignment and hence the electronic structure of QD array in chapter 3.

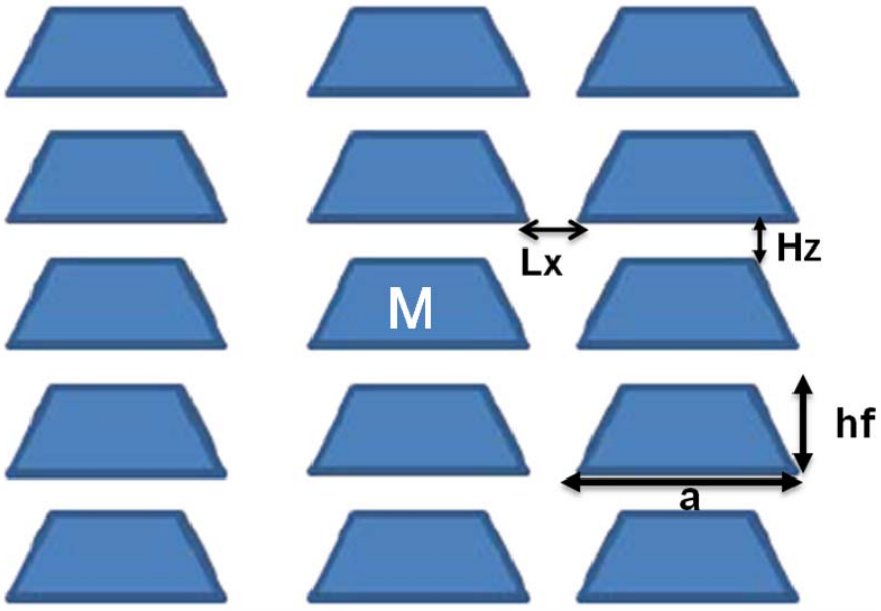

Fig. 2.11 schematic of QD array with truncated pyramid shaped QDs considered in calculation.

2.5.1 Results and discussions

Calculated according the calculation method outlined above, different strain component of pyramid and truncated pyramid shaped quantum dots are presented in this section. Fig.2.12 shows the strain components ε_{xx} of an array of 5 layers of QDs (each QD square based pyramid shaped with base length 20 nm

and height 5 nm) with spacer layer thickness of 5nm. For comparison, the strain profile of a single QD buried in an infinite medium (legend "infinite) is also presented.

The strain properties of a vertically stacked array of QDs can be expected to be as in the mid-QD layer, labeled as "M" in Fig.2.11, in the array of 5 QD layers. Therefore, further discussion of the strain profile of a QD array is focused on properties of this QD layer. From Fig.2.12 it is clearly seen that qualitatively,

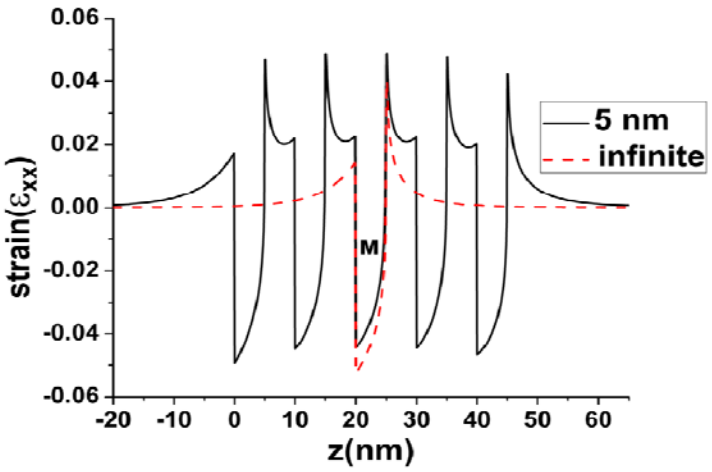

Fig. 2.12 Strain component ε_{xx} of QD array of pyramid shaped five QD layers with 5 nm spacer layer thickness along a line perpendicular and passing through the center of the base.

the strain component ε_{xx} inside the QD of a QD array is same as that of single QD buried in an infinite medium. Quantitatively, the planar strain is reduced significantly in the array in comparison to single QD. In the QD array, the strain component, ε_{xx}, is relaxed in comparison to isolated QD due to the interaction of the strain fields from the neighboring dots. On the other hand, in the barrier

material the strain profile of the QD array is significantly changed both qualitatively and quantitatively in comparison to a single QD. In the array, outside the QDs, the tensile strain from the consecutive layers superimpose causing the barrier material to be more dilative. A closer view of the variation of strain profile of the array with different spacer layer thickness is presented in Fig.2.13, where the strain profile of the mid layer are presented for different spacer layer thickness, namely 3 nm, 5 nm, 7 nm and 10 nm. For comparison the strain profile of single QD buried in an infinite medium (legend "infinite" in Fig.2.13) is also presented. A careful look in Fig.2.13 shows that the strain profile in the spacer layer changes significantly for spacer layer thickness of 3 nm in comparison to other values. Due to the superposition of the strain field from neighboring layers, the barrier is highly tensile both above and below the QD layers in the 3 nm spacing case. This theoretical observation is consistent with experimental observations of strong strain driven intermixing of indium and gallium between the dot and the barrier layer when the spacer layer thickness is less than 4 nm [90,91].

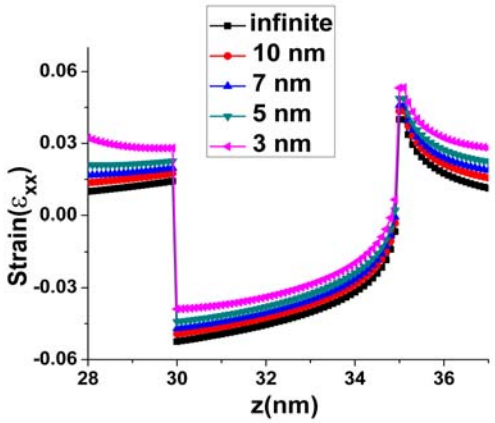

Fig. 2.13 Strain component ε_{xx} along a line perpendicular and passing through the center of the base of square based (20 nm) full pyramid shaped QD array for different spacer layer thickness.

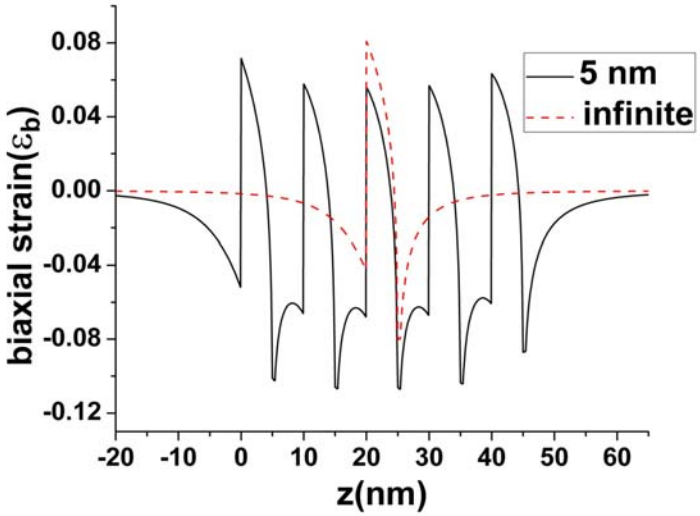

Fig. 2.14 Biaxial strain, ε_b of QD array of pyramid shaped five QD layers with 5 nm spacer layer thickness along a line perpendicular and passing through the center of the base.

In Fig.2.14, the biaxial strain components ε_b of an array of 5 layers of QDs (each QD square based pyramid shaped with base length 20 nm and height 5nm) with spacer layer thickness of 5nm are presented. For comparison, the strain

profile of a single QD buried in an infinite medium (legend “infinite) is also presented. As in the case of single QD, qualitatively, the biaxial strain component ε_b inside the QD of a QD array is same as that of single QD buried in an infinite medium. Quantitatively, the strain ε_b is reduced significantly in the array in comparison to single QD.

A closer view of the variation of strain profile ε_{zz} of the vertical QD array with different spacer layer thickness is presented in Fig.2.15, where the strain profile of the mid layer are presented for different spacer layer thickness namely 3 nm, 5 nm, 7 nm and 10 nm. For comparison, the strain profile of single QD buried in an infinite medium (legend “infinite”) is also presented. The perpendicular strain component is tensile inside the QD due to obvious reason. When the barrier layer thickness is reduced from infinite to 3 nm, the perpendicular strain component inside QD becomes less tensile at the QD base. For sufficiently thin barrier layer (less than or equal to 3 nm) the perpendicular strain component is no longer tensile even at the QD base. The reason for this is the superposition of large compressive stress from the other QDs with its own small tensile stress.

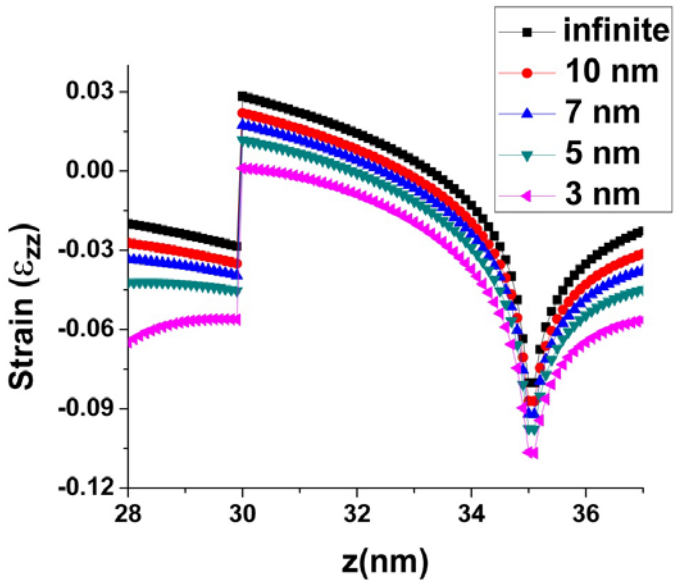

Fig.2.15 Strain component ε_{zz} along a line perpendicular and passing through the center of the base of square based (20 nm) full pyramid shaped QD array for different spacer layer thickness.

Fig.2.15 shows that the biaxial strain inside the QD base decreases when the spacer layer thickness is decreased from 10 nm to 3 nm. Qualitatively, the biaxial strain profile of the QD array inside the QD is same as that of single QD buried in an infinite medium. It is positive at the bottom and most part of the QD but becomes negative close to and at the pyramid tip. Biaxial strain is negative in the matrix material for all spacer layer thickness. Due to the superposition of the strain field from neighboring QDs the biaxial strain becomes more negative in the barrier layer when its thickness decreases. The hydrostatic strain is not presented and discussed here because for the isotropic elastic medium for a QD buried in an infinite matrix, its value is zero outside the dot and constant inside the dot and hence it does not change with the spacer layer thickness. Even with higher

computational expense with finite element method the strain distributions in and around QD in a QD array [92] are same as the values obtained from our method.

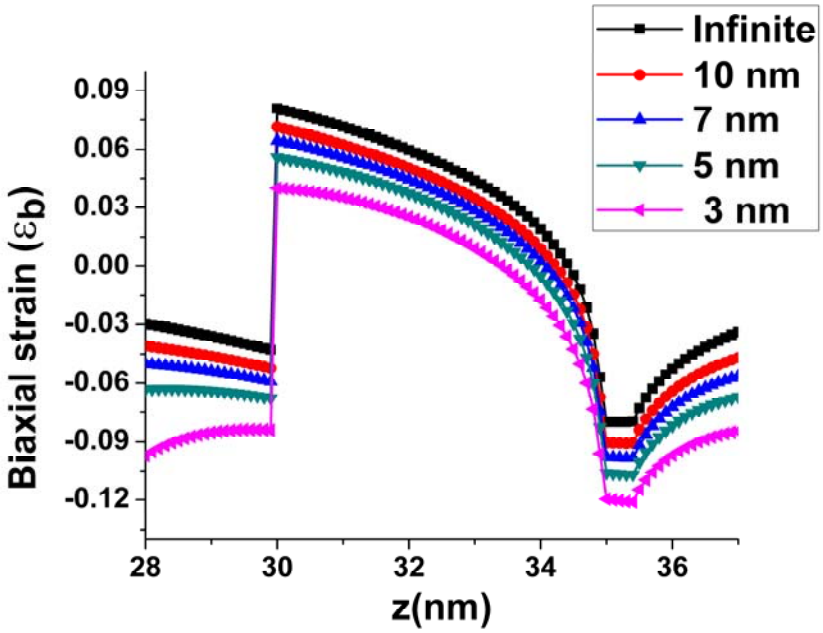

Fig. 2.16 Biaxial strain (ε_b) along a line perpendicular and passing through the center of the base of square based (20 nm) full pyramid shaped QD array for different spacer layer thickness.

The shape of quantum dots covered by barrier material is reported to have a shape close to that of a truncated pyramid. Therefore the strain components of a square based truncated pyramid shaped quantum dot are also presented in this section. Fig.2.17 shows the strain components ε_{xx} of an array of 5 layers of QDs (each QD square based truncated pyramid shaped with base length 20 nm and height 5 nm) with spacer layer thickness of 5 nm. For comparison, the strain profile of a single QD buried in an infinite medium (legend "infinite) is also presented.

Since the QDs in the mid layer represent the QDs in the multilayered structure, here, the discussion of strain profiles is focused on the mid layer QD labeled as "M" in Fig.2.11, in the array of 5 QD layers. Therefore, as in the case of full pyramid shaped QD, further discussion of the strain profile of a QD array is focused on properties of this QD layer. From Fig.2.17, it is clearly seen that qualitatively, the strain component ε_{xx} inside the QD of a QD array is same as that of single QD buried in an infinite medium. Quantitatively, the planar strain is reduced significantly in the array in comparison to single QD. In the QD array, the strain component, ε_{xx}, is relaxed in comparison to isolated QD due to the interaction of the strain fields from the neighboring dots. On the other hand, in the

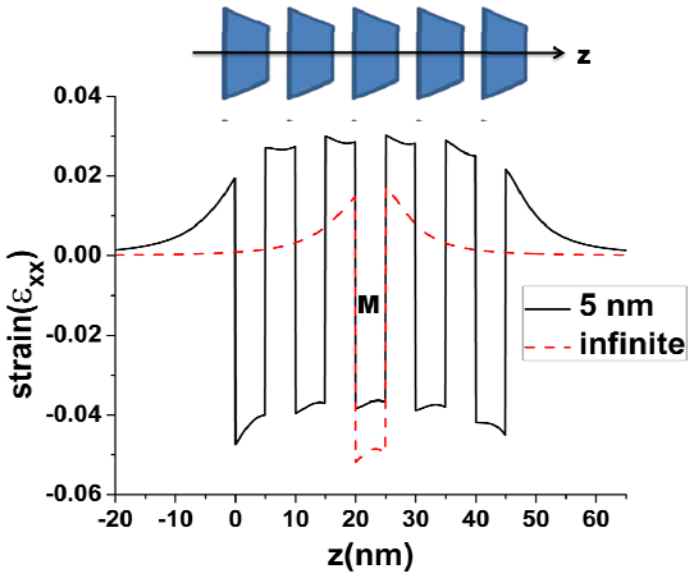

Fig. 2.17 Strain component ε_{xx} of QD array of truncated pyramid shaped five QD layers with 5 nm spacer layer thickness along a line perpendicular and passing through the center of the base.

barrier material the strain profile of QD array is significantly changed in comparison to a single QD. In the array, outside the QDs, the tensile strain from the consecutive layers superimpose causing the barrier material to be more dilative. A closer view of the variation of strain profile of the array with different spacer layer thickness is presented in Fig.2.18 where the strain profile of the mid QD layer are presented for different spacer layer thickness; namely 3 nm, 5 nm, 7 nm and 10 nm. For comparison the strain profile of single QD buried in an infinite medium (legend "infinite") is also presented.

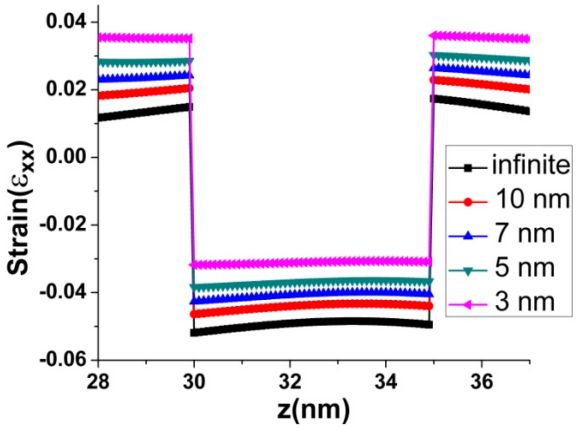

Fig. 2.18 Strain component ε_{xx} along a line perpendicular and passing through the center of the base of square based (20 nm) truncated pyramid shaped QD array for different spacer layer thickness.

Fig.2.18 and 2.19 show that the strain profiles ε_{xx} and ε_{zz} change drastically inside the QD and in the spacer layer when the spacer layer thickness is reduced. Due to the superposition of the strain field from neighboring layers, along the [001] plane (the strain component ε_{xx}) the barrier becomes highly tensile when the spacer layer thickness is decreased. Inside the QD, compressive strain is

reduced with the reduction in barrier layer thickness. On the other hand, the strain component ε_{zz} inside the QD in the array decreases from being tensile (+ve value) to compressive (-ve value) when the barrier layer thickness is reduced to 3 nm. This is due to the superposition of large compressive strains caused by QDs in the barrier material around them and small tensile strains due to the dot itself.

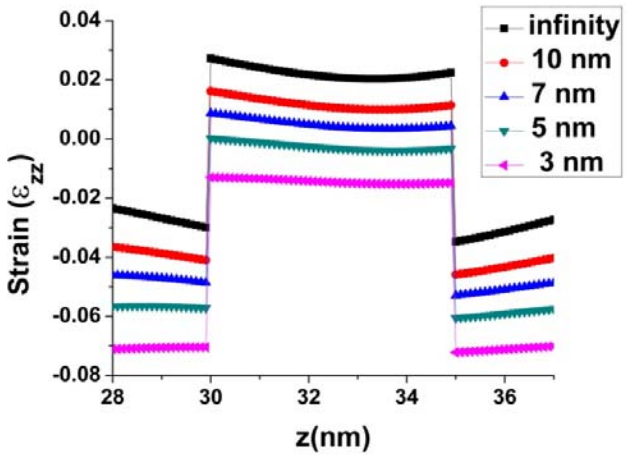

Fig. 2.19 Strain component ε_{zz} along a line perpendicular and passing through the center of the base of square based (20 nm) truncated pyramid shaped QD array for different spacer layer thickness.

Fig.2.20 shows that the biaxial strain inside the QD decreases when the spacer layer thickness is decreased from 10 nm to 3 nm. Qualitatively, the biaxial strain profile of the QD array inside the QD is same as that of a single QD buried in an infinite medium. It is positive inside the entire QD volume. Biaxial strain is negative in the matrix material for all spacer layer thickness. Due to the superposition of the strain field from neighboring QDs the biaxial strain becomes more negative in the barrier layer when its thickness decreases.

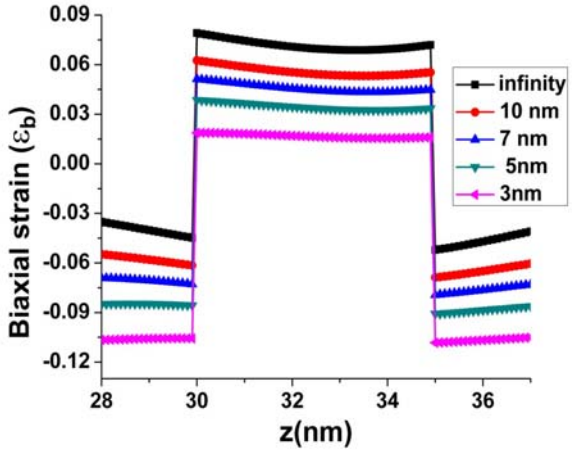

Fig.2.20 Biaxial strain (ε_b) along a line perpendicular and passing through the center of the base of square based (20 nm) truncated pyramid shaped QD array for different spacer layer thickness.

2.6 Conclusion

In this chapter, the strain distribution for single and vertically aligned quantum dots is calculated based on the continuum theory of elasticity. The strain distribution of two different shapes namely, full pyramid and truncated pyramid QDs show different pattern in strain distribution in and around a single quantum dot. These results were reflected in vertical arrays of quantum dots as well. The dependence of elastic strain distribution on the vertical spacing between the QDs clearly shows the superposition of strain fields in neighboring dots when the spacer layer thickness is less than 10 nm.

Here, I have only considered the situation with constant Indium composition within the InAs quantum dot. The experimental results indicate that there is strain driven diffusion of indium to the barrier layer. A further development in the analytical model would be to effectively model the QD with exact composition of the material which has been observed experimentally.

The change in different strain profiles, especially the biaxial strain, with the spacer layer thickness has discernible effect on the band structure. In particular, the magnitude of splitting of valence band into heavy and light holes at the Brillouin zone center (Γ-point) and the band gap is changed with the when spacer layer thickness is decreased. This effect is assessed detail in chapter 3.

Chapter 3

BAND STRUCTURE CALCULATION

3.1 Introduction

The exploration of advanced concept solar cells using semiconductor nanostructures relies on the proper understanding of their interaction with photons. The optoelectronic properties of the nanostructures strongly depend on electronic structure of the bulk and confined electronic states. The inter-band (conduction band to valence band and vice versa) and intra-band (within the conduction or valence band) transitions in the nanostructure materials are controlled by energy spacing of the confined states in conduction and valence bands together with the density of states and the wave functions of these confined states. In this chapter, the band structure of a single and vertically coupled quantum dots are calculated with the effect of strain.

This chapter starts with a brief overview of tight binding and pseudopotential methods for band structure calculations. These sections (3.2 and 3.3) are followed by details of k•p method (section 3.4), which is used to calculate the band structure of the semiconductor heterostructures presented in this dissertation. Section 3.5 considers the effect of elastic strain and its incorporation on the energy band calculation of bulk and heterostructures. The k•p method together with the results of strain calculations from chapter 2 is used to calculate the band structure of the quantum dot heterostructures with the effect of strain. The results of the band edge alignment of the QD heterostructures are presented and discussed in section 3.6. The confined electronic states in the conduction band

(CB) and the valence band (VB) are obtained by solving the Schrödinger equation for strain modified confinement potentials and the effective masses. A single band effective mass method, as outlined in section 3.7, is used for the solution of Schrödinger equation to obtain the confined electronic states in quantum dot. Section 3.8 presents the results of band edge alignment of vertical QD array. Section 3.8 concludes the chapter by summarizing the results and their significance for the development of material model for advanced nanostructured concepts in solar cells.

3.2 Tight binding method

Slater and Koster were the first to advocate the use of the tight binding method as an empirical technique that can be used for band structure calculation of semiconductor materials [93]. In semiconductor materials the outermost valence electrons are either s or p type. This is not only true for elements in atomic form but also for the electrons in elements in crystalline form as the electrons retain the s and p character even though they are Bloch (free) electrons. The tight binding method (TBM) uses atomic functions as basis sets for the Bloch functions. The periodic part of the Bloch function is represented by some combination of the atomic orbitals centered at the lattice points. If $\varphi_n(r-R)$ is such an orbital centered at R, the Bloch function can be written as,

$$\psi_k(r) = \sum_{R_n} \phi_n(r-R) e^{ik.R_n} \qquad (3.1)$$

When the atoms of the elements are brought together in a crystal, the valence electronic states are perturbed by the presence of neighboring atoms and the

original atomic functions describing the valence electrons are no longer eigenstates of the Hamiltonian. But the atomic functions can be used as a good approximate set of basis states to describe the crystalline electrons.

A simple mathematical model of tight binding method starts by assuming that the solution of the atomic Hamiltonian

$$H_{at}\psi_n = E_n\psi_n \tag{3.2}$$

is already known. However, in crystalline structure we have,

$$H_{crystal} = H_{at} + \Delta U(r) \tag{3.3}$$

In equation (3.3), $\Delta U(r)$ is the perturbation introduced due to the interaction of the neighboring atoms. So, the new Bloch wave functions are chosen as;

$$\psi_k(r) = \sum_R \phi(r-R)e^{ik.R} \tag{3.4}$$

Where $\varphi(r)$ are made up of atomic functions as,

$$\phi(r) = \sum_{n=1}^{N} b_n\psi_n(r) \tag{3.5}$$

With equations (3.4) and (3.5), the Schrodinger equation for the crystal,

$$H\psi_k = E(k)\psi_k \tag{3.6}$$

is solved using the orthogonality of atomic functions that are used to expand the Bloch functions and the fact that the atomic functions centered at different lattice sites are not orthogonal, expressed mathematically in equation (3.7) and (3.8) respectively.

$$\int d^3 r \psi_m^*(r) \psi_n(r) = \delta_{mn} \tag{3.7}$$

$$\int d^3 r \psi_m^*(r) \psi_n(r - R) \neq \delta_{mn} \quad \text{for R} \neq 0 \tag{3.8}$$

In this method, second nearest neighbor approximation for zincblende crystals in sp^3 basis (one s and three *p* orbitals as p_x, *py* and p_z) leads to eight basis functions for each of the two atoms within the Wigner-Seitz cell. This approximation assumes that there is spin degeneracy in the band structure of the crystal. This assumption leads to sixteen basis functions for zincblende semiconductors. In order to determine the tight binding matrix elements, which are the interaction parameters of the potential of neighboring atoms, the positions of the neighboring atoms with respect to each atom in the basis set must be known.

3.3 Pseudopotential method

This method was introduced by Phillips and Kleinman [94] to explain the validity and the modifications of nearly-free electron model to calculate the band structure of semiconductors. This method assumes the nature of electronic states in higher energy states (conduction and valence bands) is almost same as the free electron case with the core of the atoms replaced by a repulsive potential. This method is less accurate when the pseudopotential has to be calculated from first principles; however the accuracy is increased when it is used as an empirical method having free parameters which are obtained from the comparison of theoretical and experimental results. Since the crystal potential undergoes sharp change at the vicinity of the lattice points and varies smoothly over the rest of the

crystal, the electron wave function can be represented by a set of few plane waves except in the vicinity of ion cores where it is represented by oscillating functions as in the atomic wave functions. In this method, the strong true potential of the core is replaced by a weaker effective potential also called “pseudopotential” for the valence electrons. To solve the Schrödinger equation with this method, a pseudo wave function that is the approximation of true wave function outside the core region is used. As the pseudopotentials represent a weak perturbation in the free electron band structure, the Schrödinger equation can be diagonalized by expanding the pseudo wave functions in terms of plane waves.

3.4 The K.P method for Bulk semiconductors

The k•p method, introduced by Bardeen [95] and vitalized by Kane [96], Luttinger and Kohn [97] is extensively used to calculate the band structure of bulk and nanostructure semiconductor materials. This method can incorporate the effects of band mixing, strain and the influence of external fields (electric or magnetic). In semiconductors, the lowest conduction band will have contributions from the remote conduction bands as well as from the valence bands depending on the energetic separation of these bands from the lowest conduction band. On the other hand, the valence band edge of any of semiconductor materials is expected to comprise two or three of the valence bands with comparable contributions. Depending on the accuracy required in the calculation and the energetic separation of the bands in the bulk materials, different number of bands may be included in the calculation. Sometimes it is sufficient to include heavy holes and light holes, sometimes we have to include spin orbit split-off band and

even have to include the effect of conduction band in the description of the band structures. This section gives the brief overview of the k•p method for bulk semiconductor materials with direct band gap.

For a periodic potential *V(r)*, the electron wave function satisfies the single electron Schrödinger equation

$$H\Psi(r) = \left[\frac{-\hbar^2}{2m}\nabla^2 + V(r)\right]\Psi(r) = E(k)\Psi(r) \qquad (3.9)$$

In equation (3.9), $p = \frac{\hbar}{i}\nabla$ is the quantum mechanical momentum operator.

The general solution of equation (3.9) is the Bloch function,

$$\Psi_{nk}(r) = e^{ik.r}u_{nk}(r) \qquad (3.10)$$

with $u_{nk}(r+R) = u_{nk}(r)$. Here, R is lattice translation vector given by, $R=n_1a_1+n_2a_2+n_3a_3$, with n_1, n_2, n_3 as the integers and a_1, a_2, a_3 as lattice vectors. When we substitute equation (3.10) into (3.9), we obtain

$$\left(\frac{p^2}{2m} + \frac{\hbar}{m}k.p + \frac{\hbar^2k^2}{2m} + V(r)\right)u_{nk}(r) = E_n(k)u_{nk}(r) \qquad (3.11)$$

Using $H_o = \frac{p^2}{2m} + V(r)$, equation (3.11) can be written as,

$$\left(H_o + \frac{\hbar}{m}k.p + \frac{\hbar^2k^2}{2m}\right)u_{nk}(r) = \left(E_n(k)\right)u_{nk}(r) \qquad (3.12)$$

When we include the spin orbit interaction (Kane's model for band structure) then, the Hamiltonian due to spin orbit interaction is

$$H_{so} = \frac{\hbar}{4m^2c^2}\sigma \bullet \nabla V \times \hat{p} \tag{3.13}$$

where σ is a Pauli matrix with its components $\sigma_x, \sigma_y, \sigma_z$ and can explicitly be written as,

$$\sigma_x = \begin{bmatrix} 0 & 1 \\ 1 & 0 \end{bmatrix}, \sigma_y = \begin{bmatrix} 0 & -i \\ i & 0 \end{bmatrix}, \sigma_z = \begin{bmatrix} 1 & 0 \\ 0 & -1 \end{bmatrix} \tag{3.14}$$

Including the effect of spin orbit interaction in the total Schrödinger equation (3.12) and considering the fact that the crystal momentum $\hbar k$ is very small in comparison to the atomic momentum p in the far interior of the atom where most of the spin orbit interaction happens, equation (3.12) can be written as,

$$\left\{ H_0 + \frac{\hbar^2 k^2}{2m} + \frac{\hbar}{m} k \bullet p + \frac{\hbar}{4m^2c^2}\left[\nabla V \times p\right] \bullet \sigma \right\} u_{nk}(r) = E_n(k) u_{nk}(r) \tag{3.15}$$

The solution of equation (3.15) at Γ-point ($k=0$) without spin orbit interaction is known and is given by:

$$H_o u_{no}(r) = \left(\frac{p^2}{2m} + V(r) \right) u_{no}(r) = E_{n0} u_{n0}(r) \tag{3.16}$$

In equation (3.16), for direct band gap semiconductors, E_{n0} are band edge energies and $u_{n0}(r)$ are the corresponding wave functions, the Bloch functions at the band edge. The u_{n0}'s, for different n, form a complete orthonormal set and one can express the solutions away from the Γ-point ($u_{nk}(r)$) in terms of u_{n0} as,

$$u_{nk}(r) = \sum_m c_{mn}(k) u_{m0}(r) \tag{3.17}$$

In equation (3.17), the band edge functions, u_{m0}, are: for conduction band: $|S\uparrow\rangle$, $|S\downarrow\rangle$ with eigen energy E_C and for valence band: $|X\uparrow\rangle, |Y\uparrow\rangle, |Z\uparrow\rangle, |X\downarrow\rangle, |Y\downarrow\rangle, |Z\downarrow\rangle$ with eigen energy E'_V. In this notation, S refers to the fact that these functions have symmetry properties of s-function of the tetrahedral group, T_d. This belongs to Γ_1 symmetry in the notation of Koester [98]. The functions X, Y and Z have symmetry of p function in the solution of hydrogen atom problem. These functions transform according to Γ_4 symmetry in the notation of Dresselhaus [99].

Substituting equation (3.17) into (3.15) and then multiplying on the left by u_{n0} and using orthonormality condition, we get the Hamiltonian matrix:

$$H_{nm} = \left(E_{n0} + \frac{\hbar^2 k^2}{2m}\right)\delta_{n,m} + \frac{\hbar}{m}\langle u_{n0}|k.p|u_{m0}\rangle + \frac{\hbar^2}{4m^2c^2}\langle u_{n0}|[\nabla V \times p]\bullet\sigma|u_{m0}\rangle \qquad (3.18)$$

The second term in equation (3.18) is referred as k•p interaction term. The k•p interaction is obtained with perturbation theory

The matrix elements of (3.18) in the basis,

$$\{u_1, u_2, ..., u_8\} = \{|S\uparrow\rangle, |X\uparrow\rangle, |Y\uparrow\rangle, |Z\uparrow\rangle, |S\downarrow\rangle, |X\downarrow\rangle, |Y\downarrow\rangle, |Z\downarrow\rangle\} \qquad (3.19)$$

are given by,

$$H = \begin{bmatrix} H_1 + H_{SO} + Hr & \Gamma \\ \Gamma^* & H_1 + H^*_{SO} + Hr \end{bmatrix} \qquad (3.20)$$

In equation (3.20), H_1 includes the diagonal term (first term in equation 3.18) and the k•p interaction terms within the 8 bands (top of the valence band and the

bottom of the conduction bands) in the basis set defined in equation (3.19), H_{so} and Γ account for the spin orbit interaction terms. *Hr* includes the effect of remote bands (out of 8 bands under consideration) on the bands in basis (3.19).

The term H_1 in matrix H in equation (3.20) is given by [100],

$$H_1 = \begin{bmatrix} E_c + \frac{\hbar^2 k^2}{2m} & ik_x P_0 & ik_y P_0 & ik_z P_0 \\ ik_x P_0 & E_V^{'} + \frac{\hbar^2 k^2}{2m} & 0 & 0 \\ ik_y P_0 & 0 & E_V^{'} + \frac{\hbar^2 k^2}{2m} & 0 \\ ik_z P_0 & 0 & 0 & E_V^{'} + \frac{\hbar^2 k^2}{2m} \end{bmatrix} \quad (3.21)$$

Here, *Ec* and *Ev'* are the conduction and valence band edge energies when the pin-orbit interaction is not included. The parameter P_0 accounts the mixture of conduction and valence bands at $k \neq 0$ and is obtained from

$$P_0 = -i(\hbar/m)\langle S|p_z|Z\rangle = -i(\hbar/m)\langle S|p_x|X\rangle = -i(\hbar/m)\langle S|p_y|Y\rangle \quad (3.22)$$

The parameter P_0 can be expressed in the energy units as, $E_P = \frac{2m}{\hbar^2} P_0^2$.

The spin-orbit interaction terms, H_{so} and Γ, in (3.20) can be explicitly written in matrix form and are presented in equation (3.23) and (3.24) respectively,

$$H_{SO} = \frac{\Delta}{3}\begin{bmatrix} 0 & 0 & 0 & 0 \\ 0 & 0 & -i & 0 \\ 0 & i & 0 & 0 \\ 0 & 0 & 0 & 0 \end{bmatrix} \quad (3.23)$$

$$\Gamma = \frac{\Delta}{3}\begin{bmatrix} 0 & 0 & 0 & 0 \\ 0 & 0 & 0 & 1 \\ 0 & 0 & 0 & i \\ 0 & -1 & i & 0 \end{bmatrix} \tag{3.24}$$

In the basis states defined in (3.19), the spin orbit parameter Δ is obtained from

$$\begin{aligned} \Delta &= \frac{3\hbar i}{4m^2c^2}\left\langle X\left|\frac{\partial V}{\partial x}p_y - \frac{\partial V}{\partial y}p_x\right|Y\right\rangle \\ &= \frac{3\hbar i}{4m^2c^2}\left\langle Y\left|\frac{\partial V}{\partial y}p_z - \frac{\partial V}{\partial z}p_y\right|Z\right\rangle \\ &= \frac{3\hbar i}{4m^2c^2}\left\langle Z\left|\frac{\partial V}{\partial z}p_x - \frac{\partial V}{\partial x}p_z\right|X\right\rangle \end{aligned} \tag{3.25}$$

The eigenvalues of the spin orbit interaction matrices are 0 (doubly degenerate, related to eigenstates of the conduction band), *Δ/3* (four fold degenerate) and *-2Δ/3* (doubly degenerate) related to the valence band. Thus, the actual position of the valence band is $E'_V+\Delta/3$ which is measured experimentally and will be denoted as *Ev*, hereafter.

The basis states presented in (3.19) interact strongly with one another and can be arranged in one class, let's say A, and the states other than the ones in A can be considered to be in another class, let's say B. The states in class A interact weakly with the states in class B. The influence of states in class B on the states in class A can be treated as perturbation. Using the Lowdin's perturbation theory [101], the interactions connecting states in A with the states in group B are removed. Let U_{ij} are the initial interaction matrix within the states in group A and U'_{ij} be the renormalized matrix with second order perturbative corrections. The

perturbative correction of the remote bands to the states in class A can be expressed as,

$$U'_{ij} = U_{ij} + \sum_{\beta}^{B} \frac{U_{i\beta}U_{\beta j}}{E_i - U_{\beta\beta}} \tag{3.26}$$

In equation (3.26), the states i, j are in group A, β are in group B and E_i is the eigenvalue of state i. The renormalized Hamiltonian which is still 8x8, is solved by,

$$\sum_{j}^{A} \left(U'_{ij} - E_i \delta_{ij} \right) c_{ji} = 0 \tag{3.27}$$

Here, c_{ij} are the expansion coefficients when the remote band wave functions Ψ_i' is expressed in terms of Ψ_j (the wave functions in class A).

$$\Psi'_i = \sum_{j}^{A,B} c_{ji} \Psi_j \tag{3.28}$$

The c_{ji}'s in equation (3.28) are given by,

$$c_{ji} = \sum_{k}^{A} \frac{U_{jk}}{E_i - U_{jj}} c_{ki} \tag{3.29}$$

In (3.29), j is in B and i, k in A. The Lowdin's perturbation terms converges rapidly if $\left|U_{ij}\right| << \left|E_i - E_j\right|$. Thus, the remote band interaction Hamiltonian, H_r, in matrix expression (3.20) can be written as,

$$H_r = \frac{\hbar^2}{m} \begin{bmatrix} A'k^2 & Bk_yk_z & Bk_xk_z & Bk_xk_y \\ Bk_yk_z & M'\left(k_y^2 + k_z^2\right) + L'k_x^2 & N'k_xk_y & N'k_xk_z \\ Bk_xk_z & N'k_xk_y & M'\left(k_x^2 + k_z^2\right) + L'k_y^2 & N'k_yk_z \\ Bk_xk_y & N'k_xk_z & N'k_yk_z & M'\left(k_x^2 + k_y^2\right) + L'k_z^2 \end{bmatrix} \tag{3.30}$$

The interaction parameters in expression (3.30) are explicitly written in the following expressions.

$$A' = \frac{1}{m}\sum_{nj}\frac{\left|\langle S|\, p_x\,|n\Gamma 5j\rangle\right|}{Ec - E_{n,\Gamma 5}}$$
$$B = \frac{2}{m}\sum_{nj}\frac{\langle S|\, p_x\,|n\Gamma_{5j}\rangle\langle n\Gamma_{5j}|\, p_x\,|Z\rangle}{\frac{E_c + E_V}{2} - E_{n\Gamma 5}} \qquad (3.31)$$
$$H_1 = \frac{1}{2m}\sum_{nj}\frac{\left|\langle X|\, p_x\,|n\Gamma 5j\rangle\right|^2}{E_V - E_{n,\Gamma 5}}$$

$$H_2 = \frac{1}{2m}\sum_{nj}\frac{\left|\langle X|\, p_x\,|n\Gamma 4j\rangle\right|^2}{E_V - E_{n,\Gamma 4}}$$
$$G = \frac{1}{2m}\sum_{nj}\frac{\left|\langle X|\, p_x\,|n\Gamma 3j\rangle\right|^2}{E_V - E_{n,\Gamma 3}} \qquad (3.32)$$
$$F' = \frac{1}{m}\sum_{nj}\frac{\left|\langle X|\, p_x\,|n\Gamma 1j\rangle\right|^2}{E_V - E_{n,\Gamma 1}}$$
$$M = H_1 + H_2, \qquad N' = F' - G + H_1 - H_2, \qquad L' = F' + 2G,$$

As shown in the expressions (3.31) and (3.32), the remote band interaction terms contain all other states excluding the states in the 8 dimensional manifold. The summations in the above parameters are over all single group states $|n\Gamma_{ij}>$ Here the symbol $n\Gamma_{ij}$ is the j^{th} function of the n^{th} band with symmetry Γ_i [102]. In the matrix in equation (3.30), the term *A'* accounts for the coupling of conduction band with the states not in 8 dimensional manifold and is very small (almost negligible) as compared to its coupling with the valence band states [103]. The term B accounts for the inversion symmetry in zincblende crystals that accounts for the mixing of conduction and valence bands in the presence of shear

deformation potential. For semiconductor heterostructures grown on [001] substrates this is very small and can be neglected [104]. For diamond type crystal structures such as silicon and germanium, this term is zero.

A new basis set of the total angular momentum operator can be formed from the basis set defined in equation (3.19). In this new basis set, the Hamiltonian is diagonal at k=0. The class A states that can be formed out of basis set in (3.19) with the electron spin taken into account, can be written as, for the conduction band:

$$\begin{aligned} \varphi_{c,\alpha} &= \left|\frac{1}{2},\frac{1}{2}\right\rangle = \left|S\uparrow\right\rangle \\ \varphi_{c,\beta} &= \left|\frac{1}{2},\frac{1}{2}\right\rangle = \left|S\downarrow\right\rangle \end{aligned} \tag{3.33}$$

and for the valence band:

$$\begin{aligned} \varphi_{hh,\alpha} &= \left|\frac{3}{2},\frac{3}{2}\right\rangle = \frac{1}{\sqrt{2}}\left|(X+iY)\uparrow\right\rangle \\ \varphi_{hh,\beta} &= \left|\frac{3}{2},-\frac{3}{2}\right\rangle = \frac{1}{\sqrt{2}}\left|(X-iY)\downarrow\right\rangle \end{aligned} \tag{3.34}$$

$$\begin{aligned} \varphi_{hh,\alpha} &= \left|\frac{3}{2},\frac{3}{2}\right\rangle = \frac{1}{\sqrt{2}}\left|(X+iY)\uparrow\right\rangle \\ \varphi_{hh,\beta} &= \left|\frac{3}{2},-\frac{3}{2}\right\rangle = \frac{1}{\sqrt{2}}\left|(X-iY)\downarrow\right\rangle \end{aligned} \tag{3.35}$$

$$\begin{aligned} \varphi_{so,\alpha} &= \left|\frac{1}{2},-\frac{1}{2}\right\rangle = -\frac{1}{\sqrt{3}}\left|(X-iY)\uparrow\right\rangle + \sqrt{\frac{1}{3}}\left|Z\downarrow\right\rangle \\ \varphi_{so,\beta} &= \left|\frac{1}{2},\frac{1}{2}\right\rangle = \frac{1}{\sqrt{3}}\left|(X+iY)\downarrow\right\rangle + \sqrt{\frac{1}{3}}\left|Z\uparrow\right\rangle \end{aligned} \tag{3.36}$$

Thus, the set of basis states expressed in (3.34)-(3.36) give the Kane's band edge eigen functions. In these set of functions the total angular momentum $J=L+S$ (where L is orbital angular momentum and S is the angular momentum) and its projection along z-axis, Jz, are diagonal. With the basis set defined in equations (3.34)-(3.36) and using the Lowdin's perturbation theory to include the effect of remote bands , the 8x8 k•p Hamiltonian can be written as;

$$H=\begin{bmatrix} |S\downarrow\rangle & |S\uparrow\rangle & \left|\frac{3}{2},-\frac{3}{2}\right\rangle & \left|\frac{3}{2},-\frac{1}{2}\right\rangle & \left|\frac{3}{2},\frac{1}{2}\right\rangle & \left|\frac{3}{2},\frac{3}{2}\right\rangle & \left|\frac{1}{2},-\frac{1}{2}\right\rangle & \left|\frac{1}{2},\frac{1}{2}\right\rangle \\ A & 0 & T^{+}+V^{+} & 0 & -\sqrt{3}(T-V) & \sqrt{2}(W-U) & (W-U) & \sqrt{2}(T^{+}+V^{+}) \\ 0 & A & \sqrt{2}(W-U) & & 0 & (T-V) & -\sqrt{2}(T-V) & W^{+}+U \\ T+V & \sqrt{2}(W^{+}-U) & -P+Q & -S^{+} & R & 0 & \sqrt{3/2}S & -\sqrt{2}Q \\ 0 & -\sqrt{3}(T+V) & -S & -P-Q & 0 & R & -\sqrt{2}R & \sqrt{\frac{1}{2}}S \\ -\sqrt{3}(T^{+}-V^{+}) & 0 & R^{+} & 0 & -P-Q & S^{+} & \sqrt{\frac{1}{2}}S^{+} & \sqrt{2}R^{+} \\ \sqrt{2}(W^{+}-U) & T^{+}-V^{+} & 0 & R^{+} & S & -P+Q & \sqrt{2}Q & \sqrt{\frac{3}{2}}S^{+} \\ W^{+}-U & -\sqrt{2}(T^{+}-V^{+}) & \sqrt{\frac{3}{2}}S^{+} & -\sqrt{2}R^{+} & \sqrt{\frac{1}{2}}S & \sqrt{2}Q & Z & 0 \\ \sqrt{2}(T+V) & W+U & -\sqrt{2}Q & \sqrt{\frac{1}{2}}S^{+} & \sqrt{2}R & \sqrt{\frac{3}{2}}S & 0 & Z \end{bmatrix} \tag{3.37}$$

The parameters used to write the elements of the matrix in equation (3.27) are given by,

$$A=E_C+\left(A'+\frac{\hbar^2}{2m}\right)k^2 \qquad T=\frac{1}{\sqrt{6}}Bk_z\left(k_x+ik_y\right)$$

$$V=\frac{1}{\sqrt{6}}P_0\left(k_x-ik_y\right) \qquad U=\frac{1}{\sqrt{3}}P_0k_z$$

$$W=i\frac{1}{\sqrt{3}}Bk_xk_y \qquad P=-E_V+\gamma_1\frac{\hbar^2k^2}{2m}$$

$$Q=\gamma_2\frac{\hbar^2}{2m}\left(k_x^2+k_y^2-2k_z^2\right) \qquad R=-\frac{\sqrt{3}}{2}\left[\gamma_2\frac{\hbar^2}{m}\left(k_x^2-k_y^2\right)-2i\gamma_3k_xk_y\right]$$

$$S = \sqrt{3}\gamma_3 \frac{\hbar^2}{m} k_z \left(k_x - ik_y\right) \qquad Z = E_V - \Delta - \gamma_1 \frac{\hbar^2}{2m} k^2$$

$$E_V = E_V^{'} + \frac{\Delta}{3}$$

In these parameterization; γ_1, γ_2 and γ_3 are the modified Luttinger parameters which can be expressed in terms of Kane's parameters given in equation (3.31) and (3.32) as,

$$\begin{aligned} \gamma_1 &= -\frac{2}{3}\left(L' + 2M\right) - 1, \\ \gamma_1 &= -\frac{1}{3}\left(L' - M\right), \\ \gamma_1 &= -\frac{1}{3} N' \end{aligned} \tag{3.38}$$

Since the Luttinger parameters are directly related to the effective masses in valence band, it is convenient to express these parameters in terms of the parameters of six band Luttinger-Kohn Hamiltonian[105] and taking into account the effect of remote bands (including conduction band) from Lowdin's perturbation theory. The original Luttinger parameters, $\gamma_i^L (i = 1,2,3)$, are given by,

$$\begin{aligned} \gamma_1^L &= -\frac{2}{3}\left(L + 2M\right) - 1, \\ \gamma_2^L &= -\frac{1}{3}\left(L - M\right), \\ \gamma_3^L &= -\frac{1}{3} N \end{aligned} \tag{3.39}$$

In (3.39), L, N, F are the Dresselhaus parameters [99]. The difference between the Dresselhaus parameters L, N, F and the Kane parameters L', N', F' comes from

the fact that Dresselhaus chooses three states |X>, |Y> and |Z> as a basis for his calculations where as Kane chooses four states |S>,|X>, |Y> and |Z> as a basis set. The Dresselhaus parameters can be related to Kane parameters. The relation is given in equation (3.40).

$$\begin{aligned} L &= F + G, \\ N &= F - G + H_1 - H_2, \\ F &= F' + \frac{P_0^2}{E_V^{'} - E_C} \end{aligned} \tag{3.40}$$

Also, the 8 band Luttinger parameters are related to original Luttinger parameters (the Luttinger parameters from 6 band model), $\gamma_i^L (i = 1,2,3)$ by,

$$\begin{aligned} \gamma_1 &= \gamma_1^L - \frac{E_P}{3E_g + \Delta}, \\ \gamma_2 &= \gamma_2^L - \frac{E_P}{2\left(3E_g + \Delta\right)}, \\ \gamma_3 &= \gamma_3^L - \frac{E_P}{2\left(3E_g + \Delta\right)} \end{aligned} \tag{3.41}$$

The bulk effective masses of heavy and light hole in different crystallographic directions are obtained from the Luttinger parameters. The heavy hole effective mass can be expressed as

$$\begin{aligned} \left(\frac{m_{hh}^*}{m}\right)^{[001]} &= \frac{1}{\left(\gamma_1 - 2\gamma_2\right)} \\ \left(\frac{m_{hh}^*}{m}\right)^{[110]} &= \frac{2}{\left(2\gamma_1 - \gamma_2 - 3\gamma_3\right)} \end{aligned} \tag{3.42}$$

$$\left(\frac{m_{hh}^{*}}{m}\right)^{[111]} = \frac{1}{(\gamma_1 - 2\gamma_3)}$$

Whereas, the light hole effective masses have the expressions

$$\left(\frac{m_{lh}^{*}}{m}\right)^{[001]} = \frac{1}{(\gamma_1 + 2\gamma_2)}$$

$$\left(\frac{m_{lh}^{*}}{m}\right)^{[110]} = \frac{2}{(2\gamma_1 + \gamma_2 + 3\gamma_3)} \qquad (3.43)$$

$$\left(\frac{m_{lh}^{*}}{m}\right)^{[111]} = \frac{1}{(\gamma_1 + 2\gamma_3)}$$

From expressions (3.41) - (3.43) it is clear that the effective masses become larger for smaller momentum matrix elements and larger band separations.

Expression (3.37), as mentioned previously, includes the conduction band, heavy hole, light hole and spin orbit bands. Each of them is doubly degenerate with the consideration of spin giving rise to eight bands. A valid simplification is to decouple the conduction band from the rest of the valence bands (heavy hole, light hole and spin-orbit). In this case the Hamiltonian reduces to 6x6, which is a six band model as schematically shown in Fig.3.1. Spin-orbit interaction scales with the atomic number of atoms and is weak for the materials containing lighter elements. A further simplification on k•p method, for the materials with weak spin orbit interactions spin-orbit band also can be decoupled and the model reduces to a four band k•p model also called Luttinger-Kohn model.

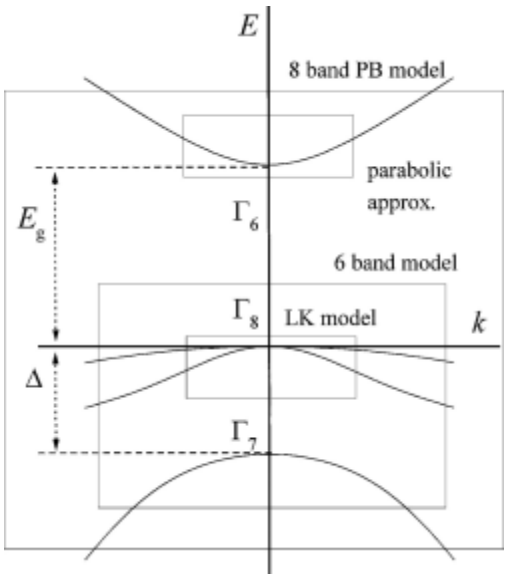

Fig. 3.1 Eight, six and four band k•p method

3.5 Effect of strain on the band structure

The lattice mismatched epitaxial growth of semiconductor heterostructures causes elastic strain in the system. In the strained materials the elastic strain causes a shift in lattice sites. The shift in lattice sites causes a change in crystalline potential in comparison to the unstrained crystal. This change in potential causes the change in energy band parameters such as band gap, the degeneracy of heavy and light holes at Γ-point in valence band and effective mass of electron and holes. The effect of strain on the electronic structure of semiconductors can be incorporated in the k•p model. The effect of elastic strain on the band structure is analyzed following the approach in Ref. [106].

Considering homogeneous strain in space ($\varepsilon_{ij}=\varepsilon_{ji}$, i, j = x,y,z), the periodicity of crystal is still maintained but the unit cell is deformed. The basis vectors of deformed unit cell are related to original basis vectors by,

$$
\begin{aligned}
a_x' &= (1+\varepsilon_{xx})a_x + \varepsilon_{xy}a_y + \varepsilon_{xz}a_z \\
a_y' &= \varepsilon_{yx}a_x + (1+\varepsilon_{yy})a_y + \varepsilon_{yz}a_z \\
a_z' &= \varepsilon_{zx}a_x + \varepsilon_{zy}a_y + (1+\varepsilon_{zz})a_z
\end{aligned}
\tag{3.44}
$$

In expression (3.44), a_i's (i=1, 2, 3 without primes) are the basis vectors in the regular crystal and the ones with prime are the unit vectors in the deformed crystal. The alternative way of dealing with this problem is that we can use the old basis vectors but use the coordinate transformation between old and new system as outlined by Pikus and Bir [107] so that the crystal periodicity of unstrained crystal is restored. The Hamiltonian in equation (3.9) can be transformed to deformed coordinate system using the transformation

$$
x_i = \sum_j \left(\delta_{ij} + \varepsilon_{ij}\right) x_j' \tag{3.45}
$$

Or simply,

$$
\begin{aligned}
r' &= \frac{r}{(1+\varepsilon)} \approx (1-\varepsilon)r \\
r_j' &= \left(\delta_{ij} - \varepsilon_{ji}\right) r_i
\end{aligned}
\tag{3.46}
$$

The Schrodinger equation of the deformed system can be written as,

$$
\left[\frac{p^2}{2m} + V(r,\varepsilon)\right]\Psi_{nk}(r) = E_n(k)\Psi_{nk}(r) \tag{3.47}
$$

For $\varepsilon_{ij} \to 0$, the potential of the deformed crystal, $V(r,\varepsilon)$, can be expanded to the first order in strain as:

$$V(r,\varepsilon) = V(r') + \sum_{ij} V_{ij}(r')\varepsilon_{ij} \tag{3.48}$$

with $V_{ij}(r') = \left[\frac{\partial V(r'+\varepsilon.r',\varepsilon)}{\partial \varepsilon_{ij}}\right]_{\varepsilon ij=0}$. The wave functions are transformed to the new coordinate system as,

$$\begin{aligned}\Psi_{nk}(r) &= \Psi_{nk}\left(\left[1+\varepsilon\right]\bullet r'\right) \\ &= e^{ik.(1+\varepsilon).r'}u_{nk}\left(\left[1+\varepsilon\right].r'\right) \\ &= e^{ik'.r'}u_{nk'}(r') = \tilde{\Psi}_{nk'}(r')\end{aligned} \tag{3.49}$$

Also, the relationship between the momentum operators in the old and new coordinate system up to the terms linear in strain is: $p_i = -i\hbar\frac{\partial}{\partial r_i} = -i\hbar\frac{\partial}{\partial r_j'}\frac{\partial r_j'}{\partial r_i}$.

Using the expression in (3.45), the momentum operator in the old coordinate system can be written in terms of the one in the new coordinate system as;

$$\hat{p}_i = \sum_j \left(\delta_{ij} - \varepsilon_{ij}\right)\hat{p}_j' \tag{3.50}$$

Substituting (3.48), (3.49) and (3.50) in equation (3.47) and applying the Bloch theorem in the new coordinate system, one obtains

$$\left(\hat{H}_b' + \hat{D}_0 + \hat{D}_1\right)u_{nk}(r') = E_n(k)u_{nk}(r') \tag{3.51}$$

In equation (3.51), $\hat{H}_b'$ is the Hamiltonian on equation (3.37) with *r* and *p* replaced with *r'* and *p'*. Other two terms on the left hand side of Hamiltonian (3.51) are due to strain and can be expressed as:

$$\hat{D}_0 = \sum_{ij}\left[-\frac{\hat{p}'_i\,\hat{p}'_j}{m} + V_{ij}(r')\right]\varepsilon_{ij} = \sum_{ij} D_{ij}\varepsilon_{ij}$$
$$\hat{D}_1 = -\frac{\hbar}{m}\sum_{ij} k_i \varepsilon_{ij}\hat{p}'_j. \tag{3.52}$$

The terms that couple spins orbit interactions with strain can be neglected as they have a very small coupling. [58,108].

For the crystal with zincblende symmetry, the terms D_0 and D_1 defined in expression (3.52) add contributions to the 4x4 Hamiltonian and take the form,

$$G_\varepsilon = \begin{bmatrix} w_{ss} & w_x & w_y & w_z \\ w_x^* & w_{xx} & n\varepsilon_{xy} & n\varepsilon_{xz} \\ w_y^* & n\varepsilon_{xy} & w_{yy} & n\varepsilon_{yz} \\ w_z^* & n\varepsilon_{xz} & n\varepsilon_{yz} & w_{zz} \end{bmatrix} \tag{3.53}$$

Each element in equation (3.53) can be expressed as

$$\begin{aligned} &w_{ss} = a'\left(\varepsilon_{xx}+\varepsilon_{yy}+\varepsilon_{zz}\right),\ w_{xx} = l\varepsilon_{xx} + m\left(\varepsilon_{yy}+\varepsilon_{zz}\right),\ w_{yy} = l\varepsilon_{yy} + m\left(\varepsilon_{xx}+\varepsilon_{zz}\right), \\ &w_{zz} = l\varepsilon_{zz} + m\left(\varepsilon_{xx}+\varepsilon_{yy}\right),\ w_x = b'\varepsilon_{yz} - iP_0\sum_j \varepsilon_{xj}k_j\ ,\ w_y = b'\varepsilon_{xz} - iP_0\sum_j \varepsilon_{yj}k_j\ , \\ &w_z = b'\varepsilon_{zy} - iP_0\sum_j \varepsilon_{zj}k_j \end{aligned} \tag{3.54}$$

In equation (3.54), *a'*, *b'*, *l*, *m* and *n* are given by,

$$\begin{aligned} &a' = \left\langle S\middle|\hat{D}_{xx}\middle|S\right\rangle,\ b' = 2\left\langle S\middle|\hat{D}_{xy}\middle|Z\right\rangle, \\ &l = \left\langle X\middle|\hat{D}_{xx}\middle|X\right\rangle,\ m = \left\langle Y\middle|\hat{D}_{xx}\middle|Y\right\rangle,\ n = 2\left\langle X\middle|\hat{D}_{xx}\middle|Z\right\rangle \end{aligned} \tag{3.55}$$

In expression (3.55), D_{ij} are the *ij* components of D_0 defined in equation (3.52). With these definitions, the strain Hamiltonian in the basis defined in (3.33)-(3.36) becomes:

$$H_s = \begin{bmatrix} a_c\varepsilon_h & 0 & -v^+ & 0 & -\sqrt{3}v & \sqrt{2}u & u & \sqrt{2}v^+ \\ 0 & a_c\varepsilon_h & \sqrt{2}u & \sqrt{3}v^+ & 0 & v & -\sqrt{2}v & -u \\ -v & \sqrt{2}u & -p+q & -s^+ & r & 0 & \sqrt{\frac{3}{2}}s & -\sqrt{2}q \\ 0 & \sqrt{3}v & -s & -p-q & 0 & r & -\sqrt{2}r & \frac{s}{\sqrt{2}} \\ \sqrt{3}v^+ & 0 & r^+ & 0 & -p-q & s^+ & \frac{s^+}{\sqrt{2}} & \sqrt{2}r^+ \\ \sqrt{2}u & v^+ & 0 & r^+ & s & -p+q & \sqrt{2}q & \sqrt{\frac{3}{2}}s^+ \\ u & -\sqrt{2}v^+ & \sqrt{\frac{3}{2}}s^+ & -\sqrt{2}r^+ & \frac{s}{\sqrt{2}} & \sqrt{2}q & -p & 0 \\ -\sqrt{2}v & -u & -\sqrt{2}q & \frac{s^+}{\sqrt{2}} & \sqrt{2}r & \sqrt{\frac{3}{2}}s & 0 & -p \end{bmatrix} \tag{3.56}$$

The matrix elements in (3.56) are given by,

$$\begin{aligned} \varepsilon_h &= \left(\varepsilon_{11}+\varepsilon_{22}+\varepsilon_{33}\right), \\ p &= a_v\varepsilon_h, \\ q &= b\left[\varepsilon_{33}-\frac{1}{2}\left(\varepsilon_{11}+\varepsilon_{22}\right)\right], \\ r &= \frac{\sqrt{3}}{2}b\left(\varepsilon_{11}-\varepsilon_{22}\right)-id\varepsilon_{12}, \\ s &= -d\left(\varepsilon_{13}-i\varepsilon_{23}\right), \\ u &= \frac{1}{\sqrt{3}}P_0\sum_j \varepsilon_{3j}k_j, \\ v &= \frac{1}{\sqrt{6}}P_0\sum_j (\varepsilon_{3j}-i\varepsilon_{2j})k_j \end{aligned} \tag{3.57}$$

Here, $a_c=a'$ and $a_v=-1/3(l+2m)$ are the conduction and valence band deformation potential respectively. The terms $b=1/3(l-m)$ and $d=n/\sqrt{(3)}$ are the shear deformation potentials.

3.6 Band edge alignment and confinement potentials in single quantum dot

In this section, the methodology used to calculate band edge alignment of strained III-V and Ge/Si quantum dot/barrier material system is discussed. The effect of strain on band edge alignment of the dot/barrier material systems is calculated and the confinement potentials for electrons, heavy and light holes are presented. For III-V material system, the focus is on InAs/GaAs dot/barrier material system as this is extensively studied experimentally. Together with this, the band edge alignment of InAs/GaAsSb material system grown on GaAs[001] for different antimony composition are also presented to investigate the antimony composition that leads to negligible valence band offset (VBO) between the dot/barrier system. The condition of negligible VBO is of particular interest for quantum dot intermediate band solar cells(QDIBSCs) as it can avoid the voltage loss due to carrier relaxation via the closely spaced confined states in QD valence band [109]. On the other hand, due to its already matured fabrication technology and the abundance, the SiGe/Si system is always of great interest for advanced concept solar cells. The methodology for calculation and the results of the effect of strain on band edge alignment of SiGe/Si system are also discussed and presented here.

3.6.1 Direct band gap III-V material systems

The band edge alignment in direct band gap III-V QD/barrier material system is calculated using k•p method at the band edge (Γ-point) with the effect of strain taken into account. First, the strain distribution in and around the quantum dot is calculated as discussed in chapter 2. The effect of strain on the band structure is obtained from the expressions (3.37) and (3.56). Expression (3.37) at the band edge (Γ-point, *k=0*) together with (3.56) which takes into account the effect of strain in band structure, give the band edge alignments of the conduction and valence bands of direct band gap III-V semiconductors. The conduction band is decoupled from the valence band and the band edge energy of the conduction band is given by,

$$Ec = E_c^0 + \delta Ec \tag{3.58}$$

In equation (3.58), E_c^0 is the band edge energy of the unstrained conduction band and δEc is the change in conduction band edge due to strain. The change in CB edge due to strain can be expressed as,

$$\delta Ec = a_c(\varepsilon_{xx} + \varepsilon_{yy} + \varepsilon_{zz}) \tag{3.59}$$

In equation (3.59), a_c is the hydrostatic deformation potential for the conduction band. The band edge energy of the unstrained conduction band, E_c^0, is given by;

$$E_c^0 = E_{v,av}^0 + \frac{\Delta_0}{3} + E_g \tag{3.60}$$

In equation (3.60), E_g is the unstrained band gap, Δ_0 is the spin orbit splitting energy and $E^0_{v,av}$ is the average over the three uppermost valence bands at Γ-point (light hole, heavy hole and spin-orbit split-off band) for the unstrained bulk semiconductor material [47]. The heavy and light hole energies of the strained material at Γ-point are no longer degenerate and their energies at that point are given by,

$$Ehh = E^0_{v,av} + \frac{\Delta_0}{3} + a_v\varepsilon_h - b\varepsilon_b \tag{3.61}$$

$$E_{lh} = Ev,av - \frac{\Delta_0}{6} + a_v\varepsilon_h + \frac{1}{4}b\varepsilon_b + \frac{1}{2}\sqrt{\left(\Delta_0^2 + \Delta_0 b\varepsilon_b + \frac{9}{4}(b\varepsilon_b)^2\right)} \tag{3.62}$$

In equation (3.61) and (3.62) a_v and b are valence band hydrostatic and shear deformation potentials respectively. The band edge alignment of InAs QDs grown on GaAs[001] substrate with GaAs barrier is calculated using expressions(3.58), (3.61) and (3.62) for the conduction, heavy hole and light hole bands respectively. To calculate the band structure, the hydrostatic and biaxial strains are first calculated at the same grid points those are used to calculate the band structure. The results of these two strain components are coupled to band structure at the same grid points via corresponding deformation potentials. The material parameters used for the band structure calculation, taken from reference [81], are listed on table 3.1. Here, for a tertiary alloy of type $A_{1-x}B_x$, the parameter P is obtained by using an expression,

$$P(A_{1-x}B_x) = (1-x)P(A)+xP(B)-x(1-x)C.$$

In this expression, *C* is a bowing parameter that accounts the deviation of specific material parameter of a tertiary material $A_{1-x}B_x$ from linear interpolation between the binaries *A* and *B*. In table 3.1, The VBO listed for InAs and GaAs are also from reference [81] where those values are listed in comparison to the valence band edge of InSb.

Table 3.1 Material parameters of GaAs, InAs, GaSb and GaAsSb relevant for band structure calculations

Parameter		InAs	GaAs	GaSb	$GaAs_{1-x}Sb_x$ bowing parameter(C)
Band Gap	E_g(eV)	0.417	1.519	0.812	1.43
Spin-orbit interaction	Δ_0(eV)	0.39	0.341	0.76	0.6
Conduction and valence band hydrostatic deformation potential	a_c(eV)	-5.08	-7.17	-7.5	0
	a_v(eV)	1	1.16	0.8	0
Shear deformation potential	b(eV)	-1.8	-2	-2	0
Valence band offset(VBO)	ΔEv (eV)	-0.59	-0.80	-0.03	-1.06

The band structure of a pyramid shaped InAs QD (along a line passing through and perpendicular to the base of pyramid) buried in infinite GaAs matrix is presented in Fig.3.2. In this figure, the band edge alignment of bulk GaAs and InAs are also presented for comparison. For the presentation of band edge alignment, the zero of energy is taken to be the energy of valence band edge of bulk GaAs. It is clear that the conduction band edge of the QD is shifted,

significantly increasing the effective band gap by almost 0.4 eV in comparison to unstrained case. The heavy and light holes are not degenerate at Γ-point. Also, there is a crossing of heavy hole and light hole band edges close to the pyramid tip. This is due to the strong spatial variation of biaxial strain towards the tip of the dot that was observed in calculation of strain distribution presented in chapter 2. The heavy hole band edge is lower in energy (in the inverted scheme of the band diagram) than the light hole at the base of the pyramid where as at the tip of the pyramid the light hole band has higher energy than the heavy hole band. The hole confinement potentials are spatially varying from the bottom of the pyramid to its tip. On the other hand, for the truncated pyramid shaped quantum dots, the heavy hole band edge is always higher in energy than the light hole band edge, as shown in Fig.3.3. As discussed in chapter 2, keeping in mind that the realistic shape of quantum dots embedded in a barrier material is close to that of a truncated pyramid, the further discussion of band structure presented hereafter will be focused on truncated pyramid shaped quantum dots with base dimension 20 nm and height 5 nm.

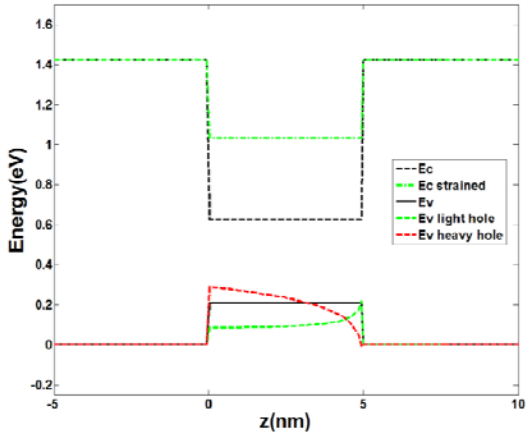

Fig. 3.2 Energy band edge diagram at the Γ point along the z axis for pyramid shaped InAs quantum dot grown on GaAs [001] substrate with GaAs barriers.

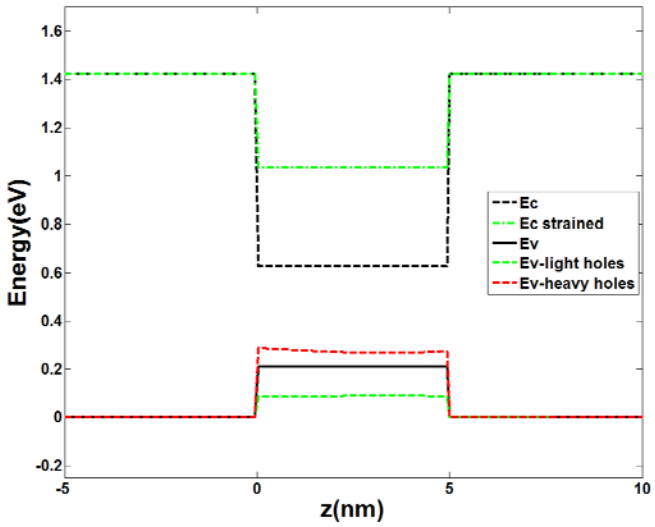

Fig. 3.3 Energy band edge diagram at the Γ point along the z axis for truncated pyramid shaped InAs quantum dot grown on GaAs [001] substrate with GaAs barriers.

Fig.3.4 presents the band structure of InAs QDs grown on GaAs [001] with GaAsSb barrier. This material system is investigated to predict the negligible valence band offset condition that suppresses the carrier relaxation to the ground state of the confined valence band states from the valence band continuum via

closely spaced confined energy states. From the calculation, it is found that the negligible valence band condition is achieved when the antimony composition in GaAsSb is 16%. Here, for the negligible valence band condition we focus on heavy hole band because as discussed earlier, for the materials that are compressively strained the heavy hole band is lower in energy (in the inverted band scheme) than the light hole.

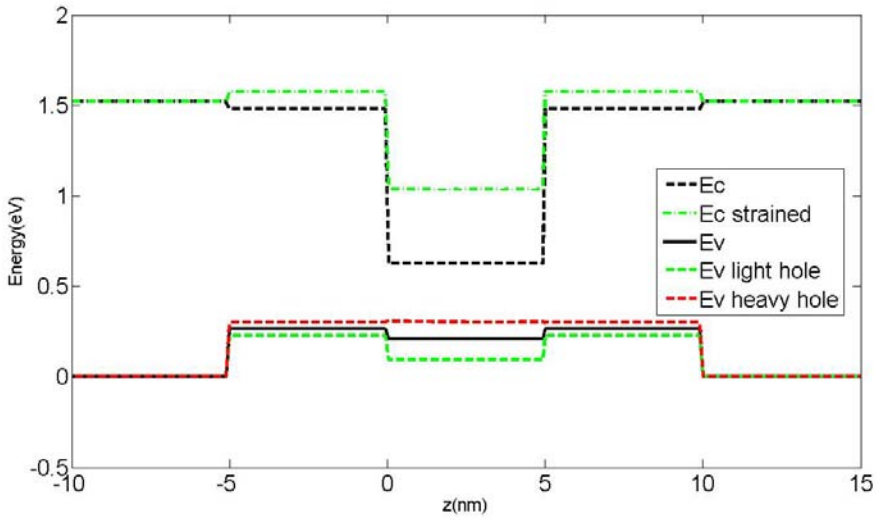

Fig. 3.4 Energy band edge diagram at the Γ point along the z axis for truncated pyramid shaped InAs quantum dot in $GaAs_{0.84}Sb_{0.16}$ matrix, grown on grown on GaAs[001] substrate

.

3.6.2 Silicon germanium/silicon material systems

The Silicon germanium ($Si_{1-x}Ge_x$) alloy grown on silicon has a lattice mismatch up to 4% for $x = 0$. In this material system epitaxial growth mode, as mentioned earlier, is the Stranski-Krastanov growth [110]. The shape and size of germanium quantum dots on silicon are reported to have bimodal distribution of

comprising both the large dome shaped and small pyramid shaped dots[111]. However, with the comparatively low growth temperature the shape and size of SiGe QDs grown on Si [001] substrate are reported to be close to that of a pyramid and truncated pyramid [112 ,113] with base length and height about 20 nm and 3 nm respectively.

In germanium, conduction band minima is in (111) crystallographic direction on the surface of Brillouin zone with band gap of 0.66 eV whereas silicon has its conduction band minima at Δ-valleys (along Γ-X line) is at $k=0.85k_{max}$[001]. The unstrained Ge/Si interface has the type-II band alignment with 0.51 eV in VB and 0.05 eV spatially indirect band offset in CB.

The effect of strain on the SiGe system can be obtained from deformation potential theory. The effect of strain in conduction band can be written as,

$$\delta E_{C,av} = \left(\Xi_d + \frac{1}{3}\Xi_u \right)\left(2\varepsilon_{xx} + \varepsilon_{zz}\right) \tag{3.63}$$

In equation (3.63), the first term inside the bracket is conduction band deformation potential and the second term is hydrostatic strain. The shift of Δ-valleys with respect to the average shift expressed in equation (3.63) can be expressed as,

$$\delta E_C(\Delta_2) = \frac{2}{3}\Xi_u^{\Delta}(\varepsilon_{zz} - \varepsilon_{xx}) \tag{3.64}$$

$$\delta E_C(\Delta_4) = -\frac{1}{3}\Xi_u^{\Delta}(\varepsilon_{zz} - \varepsilon_{xx}) \tag{3.65}$$

In these equations, Ξ_u^{Δ} is the deformation potential for the delta valley in conduction band. In silicon and germanium, the effect of strain is different in different Δ-valleys. For example, the biaxial strain lifts the degeneracy of the Δ-valleys into Δ_4 (in the layer plane) and Δ_2 (perpendicular to the layer plane, growth direction for growth in [001] substrate) valleys. Directly above and below the germanium QDs, in silicon, the Δ_2 valley is lowered in energy due to tensile strain whereas the energy of Δ_4 valleys increases. In Ge**,** the compressive strain pushes up the L-valley and switches the conduction band minimum from L-valley to the Δ_4 valley. For the calculation of valence band edge alignment, which is at Γ-point, the expressions (3.61) and (3.62) are used. The band edge alignments of the pyramid shaped germanium quantum dots of base length 20 nm and height 3 nm grown on silicon [001] substrate buried in an infinite silicon matrix are presented in Fig.3.5. The material parameters used to calculate the band structure of silicon germanium heterostructure, unless otherwise specified, are taken from reference [114] are listed in table 3.2. The band diagram, presented along a line passing through the pyramid vertex and perpendicular to the base of the pyramid, shows that at the regions directly above and below the QD the silicon Δ_2 valley has the minimum energy whereas inside the dot for germanium Δ_4 is the minimum. The band diagram clearly shows a spatially type-II band alignment with a 180 meV deep two dimensional well for electrons in silicon at the top of QD and a 700 meV deep three dimensional confinement potential for heavy hole in germanium QD. As in the case of InAs/GaAs system, the heavy hole and light hole bands at the Γ-point split in energy due to compressive strain inside the dot

(germanium) with heavy hole being the lowest energy band(in inverted band scheme).

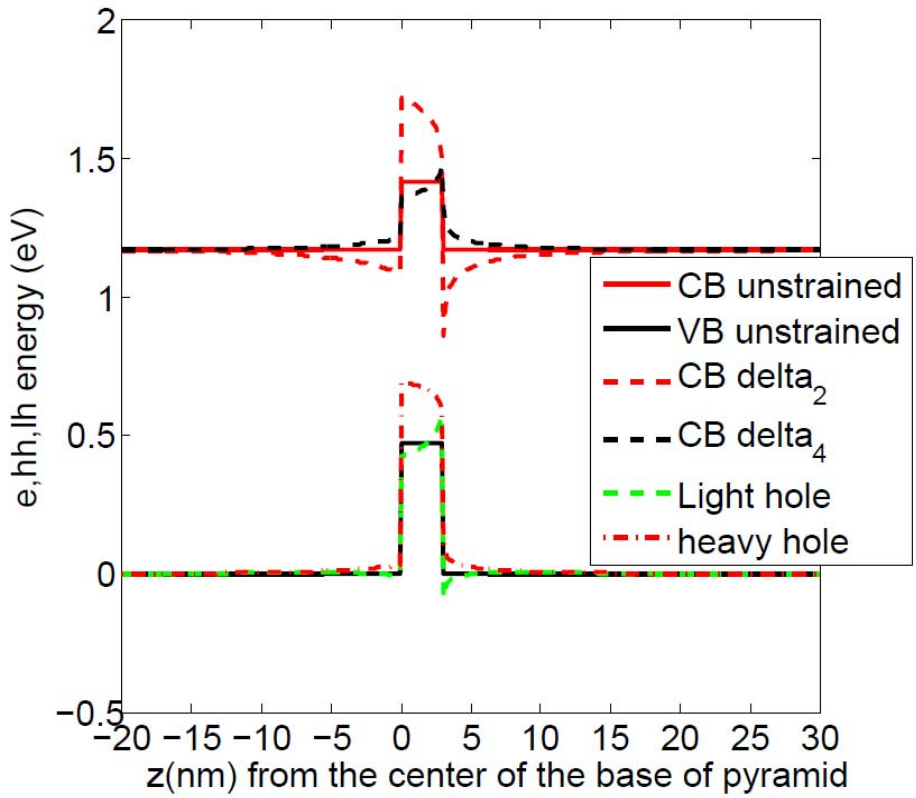

Fig. 3.5 Energy band edge diagram (minimum energy of the valleys in corresponding bands) along z axis for full pyramid shaped germanium quantum dot in silicon matrix, grown on grown on Si [001] substrate.

Table 3.2 Material parameters of silicon and germanium used in band structure calculation

parameter		Silicon	Germanium
Lattice constant	(^{o}A)	5.43	5.65
Elastic constants	C_{11} (GPa)	165.8	131.5
	C_{12}(GPa)	63.9	49.4
Deformation potentials	a_v (eV)	4.54	-3.1
	b(eV)	-2.1	-2.86
	Ξ_u^{Δ}(eV)	8.6	9.4
	Ξ_d^{Δ}(eV)	-6	-4.92
Valence band offset	$\Delta E_{V,av}^{o}$ (eV)	0	0.47 [115]
Spin-orbit splitting	Δ (eV)	0.04	0.3

3.7 Confined states in semiconductor quantum dots

For advanced nanostructure concepts in solar cell application, knowledge of their optoelectronic properties is essential. Optoelectronic properties of the nanostructures are determined by the energetic position and the wave function of the confined states in conduction and valence band. In this section, the methodology used to calculate the confined energy states and wave function is formulated and the results are presented for III-V and SiGe self-assembled quantum dots.

Semiconductor heterostructures such as quantum wells, wires and dots are obtained when a low band gap material with the dimension of few nanometers is

surrounded by a higher band gap materials in different dimensions (quantum wells: one dimension, let's say z-axis, quantum wire: two dimensions, let's say x and y axes, and for quantum dot: all three dimensions). These heterostructures have confined electronic states in valence and conduction bands. The confined energy levels and their wave functions determine the optoelectronic properties of these nanostructures. The calculation of these confined electronic states becomes a complex task due to non uniform confinement potentials and complex geometries of quantum dots.

The methods used to calculate these electronic structures can mainly be categorized in three groups namely; (a) single particle effective mass theory, (b) multiband envelope function theory and (c) first principle methods. Out of these methods, multiband envelope function theory [57,116] is highly used for valence band confined states as it accounts for the interaction of heavy hole, light hole and spin orbit interaction bands. The conduction band is, generally, decoupled from valence band and is solved by using single band effective mass theory [116]. Here, for computational simplicity, single band effective mass theory, which is applied successfully to explain the electronic structure of quantum wires [117] and dots [118] is used. A brief overview of the method that is based on single band effective mass theory and the results of the calculation of confined energy states and the wave functions is presented in the following sub-sections.

3.7.1 Single band effective mass method

In this method, the confined energy eigenvalues and eigenstates are obtained from single parabolic band. In semiconductor heterostructures, the

conduction and valence band edges (strain modified) of the two constituent semiconductors form piecewise constant potentials. The electron in CB and hole in VB in each region (QD and barrier) act as free particle with effective mass determined from bulk band curvature at the band edge. The band offset obtained from the difference in the energy of band edges of two constituent semiconductors with the effect of strain is used to obtain the confining potential.

The confined states and energy levels in the conduction band are obtained by using the single band effective mass theory for the three dimensional confining potential, $V(x, y, z)$, and the effective mass, $m^*_{c,}$ modified by the effect of strain. That is to say, for the conduction band the Schrödinger equation becomes,

$$\left[-\left(\hbar^2 \big/ 2m_c^*\right)\nabla^2 + V(x,y,z)\right]\psi(x,y,z) = E\psi(x,y,z) \qquad (3.66)$$

Equation (3.66) is solved by expanding the envelope function, $\psi(x, y, z)$, in terms of the solution of a particle in an infinite potential cuboidal box surrounding the quantum dot [119].

$$\psi(x,y,z) = \sum_{lmn} a_{lmn}\phi_{lmn} \qquad (3.67)$$

where

$$\phi_{lmn} = \sqrt{\frac{2}{L_x}}\sin\left[l\pi\left(\frac{1}{2} - \frac{x}{L_x}\right)\right]\sqrt{\frac{2}{L_y}}\sin\left[m\pi\left(\frac{1}{2} - \frac{y}{L_y}\right)\right]\sqrt{\frac{2}{L_z}}\sin\left(n\pi\frac{z}{L_z}\right) \qquad (3.68)$$

and a_{lmn}'s are the expansion coefficients with l, m and n =1,2,------,n, with n determined from the required accuracy of the calculation. The calculation domain

is chosen to be: [-Lx/2≤x≤Lx/2], [-Ly/2≤x≤Ly/2] and [0≤z≤Lz] for x, y and z respectively, as shown in Fig.3.6. A matrix of size $l \times m \times n$ is obtained by substituting equation (3.67) into (3.66) and multiplying (3.66) by $\varphi^*_{l',m',n'}$ and then integrating over the volume of cuboid (see Fig. 3.6). The eignevalues and eigenvectors of this matrix give the energy levels and the wave functions of the confined states in the CB of the QD.

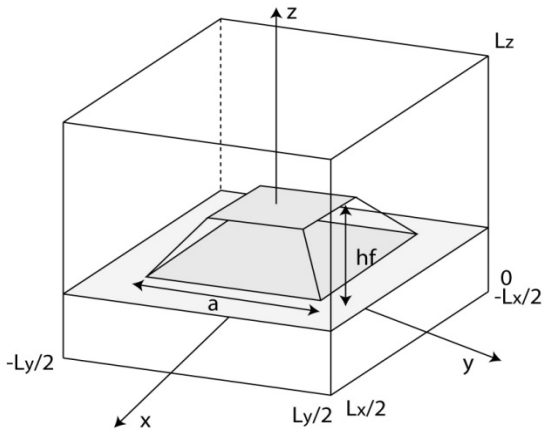

Fig. 3.6 Schematic diagram representing the configuration used in the calculation of the conduction and valence band.

Table 3.3 Material parameters of GaAs, InAs GaSb and GaAsSb used in the calculation of confined electronic states.

Parameter		InAs	GaAs	GaSb	$GaAs_{1-x}Sb_x$ Bowing parameters(C)
Bulk effective mass at Γ point [m]	m^*	0.026	0.067	0.039	0
Luttinger parameters	γ_1^L	20.0	6.98	13.4	0
	γ_2^L	8.5	2.06	4.7	0
	γ_3^L	9.2	2.93	6.0	0
Bulk valence band offset [eV]	VBO	-0.59	0.80	-0.03	-1.06
Bulk Band Gap	E_g(eV)	0.417	1.519	0.812	1.43

Here, the confined energy states of electrons and holes for InAs quantum dots in $GaAs_{0.84}Sb_{0.16}$ grown on GaAs [001] are calculated. The conduction band effective mass is isotropic and the method works very well for CB confined states. For the valence band, the anisotropy in effective masse is taken into account. Here, only the heavy hole confined states are calculated and presented because this band is the lowest in energy for compressively strained QD material. The material parameters used for the calculation of confined states, taken from reference [81], are listed on table 3.3. Here, for a tertiary alloy of type $A_{1-x}B_x$, the parameter P is obtained by using an expression,

$$P(A_{1-x}B_x) = (1-x)P(A)+xP(B)-x(1-x)C.$$

In this expression, *C* is a bowing parameter that accounts the deviation of specific material parameter of a tertiary material $A_{1-x}B_x$ from linear interpolation between the binaries A and B. To calculate the confined states in the conduction band (CB)

of InAs QD, the electron effective mass was taken to be 0.04 as reported in reference [120] rather than the bulk effective mass listed in table 3.3.

3.7.2 Results and discussions

The conduction band energy levels and the wave functions calculated for InAs quantum dots buried in a $GaAs_{0.84}Sb_{0.16}$ matrix on a GaAs[001] substrate are calculated by the method explained in section 3.7.1. The shape and size of the dot considered for this calculation is a square based (*a=20nm*) truncated (height, *hf, 5* nm) pyramid as shown in the Fig.3.6. At 0 K temperature, the calculated values of E_0H_0 (separation between heavy hole ground state and the CB electronic ground state) and E_1H_1 (separation between heavy hole first excited state and electron first excited state) are obtained to be 1.143eV and 1.23eV, respectively, as shown in Fig.3.7 are in good agreement with the observed experimental data [121] presented in Fig.3.8.

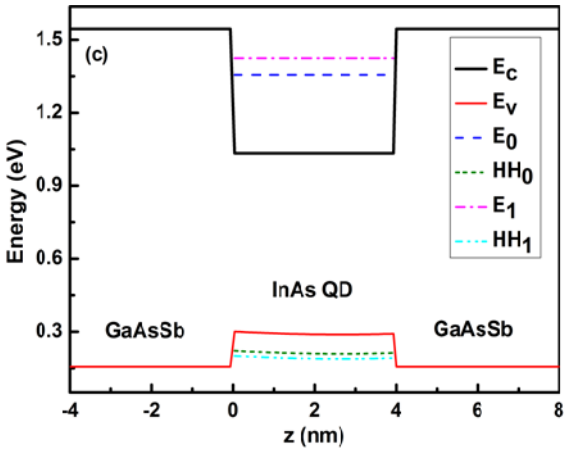

Fig. 3.7 The calculated electron and hole energy levels of an InAs QD buried in $GaAs_{0.92}Sb_{0.08}$ matrix.

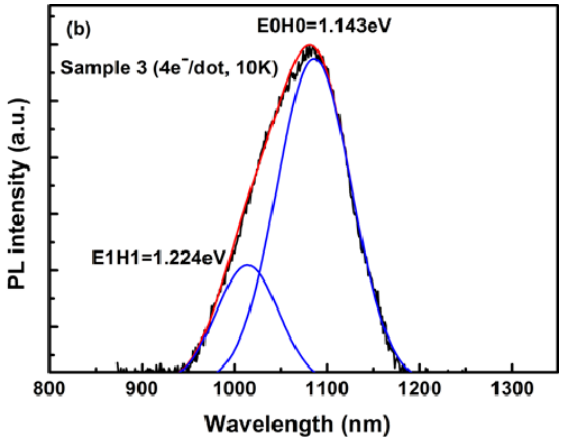

Fig. 3.8 The PL spectra (10K) of InAs QDs in $GaAs_{0.92}Sb_{0.08}$ matrix fitted by a Gaussian distribution function [121]

Table 3.4 Material parameters of Silicon and Germanium used in calculation

Parameters	Silicon	Germanium
m_l (m)Δ	0.92	0.93
m_t(m)Δ	0.19	0.081
$m_{hh}^{[001]}$ (m)	0.23	0.33

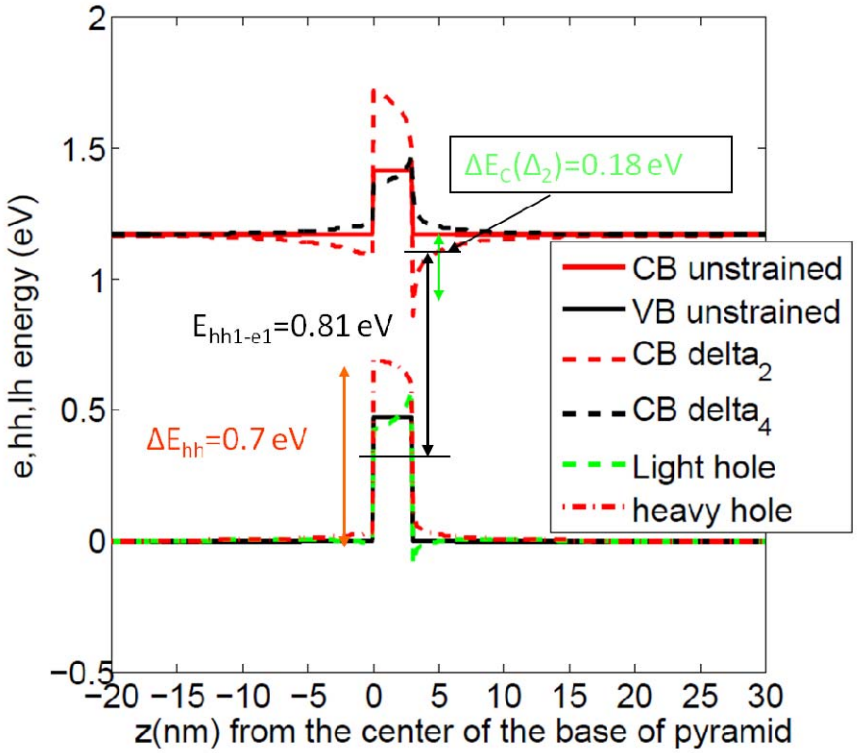

Fig. 3.9 Heavy hole and conduction band confined states in Germanium quantum dot (size: base length 20 nm and height 3.5 nm) in silicon matrix.

Germanium QDs in silicon matrix, grown on [001] silicon substrate, as shown in section 3.6, have type-II band alignment. The electrons are confined in silicon at the top of the QD while the holes are confined inside the QD in germanium. The energy of the confined states of heavy hole is calculated using the method outlined in section 3.7 with the confinement potential obtained with the effect of strain. The material parameters used for calculation are listed in table 3.4. The energy of electron ground state from heavy hole ground state is found to be 0.81 eV as shown in figure 3.9. These results are in good agreement with experimental observations of the photoluminescence peak of germanium QDs in silicon [111].

The ground state electronic wave functions of an InAs QD in GaAsSb matrix is presented in Fig.3.10 together with the probability density of electrons confined in the conduction band. From this figure, it is clear that the ground state electronic wave function is totally restricted inside the QD and has a spherical symmetry. The probability density and the wave function of first and second excited states are presented in Fig.3.11. The wave functions of these states have *p*-symmetry. As the confinement of these states is weak, the wave function extends to the barrier material.

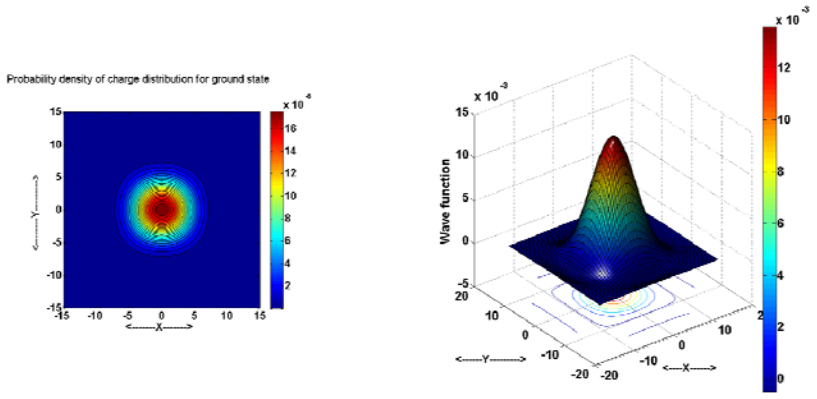

Fig. 3.10 Probability of finding the ground state (E_1) electron in the QD (left panel) and the wave function of the electronic ground state (right panel).

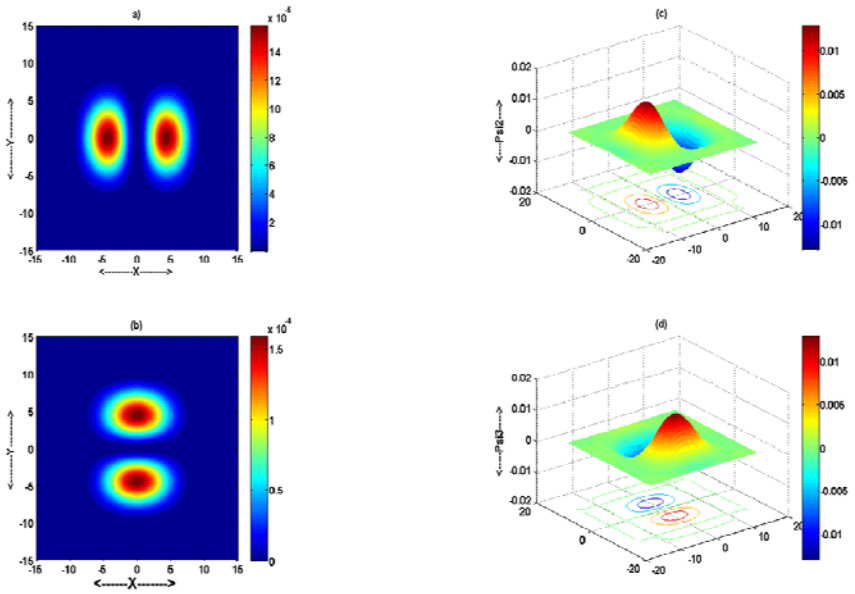

Fig. 3.11 Probability of finding the first (E_2) and second excited state (E_3) electrons in QD (left panel) and the corresponding wave functions of the E_2 and E_3 confined states (right panel).

The confined energy states and wave functions of electrons in conduction band confined states of InAs quantum dot in GaAsSb matrix are calculated and presented. The single particle effective mass method gives accurate results despite its simplistic formulation.

3.8 Band edge alignment of vertically stacked QD array

The band edge alignment of the QD array can be calculated using k•p method for $k = 0$ (Γ-point). Using the expressions (3.58)-(3.62) in section 3.6.1 which account the coupling the hydrostatic and the biaxial strain fields with the band structure, we get the band edge alignment and hence the confinement potentials for the electrons and holes in quantum dots. The hydrostatic and biaxial strain fields are fist calculated for the vertical QD array with the method outlined

in section 2.4. The band structure is calculated at the same grid points that are used to calculate the strain fields and the hydrostatic and biaxial strain fields are coupled to the band structure via corresponding deformation potentials.

Fig.3.12 presents the energy band edge alignment of vertical array of InAs QDs in GaAs matrix along z-axis passing through the center of the base of each QD. Each QD in the array has the shape of a square based truncated pyramid with base dimension 20 nm and height 5 nm with spacer layer thickness of 5 nm. The zero of energy is taken to be the valence band of unstrained bulk GaAs. As the strain calculation was done for an isotropic medium using the method outlined in section 2.1, the hydrostatic strain is constant inside the QD and zero outside for a single QD buried in an infinite matrix. This is reflected in the band diagram of QD array as well. The shift in conduction band edge due to strain in QD array is same as in case of single QD in an infinite matrix. Therefore, the discussion hereafter is focused on valence band, heavy and light holes which are significantly affected by the biaxial strain that depends strongly on the vertical spacing between the QDs.

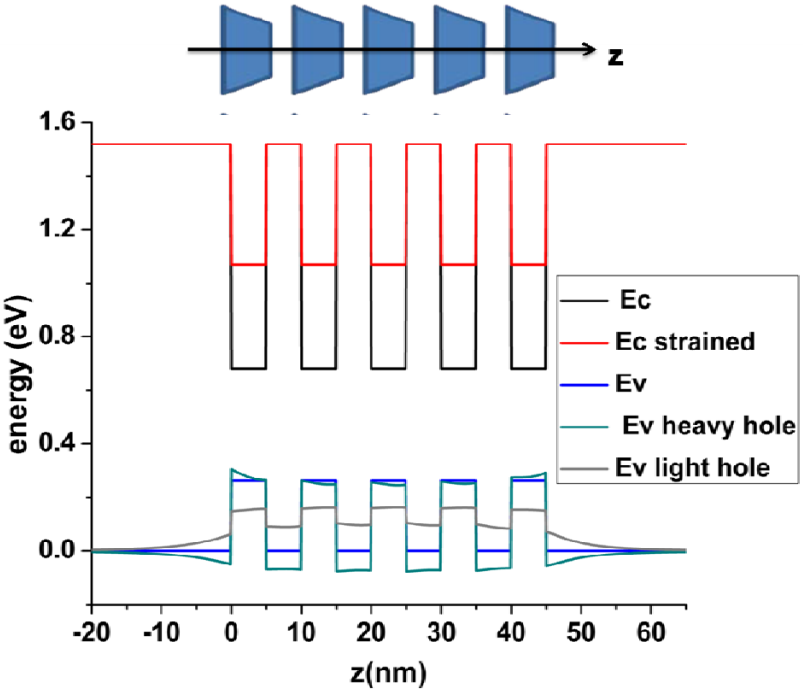

Fig. 3.12 Energy band edge alignment of a vertical QD array of 5 QDs with 5 nm spacing.

In the QD array, inside the QD, the heavy hole band edge (shown in Fig.3.13) shifts downward in energy with decrease of spacer layer thickness from infinite to 3 nm. The barrier material also shows the downshift of the heavy hole band edge. But the downward shift of heavy hole band edge is more rapid in QD than in barrier material with the decrease of barrier layer thickness. These results together with the intermixing of indium and gallium due to strain fields can explain the blue shift in the PL peak energy observed when the barrier layer thickness is less than 5 nm [122]. On the other hand, the light hole band shifts upward in energy with the decrease of spacer layer thickness from infinite to 3 nm. Fig.3.14 shows that in the barrier material the light hole band shifts upward in energy more rapidly than inside the QD making the light hole confinement

potential shallower as the spacer layer thickness is decreased from infinite to 3 nm. As the spacer layer thickness decreases to 3 nm, the energy separation of heavy and light holes becomes only 0.04 eV in comparison to 0.16 eV in case of a QD in an infinite matrix .

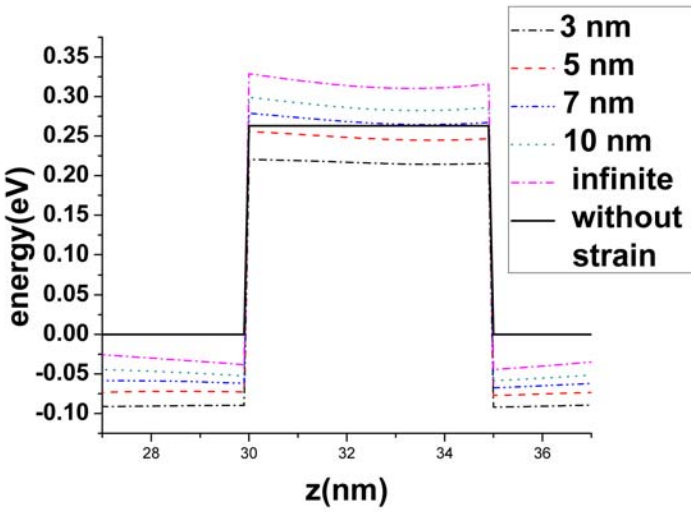

Fig.3.13 Valence band, heavy hole band edges along a line scan perpendicular and passing through the center of the base of square based (20 nm) truncated pyramid shaped QD array for different spacer layer thickness.

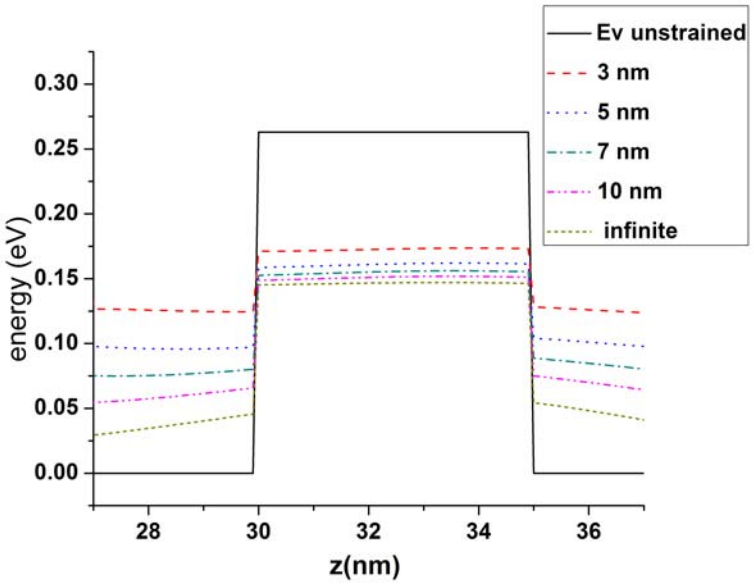

Fig.3.14 Valence band, heavy hole band edges along a line scan perpendicular and passing through the center of the base of square based (20 nm) truncated pyramid shaped QD array for different spacer layer thickness.

3.9 Conclusion

In this chapter, the formulation for the band structure calculation with the effect of strain was assessed based on the k•p method. The formulation was used to calculate the band edge alignment with the effect of strain for III-V and silicon germanium quantum dot/barrier material system. The results were presented and analyzed for their potential implication to the advanced nanostructure solar cells. The results obtained for vertical array of QD in III-V materials, especially InAs QDs on GaAs matrix, show a significant change in valence band alignment between the QD and barrier materials with the change of spacer layer thickness. The confinement potentials of heavy and light holes changes with the spacer layer thickness. This, ultimately changes the energy of confined energy states in valence band and hence the band gap E_{IV} (see Fig. 1.7) of intermediate band solar

cells. Overall, the methodology developed in this chapter is applied to search for the optimum material combinations for multiple transitions solar cells, which could be realized with QD nanostructures.

Chapter 4

MATERIAL SEARCH FOR QUANTUM DOT INTERMEDIATE BAND SOLAR CELLS

4.1 Introduction

A multiple transitions solar cell, also called intermediate band solar cell (IBSC), can overcome the Shockley-Queisser limit by absorbing low band-gap photons while preserving the voltage corresponding to high band gap material. This solar cell, as briefly explained in chapter 1, absorbs the below band gap photons via the intermediate electronic states (or bands). Single or multiple such electronic states (or bands) that could be introduced in an otherwise forbidden energy gap of a semiconductor material extend the absorption of solar radiation to longer wavelength by multiple electronic transitions.

Heterostructures including self-assembled quantum dots (QDs) have been suggested as model systems for the realization of intermediate band solar cells[34,123].The experimental prototypes for quantum dot intermediate band solar cells (QD IBSCs) include heterostructures consisting of InAs, GaAs and their alloys[36,37] grown on GaAs substrates. In spite of numerous efforts, the prototype quantum dot solar cells show a deteriorated efficiency as compared to the control solar cell without quantum dots [38,124]. There is no experimental evidence of global efficiency enhancement in the solar cell with quantum dot nanostructures. Generally, the prototype intermediate band solar cells with self-assembled QD nanostructures show the spectral response to longer wavelengths than that of a base GaAs solar cells without QDs but the I-V characteristics shows significant loss in open circuit voltage(V_{oc}) [125, 126].

There are several possible reasons for the lower than predicted open circuit voltage (V_{oc}). The creation of defects due to accumulation of strain due to the growth of many QD layers in order to obtain significant contribution to the photocurrent from sub-band-gap photons degrades minority carrier lifetime and reduces open circuit voltage. To minimize the accumulation of strain, thin strain compensating layers have been included in the prototype. The improvement in V_{oc} due to strain balanced structures compared to devices without strain compensation [127,128,129] can be attributed to much lower density of dislocations (thus low non-radiative recombination). Nevertheless, all of the strain compensated devices still have lower V_{oc} than the GaAs control cell.

In addition to material quality issues, InAs/GaAs systems have non-optimum band structures. For example, the InAs/GaAs material system has significant valence band offset (0.23 eV). Another reason for the lower V_{oc} is the significant valence band offset between the dot and barrier materials in those material systems [109, 129]. It is well known that the valence band (heavy hole) effective mass of a semiconductor is higher than the effective mass of an electron in conduction band. From simple quantum mechanical calculations, it can be observed that the higher effective mass results into closely spaced confined states [130]. For experimentally observed shape and size of QD, the energetic spacing of the heavy hole confined states is so close that the holes from the valence band continuum of GaAs, simply, thermalize to the lowest confined energy state in InAs QD valence band via optical phonon interaction. This mechanism causes shift of quasi Fermi level corresponding to the GaAs valence band to the lowest

confined state in the valence band, which ultimately causes the loss in V_{oc}. In addition to this, the key principle of IBSCs is that there should be a simultaneous existence of multiple quasi Fermi levels in an IB material. Although, some studies have shown the simultaneous absorption of sub-band gap photons [131,132] the proof of simultaneous existence of multiple quasi Fermi levels in an IB material is still an unresolved issue.

Overall, a key barrier in intermediate band solar cells is the identification of a QD material system which can be readily fabricated to facilitate characterization and displays a close to optimum band structure. In this work, QD/barrier material combinations with band gaps (E_{IV}, E_{IC}, E_G) capable of photovoltaic efficiency greater than 40% at moderate solar concentration (500x) are determined. These calculations include realistic effects associated with the growth of self-assembled quantum dots. Specifically, the effect of elastic strain due to lattice mismatch between the QD and barrier/substrate materials is calculated and the effect of strain on the band structure is taken into account to search the material combinations. A brief overview of the methodologies and the constraints used in the QD/barrier material search is given in the next sections.

When a material with significant lattice mismatch (eg GaAs/InAs, 7.2%) is grown epitaxially on a substrate, initial growth occurs layer by layer but the accumulation of strain energy causes three dimensional growth to proceed in order to minimize the energy increase due to strain. This sees the formation of islands of grown material distributed randomly over the growth surface that act as

quantum dots [133]. The shape and size of these self-assembled quantum dots depend on the growth conditions and material parameters with reports of lens, multifaceted dome, pyramid or truncated pyramid shaped dots [47,78,134]. For this work, the shape of the quantum dot is considered to be that of a square based truncated pyramid as schematically shown in Fig.4.1(as described and analyzed in Chapters 2 and 3). The pyramid has a base width (a) of 20 nm and height (hf) 5 nm. The QDs are considered to be grown on a (001) substrate. The initial misfit strain is defined as:

$$\varepsilon_0 = \frac{(a_s - a_l)}{a_l} \tag{4.1}$$

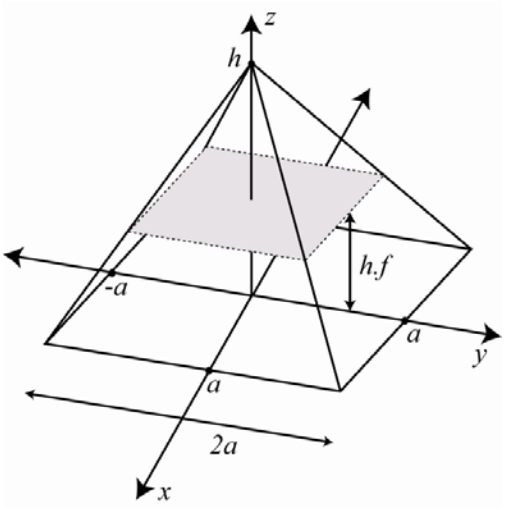

Fig. 4.1 Schematic diagram of the truncated pyramid shaped quantum dot assumed in the band structure calculations.

where, a_s and a_l are the lattice constants of substrate or barrier and quantum dot materials, respectively and the misfit strain is, in this case, taken to be negative for material under compression. For simplicity, the misfit strain is considered to be constant throughout the QD structure. An analytical method based on the

continuum theory of elasticity, as outlined in chapter 2, is used to calculate the strain distribution in and around the quantum dot. The hydrostatic and biaxial strains are calculated and coupled to the k•p method via deformation potentials to calculate the band structure.

4.2. Calculation of the band structure of a quantum dot

For the band structure calculation, a multi-band envelope function method (also called k•p method) is used. As outlined in chapter 3, this method gives the band structure near the band edge very accurately for bulk and heterostructures. In this method, as outlined in chapter 3, the strain is incorporated in the Hamiltonian via deformation potentials.

The bulk and alloy band gaps at room temperature are obtained by using Varshni parameters (α and β) for the materials from their corresponding values at zero Kelvin. The band gaps of the alloy compositions are calculated by using the corresponding bowing parameters for the materials. For all the III-V semiconductors and their alloys considered in this work, the parameters used for the calculation of strain and the band gaps as well as the dependence of band gaps on temperature and alloy composition are taken from references [135] and [81].

By including all of these features (the modified band gap and band offsets), an optimum combination of III-V semiconductor binaries/ternaries can be found. The calculations are performed allowing a large number of combinations to be investigated. Some constraints to the materials are included to make the calculations more feasible and realistic from experimental point of view.

4.3 Constraints for material search for QD intermediate band solar cells

As stated in section 4.1, the main factors limiting the materials systems search are the requirement of negligible valence band offset and the optimum band gaps. Both of these parameters are highly dependent on the elastic strain in the structure due to lattice mismatch between the substrate (barrier) and the dot materials. Two cases are considered to broaden the criteria of material search.

1. Materials grown on lattice matched metamorphic buffer layer.
2. Materials grown on lattice mismatched pseudomorphic buffer layer.

Both of these cases are viable from experimental point of view with the 'lattice matched metamorphic buffer layer' case giving greater flexibility in the choice of barrier material. This case can be experimentally realized by growth schemes involving compositionally graded buffer layers for obtaining the required composition of barrier material and localizing defects and misfits away from the device layers [136] as schematically shown in Fig.4.2.

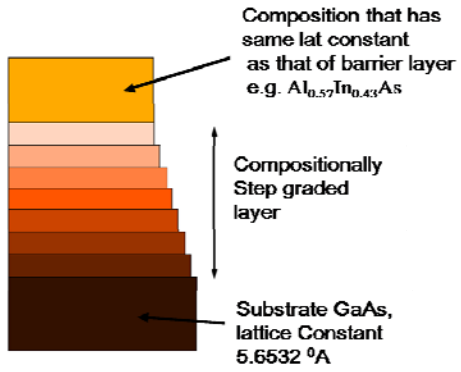

Fig. 4.2 Schematic diagram of the compositionally step graded buffer layer.

The ‘materials grown on pseudomorphic buffer layer’ case (mentioned as ‘fully strained’ hereafter), as schematically shown in Fig. 4.3, is possible when the barrier thickness is kept less than its critical thickness. In both cases (fully strained and relaxed), the management of strain will become critical in order to grow a large number of QD layers (necessary in order to increase absorption), but with mismatch between all of the layers the fully strained case would be anticipated to be the more challenging of the two scenarios.

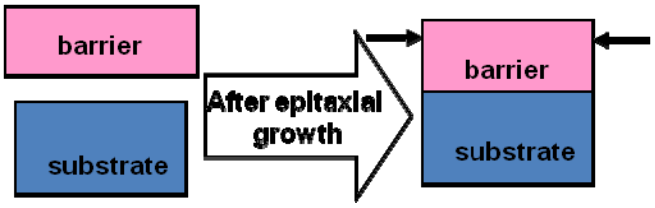

Fig. 4.3 Fully strained case, pseudomorphic structure compressive/tensile strain.

There are also practical considerations such as the choice of III-V binary substrates. For this work several commercially available substrates are considered including GaAs, InP and InAs with preference given to GaAs and InP. Restricting ourselves to these three substrates, the three main criteria considered for material identification for high efficiency QD solar cells are: negligible valence band offset; constraints on lattice mismatch; and realization of optimum band gaps.

4.3.1 Negligible Valence band offset (VBO) between barrier and QD

As briefly mentioned in section 4.1, due to the higher effective mass of holes in valence band, even a small confinement potential gives rise to many

bound states very close (in the order of kT) to each other [109,137]. Holes may thermalize through these states to the ground state in QD. Because of the lower energy level of the hole states, carriers from the barrier thermalize to the lowest energy in the QD. Thus, the quasi Fermi level of the valence band is determined by the hole ground state in QD rather than valence band continuum of the barrier material. This ultimately reduces the open circuit voltage (V_{oc}).as schematically shown in Fig. 4.4. Also, the lifetime of the carriers is reduced as they can easily recombine between the conduction and valence band bound states rather than between the CB bound states and continuum states in VB or between continuum states (this can be roughly estimated from the Fermi-Golden rule for the transition rate due to interaction with photons)[138]. In order to minimize these effects the maximum for the VBO was set to be ~3kT where k is the Boltzmann constant and T is room temperature.

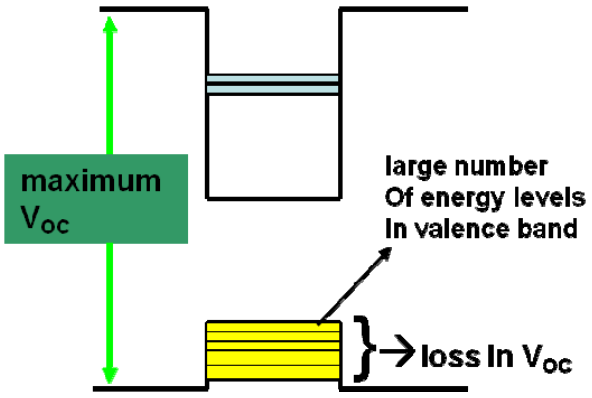

Fig. 4.4 Schematic diagram showing the voltage loss due to VBO.

Several theoretical approaches to calculate the band offsets of semiconductor heterostructures [139,140,141] predict different values of VBO. The experimental results together with the theoretical calculations provide

reasonably accurate vales of VBO for III-V heterostructures. Here, to calculate the VBO of strained material systems the bulk values given in reference [81], which presents the VBO of each III-V materials with respect to InSb valence band, are used.

4.3.2 Lattice mismatch

The lattice mismatch between the barrier and QD materials is taken to be in a reasonable range [142] for the formation of QDs by Stranski-Krastanov growth mode when using the epitaxial growth methods such as metal-organic chemical vapor deposition (MOCVD) or molecular beam epitaxy (MBE). Previous work has shown that, in Stranski-Krastanov growth, the onset of 3D growth at the top of 2D wetting layer depends on the elastic strain between the substrate and grown materials [143 ,144]. For very small lattice mismatch (less than 2%) there is no observation of formation of QDs for normal growth conditions [143]. At low temperature, due to limited surface diffusion of ad-atoms, QD formation might be suppressed [142]. Taking these facts into account, for the materials grown on metamorphic buffer layer, the lattice constant of the dot material is specified to be at least 2% greater than that of barrier. For the fully strained case, the lattice constant of the dot material was taken to be at least 2% greater than that of the substrate.

4.3.3 Band gaps

The eight band k•p method including the effect of strain is used to calculate the band diagram along a Γ-point ($k = 0$) and the band alignment of the

barrier and dot materials are obtained. With this, the modified band gaps, the conduction and valence band offsets are determined.

Due to relatively higher absorption coefficient than indirect band gap materials, devices with direct band gap can absorb significant amount of light at comparatively lower thickness. The thickness of the IB-absorbing medium is limited by the number of QD layers that can be achieved while retaining sufficiently low defect density for large carrier collection. Given the low absorption of a single QD layer, only direct band gap materials are considered in the material search in order to address the issue of absorption and the thickness of the absorbing medium in the nanostructured materials [145]. The barrier band gap is taken to be greater than 1.2 eV and conduction band offset (CBO) greater than 0.4 eV. These values are essential for the efficiency to be greater than 45% as indicated by previous detailed balance calculations [146]. All of the bands gaps used to calculate and presented in this work are at room temperature with the effects of strain included.

4.4 Material combinations for QD intermediate band solar cells

Material searches were performed among III-V binaries and their alloys with direct band gaps applying the criteria described in the previous section. This corresponds to the absolute value of the VBO between the barrier and the dot materials at room temperature being lower than ~ 0.06 eV. The valence band edge energies are no longer degenerate when the strain is included and so a separate VBO was found for light holes and heavy holes. As discussed earlier, a higher

effective mass means a greater number of confined energies and hence greater deleterious thermalization of carriers. In addition to this, due to compressive strain in QD, for the shape considered in this work the heavy hole band edge is always lower in energy than the light hole band edge. For these reasons, the VBO for heavy holes was taken as the selection criterion in preference to that for light holes.

Table 4.1 Barrier/QD materials combinations for material grown on lattice matched metamorphic buffer layer.

Barrier	X	Dot	y
$Al_{1-x}In_xAs$	[0.43→0.54]	$InP_{1-y}Sb_y$	[0.13→0.21]

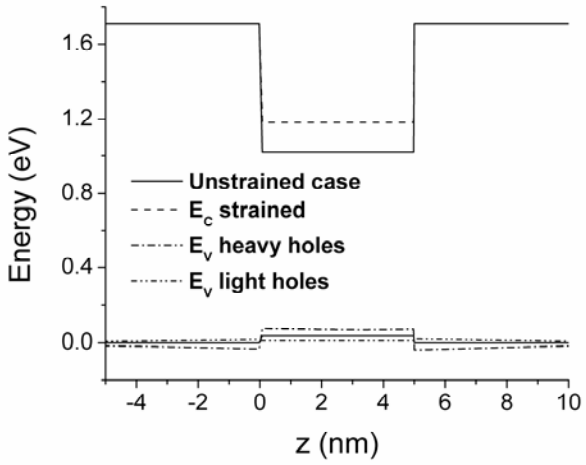

Fig. 4.5 Energy band edge diagram at the Γ point along the z axis through QD midpoint (x=0, y=0) for $InP_{0.87}Sb_{0.13}$ quantum dots with $Al_{0.57}In_{0.43}As$ barriers (grown on lattice matched metamorphic buffer layer).

Table 4.1 gives the material combination (barrier/dot) that best satisfies the target parameters for the case of material grown on a metamorphic buffer

layer. The $InP_{1-y}Sb_y$ dots with $Al_{1-x}In_xAs$ barrier has negligible valence band offset with the conduction band offset being approximately 0.5 eV. The theoretical efficiency of this material combination with these band gaps is 58% under 1000 solar concentrations for the AM 1.5D spectrum, very close to the maximum available (61%) for this spectrum at this concentration [15]. Shown in Fig.4.5 is the band edge energy at the Γ point along the z (growth) axis through the center of the quantum dot for $InP_{0.87}Sb_{0.13}$ dots with $Al_{0.57}In_{0.43}As$ barriers. Also shown are the band edges without the effect of strain for comparison. The dot/barrier lattice mismatch in this material combination is ~2% and the band gaps of the barrier and dot materials are 1.707 eV and 1.183 eV respectively making it a close match to the low confinement energy design identified in [146].

Tables 4.2 and 4.3 present materials combinations for the case of fully strained system on GaAs and InP substrates respectively. These material combinations, with negligible VBO, have comparatively larger lattice mismatches than for the material grown on lattice matched metamorphic buffer layer case with the mismatch between substrate and dot generally being around 3% or higher for the material combinations on GaAs substrate.

Table 4.2 Material combinations on GaAs substrate for the materials grown on lattice mismatched pseudomorphic buffer layer.

Barrier	X	Dot	y
$Al_{1-x}Ga_xSb$	[0.79→0.88]	$InAs_{1-y}Sb_y$	[0.58→0.73]
$Al_{1-x}In_xAs$	[0.52→0.37]	$InAs_{1-y}P_y$	[0.54→1]
$Al_{1-x}In_xAs$	[0.37→0.41]	$InP_{1-y}Sb_y$	[0.01→0.06]

Table 4.3 Material combinations on InP substrate for the materials grown on lattice mismatched psuedmorphic buffer layer.

Barrier	x	Dot	y
$Al_{1-x}Ga_xSb$	[0.74→0.80]	$InAs_{1-y}Sb_y$	[0.56→0.70]
$Al_{1-x}In_xAs$	[0.74→0.79]	$InP_{1-y}Sb_y$	[0.70→0.79]
$Al_{1-x}In_xAs$	0.59	$InAs_{1-y}P_y$	0.37

For instance, the $Al_{0.50}In_{0.50}As/InAs_{0.41}P_{0.59}$ barrier/dot combination has a 3.6% substrate/barrier lattice mismatch and a 5% substrate/dot lattice mismatch. This increase in compressive strain due to lattice mismatch between the barrier and the dot materials results in smaller values of the CBO and so achieving the optimum band gaps is more difficult than for the material grown on lattice matched metamorphic buffer layer case. As a consequence the limiting efficiencies for these designs were considerably lower than for the material grown on lattice matched metamorphic buffer layer. On the other hand, the material combinations on InP substrate; particularly AlGaSb/InAsSb barrier dot combination; have 4% substrate/barrier lattice mismatch and a 7% substrate/dot lattice mismatch. Despite the very low bulk band gap of InAsSb, significant compressive strain

(~7%) increases its band gap by almost 0.6eV making this material combination a realistic candidate material for the growth of QDIBSCs. A few specific materials combinations for fully strained system grown on a GaAs are listed in Table 4.4 along with their corresponding limiting efficiencies. The efficiencies listed are for 1000x concentration under AM1.5D spectrum calculated by detailed balance. In this case the theoretical efficiencies of most of the materials combinations are about 50% with the $Al_{0.50}In_{0.50}As/InAs_{0.41}P_{0.59}$ barrier/dot combination giving the highest value of 53%.

Table 4.4 Barrier/Dot materials combinations on a GaAs substrate (materials grown on lattice mismatched pseudomorphic buffer layer) with corresponding efficiencies.

Barrier	Dot	E_G Bar (eV)	E_G Dot (eV)	Eff. (%)
$Al_{0.63}In_{0.37}As$	InP	2.07	1.65	48
$Al_{0.62}In_{0.38}As$	$InAs_{0.11}P_{0.89}$	2.05	1.55	49
$Al_{0.6}In_{0.4}As$	$InAs_{0.15}P_{0.85}$	2.0	1.52	48
$Al_{0.50}In_{0.50}As$	$InAs_{0.41}P_{0.59}$	1.77	1.30	53

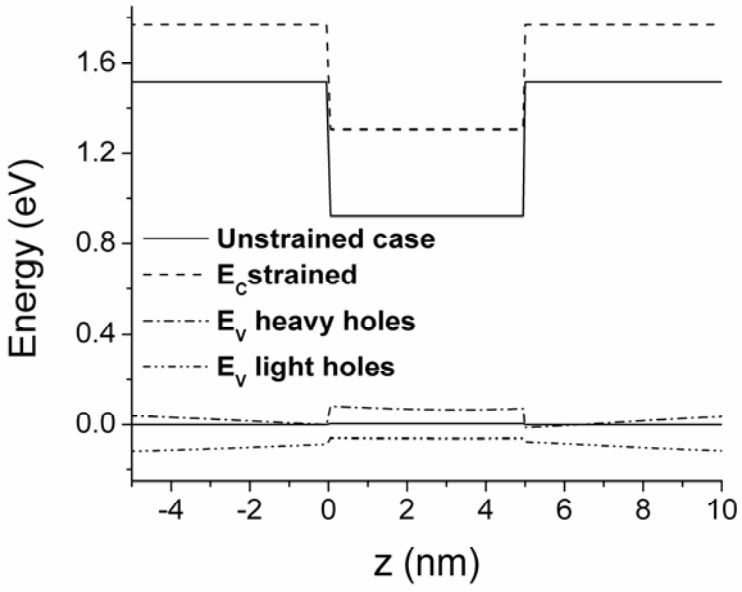

Fig. 4.6 Energy band edge diagram at the Γ point along the z axis through QD midpoint (x=0, y=0) for $InAs_{0.41}P_{0.59}$ quantum dots with $Al_{0.50}In_{0.50}As$ barriers on a GaAs substrate (grown on lattice mismatched pseudomorphic buffer layer).

The band edge energy at the Γ-point along the z-axis through the center of the base of the quantum dot for $InAs_{0.41}P_{0.59}$ QD with $Al_{0.50}In_{0.50}As$ barriers on a GaAs substrate is shown in Fig.4.6. As can be seen, the band gaps of the barrier and the dot material are 1.77 eV and 1.30 eV respectively making it the closest match to the optimum combination of 1.77eV and 1.20 eV respectively. What is also evident is the effect of the high levels of compressive strain in this materials system due to lattice mismatch. The compressive strain raises the conduction band edge of the dot material resulting in the decrease of the CBO pushing the value further away from its optimum.

4.5 Issues related to growth of the optimum material combinations

With one exception of InP QD in $Al_{0.63}In_{0.37}As$ matrix grown on [001] GaAs substrate (table 4.4), all of the barrier/dot material combinations identified in this work as being close to optimum, require ternary compounds with two group V elements for the QD material. From a growth perspective, the growth of compounds containing more than one group V elements requires precise control of the flux ratio and growth temperature in order to achieve the desired mole fractions reproducibly. This is due to the different temperature dependencies of the sticking coefficients of group V elements, therefore adding to the complexity of the growth. As well as being dependent on flux ratio and temperature, the composition will depend on the strain in any grown layer making the growth of multiple group V element ternary quantum dots, where the strain varies throughout the volume of the structure, particularly challenging. However, well optimized growths of InAsP [147,148] and InAsSb [149] dots have been reported. In contrast, InPSb QDs grown on AlInAs have not been reported. This could be due to the reported miscibility gap of InPSb [150] which is predicted by theory to cover almost the whole range of compositions for commonly used growth temperatures. This miscibility gap is ascribed to the very different covalent bonding radii of phosphorous and antimony. However, the experimental demonstration of high quality InPSb quantum wells on InAs has been reported in direct contradiction of theory [151].

With few exceptions, the barrier material for optimum material combinations is AlInAs, which is not lattice matched to GaAs and InP substrates.

Experimentally, there are reports of lateral composition modulation and the surface morphology of AlInAs epitaxially grown on lattice matched InP substrates [152,153,154]. These reports indicate that the control of shape, size and uniformity of quantum dots on AlInAs buffer may be challenging and would require extensive experimental optimization. Finally, most of the barrier materials identified contain significant fractions of aluminum, which would make them prone to oxidation in atmospheric conditions. This issue can be effectively solved by capping with appropriate binary compound and there would appear to be no other impediments to their growth.

4.6 Conclusion

Materials combinations for QD intermediate band solar cell with negligible valence band offset are presented with the effects of the strain due to lattice mismatch included in the band structure. The two cases of the barrier being fully relaxed and fully strained are examined. The limiting efficiencies of the identified material combinations are calculated using detailed balance for the AM1.5D solar spectrum at 1000x concentration and are presented. Two material combinations were obtained having limiting efficiencies greater than 50%. One of the material combinations, $InP_{0.87}Sb_{0.13}$ QDs with $Al_{0.57}In_{0.43}As$ barriers, optimum for the barrier fully relaxed case, has a limiting efficiency up to 58% under 1000x concentration, very close to the maximum efficiency (61%) at this concentration. The other barrier/QD material combination identified, $Al_{0.50}In_{0.50}As$/ $InAs_{0.41}P_{0.59}$, with the barriers fully strained, has a limiting efficiency of 53% under 1000x

concentrations. Finally, it was observed that the $Al_{0.50}In_{0.50}As/InAs_{0.41}P_{0.59}$ system may be preferred to the $Al_{0.57}In_{0.43}As/InP_{0.87}Sb_{0.13}$ system due to a perceived miscibility gap for InPSb in the temperature range normally used in growth.

Chapter 5

CONCLUSION

Realization of ultra-high efficiency photovoltaic devices based on advanced concepts relies on materials which have the appropriate material parameters as determined by detailed balance efficiency calculations. From detailed balance calculations, the material band gap is the most fundamental parameter that determines the efficiency of a solar cell. Advanced concept solar cells rely on the modification of the absorption/recombination process in conventional solar cell to achieve efficiency increases. While it is possible to design new bulk materials which display the desired properties, nanostructures provide an immediate path towards the realization of advanced concept solar cells. However, despite the present necessity of using nanostructures to investigate most of the advanced concept approaches, a critical need has been an approach which allows design of nanostructures that can be practically implemented and display band structures close to those required by detailed balance calculations. The overarching goal of this work is to address this need, allowing the identification of materials and nanostructure configurations for advanced concept solar cells. This is by developing material models which include critical realistic effects, such as strain, and which can be combined with detailed balance calculations to predict and identify optimum material candidates for ultra-high efficiency approach.

The starting point for the development of material model for advanced concept ultra-high efficiency solar cells using nanostructures as absorbing

medium is to calculate the band structure of these nanometer scale structures taking into account some of the realistic effects associated with growth of these materials. This work addresses the fundamental issues by calculating the band structure of the materials (specifically, self-assembled quantum dots) taking the effect of elastic strain due to lattice mismatch and the realistic shape of quantum dots into account. The results of band structure calculations are applied to search optimum material combinations for multiple transitions solar cells.

In multiple transitions solar cells using nanostructures (also called quantum dot intermediate band solar cells); the current research revolves around InAs/GaAs-based material system, mainly due to well established growth methodology. This particular material neither has optimum band gap nor is ideal for device application due to its significant valence band offset. This work addresses the gap between the concept and the material model for multiple transition solar cells by searching the material combinations among existing materials (III-V and their alloys) with realistic effects included in band structures. Out of the optimum material combinations obtained, some combinations have efficiencies of almost 95% of the detailed balance efficiency [109,146]. However, some of the material combinations also have issues related to growth as they are tertiary materials with the combination of group III and group V materials with large difference on atomic sizes. This might limit miscibility of these materials to produce an alloy with uniform composition for normal growth conditions. These practical issues highlight the importance of the developed approach which allows

a robust search among material systems and a way to include realistic material effects in detailed balance calculations.

Although the results on the band structure calculation are presented for specific material systems, the methodology developed here can be applied to any nanostructured materials and their alloys that are feasible for advanced concept or high efficiency tandem solar cells. For example a multijunction technology with 4 and 5 junctions requires new materials, which may be implemented using nanostructures of existing materials or the existing materials strained due to lattice mismatch to achieve the proper band gaps. Also, the requirement of proper material for extraction of hot carriers in hot carrier solar cells can be fulfilled using confined states in nanostructures as resonant states. The methodology developed here could not only be applied to identify the materials for these selective energy contacts in hot carrier solar cells but also to identify the proper materials that are optimum as absorbers in these solar cells.

Overall, the identification of optimum materials for intermediate band nanostructured solar cells overcomes one of the fundamental barriers in such approaches, namely the experimental implementation of a structure which is theoretically predicted to display multiple quasi-Fermi levels. Further, the tools developed can be further applied to other ultra-high efficiency approaches, including conventional tandems using nanostructured layers and multiple exciton solar cells.

REFERENCES

[1] "International Energy Outlook 2010," US Eneregy Information Administration, Department of Energy, published July 2010.

[2] "Annual Energy Review 2009," US Energy Information Administration, Department of Energy, published August 2010.

[3] S. P. Bremner, R. Corkish, and C. B. Honsberg, "Detailed balance efficiency limits with quasi-Fermi level variations," *IEEE Transactions on Electron Devices*, vol. 46, no. 10, pp. 1932-1939, 1999.

[4] S. P. Bremner, M.Y. Levy, C. B. Honsberg, "Analysis of Tandem Solar Cell Efficiencies Under AM1.5G Spectrum Using a Rapid Flux Calculation Method," *Progress in Photovoltaics: Research and Applications*, vol.16, pp.225-233, 2008.

[5] A. Luque, A. Marti, "Increasing the efficiency of ideal solar cells by photon induced transitions at intermediate levels," *Physical Review Letters*, vol. 78, p.5014, 1997.

[6] A. De Vos and B. Desoete, "On the ideal performance of solar cells with larger-than-unity quantum efficiency," *Solar Energy Materials and Solar Cells*, vol. 51, pp. 413-424, 1998.

[7] R.T. Ross, "Efficiency of hot-carrier solar energy converters," *Journal of Applied Physics*, vol. 53, p. 3813, 1982.

[8] K.M Yu, W. Walukiewicz, J. Wu, W. Shan, J.W. Beeman, M.A Scarpulla, O.D. Dubon, and P. Becla, " Diluted II-VI oxide semiconductors with multiple band gaps," *Physical Review Letters*, vol. 91, p. 246403, 2003.

[9] C. Tablero, "Analysis of the electronic properties of intermediate band materials as a function of impurity concentration," *Physical Review B*, vol. 72, no. 3, p. 035213, 2005.

[10] Martin A. Green, "Third generation photovoltaics: Ultra-high conversion efficiency at low cost," *Progress in photovoltaics:Research and Applications*, vol. 9, pp:123-135, 2001.

[11] M. A. Green, J. Zhao, A. Wang, and S. R. Wenham, "Progress and outlook for high-efficiency crystalline silicon solar cells," *Solar Energy Materials and Solar Cells*, vol. 65, no. 1-4, pp. 9-16, 2001.

[12] T. Tiedje, E. Yablonovitch, G.D. Cody and B.G Brooks, "Limiting efficiency of silicon solar cells," *IEEE transactions on electron devices*, Vol. ED-31, No.5 pp.711-716, 1984.

[13] C.B. Honsberg, A.M. Barnett, and D. Kirkpatrick, "Nanostructured solar cells for high efficiency photovoltaics," *Conference Record of the 2006 IEEE 4th World Conference on,* vol. 2, pp.2565-2568, 2006.

[14] W. Shockley and H. J. Queisser, "Detailed Balance Limit of Efficiency of p-n Junction Solar Cells," *Journal of Applied Physics*, vol. 32, no. 3, p. 510, 1961.

[15] S. P. Bremner, M. Y. Levy, C. B. Honsberg, "Rapid detailed balance calculations for multiple energy gap solar cesll," *Conference record at 22nd European Photovoltaic solar energy conference*, Milan, Italy, 3-7 September, 2007.

[16] P. Chiu, S Wojtczuk, C. Harris, D. Pulver, and M. Timmons, "42.3% efficient InGaP/GaAs/InGaAs concentrators using bifacial epigrowth," *Proc.37th IEEE Photovoltaic specialist conference*, Seattle, WA, June 19-24, 2011.

[17] "Solar Junction tips 43.5% efficient CPV cell, preps 250MW capacity ramp", *Photovoltaics World, Photovoltaics-CPV*, Issue 2, March 2011

[18] R. P. Raffaelle, S .Sinharoy, J .Anderson, D.M. Wilt, S. Bailey, "Multi-junction solar cell spectral tuning with quantum dots," *In: Proc 4th world conference on photovoltaic energy conversion*. p. 162, 2006.

[19] K. W. J. Barnham and G. Duggan, "A new approach to high-efficiency multi-band-gap solar cells," *Journal of Applied Physics*, vol. 67, no. 7, p. 3490, 1990.

[20] D. B. Bushnell, N. J. Ekins-Daukes, K.W. Barnham, J. P. Connolly, J. S. Roberts, G. Hill, R. Airey, M. Mazzer, "Short-circuit current enhancement in Bragg stack multi-quantum-well solar cells for multi-junction space cell applications," *Solar Energy Materials and Solar Cells*, vol. 75, no. 1-2, pp. 299-305 2003.

[21] P. T. Landsberg, H. Nussbaumer, and G. Willeke, "Band-band impact ionization and solar cell efficiency," *Journal of Applied Physics*, vol. 74, no. 2, p. 1451, 1993.

[22] J.H. Werner, S. Kolodinski, and H.J. Queisser, "Novel optimization principles and efficiency limits for semiconductor solar cells," *Physical Review Letters*, vol. 72, p. 3851, 1994.

[23] O. Christensen, "Quantum efficiency of the internal photoelectric effect in silicon and germanium," *Journal of Applied Physics*, vol. 47, p. 689, 1976.

[24] A. J. Nozik, "Multiple exciton generation in semiconductor quantum dots," *Chemical Physics Letters*, vol. 457, no. 1-3, pp. 3-11, 2008.

[25] G.J. Conibeer,C.W. Jiang, D. Koning, S. Shrestha, T. Walsh, M.A. Green, "Selective energy contacts for hot carrier solar cells," *Thin Solid Films* vol.516, no. 20, pp. 6968-6973, 2008.

[26] A.J. Nozik, "Spectroscopy and hot electron relaxationdynamics in semiconductor quantum wells and quantum dots," *Annual Review of Physical Chemistry*, vol. 52, pp. 193-231, 2001.

[27] D. König, K. Casalenuovo, Y. Takeda, G. Conibeer, J.F. Guillemoles, R. Patterson, L.M. Huang, and M.A. Green, "Hot carrier solar cells: Principles, materials and design," *Physica E: Low-dimensional Systems and Nanostructures*, vol. 42, pp. 2862-2866, 2010.

[28] M. wolf, "Limitations and possibilities for improvement of photovoltaic solar energy converters. Part I: considerations for Earth's surface operation," *in Proceedings of the institute of Radio Engineers*, vol. 48, no. 7, pp. 1246-63.

[29] W. Walukiewicz, W. Shan, K.M Yu, and J.W Ager III, "interaction of localized electronic states with the conduction band: band anticrossing in II-VI semiconductor ternaries," *Physical Review Letters*, vol. 85, p. 1552, 2000.

[30] K.M Yu, W. Walukiewicz, J.W. Ager, D.Bour, R. Farshchi, OlD. Dubon, X.X.LI, I.D. Sharp, and E.E. Haller, "Multiband GaNAsP quarternary alloys," *Appl. Phys. Lett*, vol. 88, p, 092110 ,2006.

[31] C. Tablero, "Electronic and magnetic properties of ZnS doped with Cr," Phys Rev. B, vol. 74, p. 195203, 2006.

[32] N. J. Ekins-Daukes and T. W. Schmidt, "A molecular approach to the intermediate band solar cell: The symmetric case," *Applied Physics Letters*, vol. 93, no. 6, p. 063507, 2000.

[33] A. Marti, L.Cuadra, and A. Luque, *proc. 28th IEEE Photovoltaic specialists conference*, Piscataway, NJ, p.940, 2000.

[34] A. Marti, L.Cuadra, A. Luque, "Partial filling of a quantum dot intermediate band for solar cells," *IEEE Transactions on Electron Devices*, vol 48, pp. 2394-2399, 2001.

[35] S. Tomic, "Intermediate-band solar cells: Influence of band formation on dynamical processes in InAs/GaAs quantum dot arrays," *Physical Review B*, vol. 82, p. 195321, 2010.

[36] R Oshima, H.Komiyama, T.Hashimoto, H. shigekawa, Y. Okada, "Fabrication of multi-layer self assembled InAs quantum dots for high-efficiency solar cells," *Conference record of the 2006 4th world conference on photovoltaic Energy conversion* , Waikoloa, Hawaii, May 7-12, 2006.

[37] R.B. Laghumavarapu, M. El-Emawy, N. Nuntawong, A. Moscho, L.F. Lester, and D.L. Huffaker, "Improved device performance of InAs/GaAs quantum dot solar cells with GaP strain compensation layers," *Applied Physics Letters*, vol. 91, p. 243115, 2007.

[38] A. Martí, N. Lopez,E. Antolin, E. Canovas, A. Luque, C. Stanley, C. Farmer, and Pl Diaz, " Emitter degradation in quantum dot intermediate band solar cells," *Applied Physics letters*, vol. 90, no.23, pp. 233510-1, 2007.

[39] A. G. Norman, M. C. Hanna, P. Dippo, D. H. Levi, R. C. Reedy, J. S. Ward, and M. M. Al-Jassim, "InGaAs/GaAs QD superlattices: MOVPE growth, structural and optical characterization, and application in intermediate-band solar cells," *Proceedings of 31st IEEE photovoltaic specialists conference and exhibition*, pp. 43-48, 2005.

[40] S. Tomić, T.S. Jones and N.M. Harrison, "Absorption characteristics of a quantum dot array induced intermediate band: implications for solar cell design," *Applied physics letters* vol 93, p.263105, 2008.

[41] A. Marti, L.Cuadra, and A. Luque, *proc. 28th IEEE Photovoltaic specialists conference*,Piscataway, NJ, p.940, 2000.

[42] S.W. Osborne, P. Blood, P.M. Smowton, Y.C. Xin, A. Stintz, D. Huffaker, and L.F. Lester, "Optical absorption cross section of quantum dots," *Journal of Physics: Condensed Matter*, vol. 16, pp. S3749-S3756, 2004.

[43] A.D. Andreev, J.R. Downes, D.A. Faux, and E.P. O'Reilly, "Strain distributions in quantum dots of arbitrary shape," *Journal of Applied Physics*, vol. 86, p. 297, 1999.

[44] T.O. Cheche and Y.-C. Chang, "Analytical approach for strain and piezoelectric potential in conical self-assembled quantum dots," *Journal of Applied Physics*, vol. 104, p. 083524, 2008.

[45] J. H. Davies,"Elastic and piezoelectric fields around a buried quantum dot: A simple picture," *Journal of Applied Physics* 84, pp. 1358-1365, 1998.

[46] G.S. Pearson and D.A. Faux, "Analytical solutions for strain in pyramidal quantum dots," *Journal of Applied Physics*, vol.88, pp. 730-736, 2000.

[47] Valeria-Gabriela Stoleru, Debdas Pal, and Elias Towe, "Self-assembled (In,Ga)As/GaAs quantum-dot nanostructures: strain distribution and electronic structure," *Physica E: Low-dimensional Systems and Nanostructures,* vol.15, no. 3, pp.131-152, 2002.

[48] M. Grundmann, O. Stier, and D. Bimberg, "InAs/GaAs pyramidal quantum dots: Strain distribution, optical phonons, and electronic structure," *Physical Review B*, vol. 52, p. 11969, 1995.

[49] A.E. Romanov, G.E. Beltz, W.T. Fischer, P.M. Petroff, and J.S. Speck, "Elastic fields of quantum dots in subsurface layers," *Journal of Applied Physics*, vol. 89, p. 4523, 2001.

[50] G. Muralidharan, "Strains in InAs Quantum Dots Embedded in GaAs: A Finite Element Study," *Japanese Journal of Applied Physics*, vol. 39, p. L658-L660, 2000.

[51] Hongtao Jiang and Jasprit Singh, "Strain distribution and electronic spectra of InAs/GaAs self-assembled dots: An eight-band study," *Physical Review B* vol.56, no. 8, p.4696, 1997.

[52] S. Lee, O.L. Lazarenkova, P. von Allmen, F. Oyafuso, and G. Klimeck, "Effect of wetting layers on the strain and electronic structure of InAs self-assembled quantum dots," *Physical Review B*, vol. 70, p. 125307, 2004.

[53] Y. Kikuchi, H. Sugii, and K. Shintani, "Strain profiles in pyramidal quantum dots by means of atomistic simulation," *Journal of Applied Physics*, vol. 89, p. 1191, 2001.

[54] P. N. Keating, "Effect of Invariance Requirements on the Elastic Strain Energy of Crystals with Application to the Diamond Structure," *Physical Review* 145, no. 2, p. 637, 1966.

[55] Richard M. Martin, "Elastic Properties of ZnS Structure Semiconductors," *Physical Review B* vol.1, no. 10, p. 4005, 1970.

[56] C. Pryor, J. Kim, L.W. Wang, A.J. Williamson, and A. Zunger, "Comparison of two methods for describing the strain profiles in quantum dots," *Journal of Applied Physics* 83, no. 5, pp.2548-2554, 1998.

[57] M. A. Cusack, P. R. Briddon, and M. Jaros, "Electronic structure of InAs/GaAs self-assembled quantum dots," *Physical Review B* 54, no. 4, p. R2300, 1996.

[58] O. Stier, M. Grundmann, and D. Bimberg, "Electronic and optical properties of strained quantum dots modeled by 8-band k·p theory," *Physical Review B* 59, no. 8, p.5688, 1999.

[59] O. Brandt, K. Ploog, R. Bierwolf, and M. Hohenstein, "Breakdown of continuum elasticity theory in the limit of monatomic films," *Physical Review Letters* 68, no. 9, p.1339, 1992.

[60] J. H. Davies,"Elastic and piezoelectric fields around a buried quantum dot: A simple picture," *Journal of Applied Physics* 84, pp. 1358-1365, 1998.

[61] T.O Cheche and Yia-Chung Chang,"Analytical approach for strain and piezoelectric potential in conical self-assembled quantum dots," *Journal of Applied Physics* 104, pp. 083524-083524-11, 2008.

[62] J. D. Eshelby, "The Determination of the Elastic Field of an Ellipsoidal Inclusion, and Related Problems," *Proceedings of the Royal Society of London. Series A, Mathematical and Physical Sciences* 241, no. 1226 pp.376-396, 1957.

[63] J.R. Downes, D.A. Faux, and E.P. O'Reilly,"A simple method for calculating strain distributions in quantum dot structures," *Journal of Applied Physics* 81, p: 6700, 1997.

[64] L. D. Landau, *Theory of elasticity*, Elsevier, 1986.

[65] Stephen P. Timoshenko and James N. Goodier, *Theory of elasticity*, McGraw-Hill, 1970.

[66] P.C. Kelires and J. Tersoff, "Equilibrium alloy properties by direct simulation: Oscillatory segregation at the Si-Ge(100) 2 x 1 surface," *Physical Review Letters*, vol. 63, p. 1164, 1989.

[67] S. Ghanad-Tavakoli, M.A. Naser, D.A. Thompson, and M. Jamal Deen, "Experimental characterization and theoretical modeling of the strain effect on the evolution and interband transitions of InAs quantum dots grown on In(x)Ga(1−x)As ($0.0 \leq x \leq 0.3$) metamorphic pseudosubstrates on GaAs wafers," *Journal of Applied Physics*, vol. 106, p. 063533, 2009.

[68] V. Le Thanh, V. Yam, P. Boucaud, F. Fortuna, C. Ulysse, D. Bouchier, L. Vervoort, and J.-M. Lourtioz, "Vertically self-organized Ge/Si(001) quantum dots in multilayer structures," *Physical Review B*, vol. 60, p. 5851, 1999.

[69] V. Le Thanh, V. Yam, P. Boucaud, Y. Zheng, and D. Bouchier, "Strain-driven modification of the Ge/Si growth mode in stacked layers: a way to produce Ge islands having equal size in all layers," *Thin Solid Films*, vol. 369, pp. 43-48, 2000.

[70] R. Murray, D. Childs, S. Malik, P. Siverns, C. Roberts, J.-M. Hartmann, and P. Stavrinou, "1.3 μm Room Temperature Emission from InAs/GaAs Self-Assembled Quantum Dots," *Japanese Journal of Applied Physics*, vol. 38, pp. 528-530, 1999.

[71] Y. Nakata, K. Mukai, M. Sugawara, K. Ohtsubo, H. Ishikawa, and N. Yokoyama, "Molecular beam epitaxial growth of InAs self-assembled quantum dots with light-emission at 1.3 μm," *Journal of Crystal Growth*, vol. 208, pp. 93-99, 2000.

[72] H. Saito, K. Nishi, and S. Sugou, "Shape transition of InAs quantum dots by growth at high temperature," *Applied Physics Letters*, vol. 74, p. 1224, 1999.

[73] P.B. Joyce, T.J. Krzyzewski, G.R. Bell, B.A. Joyce, and T.S. Jones, "Composition of InAs quantum dots on GaAs (001): Direct evidence for (In,Ga)As alloying," *Physical Review B*, vol. 58, p. R15981, 1998.

[74] S. Ketharanathan, S. Sinha, J. Shumway, and J. Drucker, "Electron charging in epitaxial Ge quantum dots on Si(100)," *Journal of Applied Physics*, vol. 105, p. 044312, 2009.

[75] P. Sutter and, M.G. Lagally, "Embedding of Nanoscale 3D SiGe Islands in a Si Matrix," *Physical Review Letters*, vol. 81, p. 3471, 1998.

[76] R. Songmuang, S. Kiravittaya, and O.G. Schmidt, "Shape evolution of InAs quantum dots during overgrowth," *Journal of Crystal Growth*, vol. 249, pp. 416-421, 2003.

[77] D. M. Bruls, J. W. A. M. Vugs, P. M. Koenraad, H. W. M. Salemink, J. H. Wolter, M. Hopkinson, M. S. Skolnick, Fei Long, and S. P. A. Gill, "Determination of the shape and indium distribution of low-growth-rate InAs quantum dots by cross-sectional scanning tunneling microscopy," *Applied Physics Letters* vol.81, no. 9, p.1708, 2002.

[78] L Ouattara, A. Mikkelsen, E. Lundgren, M. Borgstrom, L. Samuelson and W. Seifert, "Stacked InAs quantum dots in InP studied by cross-sectional scanning tunnelling microscopy," *Nanotechnology* vol.15, no. 12, pp.1701-1707, 2004.

[79] L. Chu, M. Arzberger, G. Bohm, and G. Abstreiter, "Influence of growth conditions on the photoluminescence of self-assembled InAs/GaAs quantum dots," *Journal of Applied Physics* vol.85, no. 4 p.2355, 1999.

[80] A. Rastelli, M. Kummer, H.von Kanel , "Reversible shape evolution of Ge Islands on Si (001)," *Physical Review Letters* vol.87, p. 256101, 2001.

[81] I.Vurgaftman, J.R.Meyer and L.R.Ram-Mohan, "Band parameters for III-V compound semiconductors and their alloys" *Journal of Applied Physics* vol.89, p.5815, 2001.

[82] P. Yu, M.C. Beard, R.J. Ellingson, S. Ferrere, C. Curtis, J. Drexler, F. Luiszer, and A.J. Nozik, "Absorption Cross-Section and Related Optical Properties of Colloidal InAs Quantum Dots," *The Journal of Physical Chemistry B*, vol. 109, pp. 7084-7087, 2005.

[83] M. Bayer, P. Hawrylak, K. Hinzer, S. Fafard, M. Korkusinski, Z.R. Wasilewski, O. Stern, and A. Forchel, "Coupling and Entangling of Quantum States in Quantum Dot Molecules," *Science*, vol. 291, pp. 451 - 453, 2001.

[84] G.S. Solomon, J.A. Trezza, A.F. Marshall, and J. Harris, "Vertically Aligned and Electronically Coupled Growth Induced InAs Islands in GaAs," *Physical Review Letters*, vol. 76, p. 952, 1996.

[85] S. Yamauchi, K. Komori, I. Morohashi, K. Goshima, and T. Sugaya, "Electronic structures in single pair of InAs/GaAs coupled quantum dots with various interdot spacings," *Journal of Applied Physics*, vol. 99, p. 033522, 2006.

[86] S. Rouvimov, Z. Liliental-Weber, W. Swider, J. Washburn, E.R. Weber, A. Sasaki, A. Wakahara, Y. Furkawa, T. Abe, and S. Noda, "Effects of GaAs-spacer strain on vertical ordering of stacked InAs quantum dots in a GaAs matrix," *Journal of Electronic Materials*, vol. 27, pp. 427-432(1998).

[87] M.A. Migliorato, L.R. Wilson, D.J. Mowbray, M.S. Skolnick, M. Al-Khafaji, A.G. Cullis, and M. Hopkinson, "Structural and optical studies of vertically aligned InAs/GaAs self-assembled quantum dots," *Journal of Applied Physics*, vol. 90, p. 6374, 2001.

[88] K.-Y. Ban, S.P. Bremner, G. Liu, S.N. Dahal, P.C. Dippo, A.G. Norman, and C.B. Honsberg, "Use of a GaAsSb buffer layer for the formation of small, uniform, and dense InAs quantum dots," *Applied Physics Letters*, vol. 96, p. 183101, 2010.

[89] T. Kanto and K. Yamaguchi, "In-plane self-arrangement of high-density InAs quantum dots on GaAsSb/GaAs(001) by molecular beam epitaxy," *Journal of Applied Physics*, vol. 101, p. 094901, 2007.

[90] C.H. Chan, C.H. Lee, Y.S. Huang, J.S. Wang, and H.H. Lin, "Characterization of excitonic features in self-assembled InAs/GaAs quantum dot superlattice structures via surface photovoltage spectroscopy," *Journal of Applied Physics*, vol. 101, p. 103102, 2007.

[91] J.S. Wang, S.H. Yu, Y.R. Lin, H.H. Lin, C.S. Yang, T.T. Chen, Y.F. Chen, G.W. Shu, J.L. Shen, R.S. Hsiao, J.F. Chen, and J.Y. Chi, "Optical and structural properties of vertically stacked and electronically coupled quantum dots in InAs/GaAs multilayer structures," *Nanotechnology*, vol. 18, p. 015401, 2007.

[92] H. Shin, W. Lee, and Y.-H. Yoo, "Comparison of strain fields in truncated and un-truncated quantum dots in stacked InAs/GaAs nanostructures with varying stacking periods," *Journal of Physics: Condensed Matter*, vol. 15, pp. 3689-3699, 2003.

[93] J.C. Slater and G.F. Koster, "Simplified LCAO Method for the Periodic Potential Problem," *Physical Review*, vol. 94, p. 1498, 1954.

[94] J.C. Phillips and L. Kleinman, "New Method for Calculating Wave Functions in Crystals and Molecules," *Physical Review*, vol. 116, p. 287, 1959.

[95] J. Bardeen, "An improved calculation of the energies of metallic Li and Na," *J. Chem. Phys*, Vol. 6, pp.367-371, 1938.

[96] E.O Kane, "The k.p method," *Semicnductors and semimetals*, vol. 1, Academic, New York, 1996.

[97] J.M. Luttinger and W. Kohn, "Motion of electrons and holes in perturbed periodic fields," *Phys. Rev*. Vol 97, pp. 869-883, 1955.

[98] George F. Koster, *Properties of the thirty-two point groups*, M.I.T. Press, 1963.

[99] G. Dresselhaus, A. F. Kip, and C. Kittel, "Cyclotron Resonance of Electrons and Holes in Silicon and Germanium Crystals," *Physical Review* 98, no. 2 p.368, 1955.

[100] E.O. Kane "Energy band theory", in *Handbook on semiconductors*. - 1: *Basic properties of semiconductors*, edited by T. S. Moss and P. T. Landsberg, North-Holland, 1992.

[101] P. Löwdin, "A Note on the Quantum-Mechanical Perturbation Theory," *The Journal of Chemical Physics* 19, no. 11 p.1396, 1951.

[102] R. H. Parmenter, "Symmetry Properties of the Energy Bands of the Zinc Blende Structure," *Physical Review* 100, no. 2, p.573, 1955.

[103] Soline Richard, Frédéric Aniel, and Guy Fishman, "Energy-band structure of Ge, Si, and GaAs: A thirty-band kbullp method," *Physical Review B* 70, no. 23 p. 235204, 2004.

[104] O. Krebs, D. Rondi, J.L. Gentner, L. Goldstein, and P. Voisin, "Inversion Asymmetry in Heterostructures of Zinc-Blende Semiconductors: Interface and External Potential versus Bulk Effects," *Physical Review Letters*, vol. 80, p. 5770, 1998.

[105] J. M. Luttinger and W. Kohn, "Motion of Electrons and Holes in Perturbed Periodic Fields," *Physical Review* 97, no. 4, p. 869, 1955.

[106] T. B. Bahder, "Eight band k.p model of strained zinc-blende crystals," *Physical Review B*, Vol. 41, p.11992, 1990.

[107] G. L. Bir and G. E. Pikus, *Symmetry and strain-induced effects in semiconductors*, Wiley, 1974.

[108] C. Pryor, "Quantum Wires Formed from Coupled InAs/GaAs Strained Quantum Dots," *Physical Review Letters*, vol. 80, p. 3579, 1998.

[109] S.N. Dahal, S.P. Bremner, and C.B. Honsberg, "Identification of candidate material systems for quantum dot solar cells including the effect of strain," *Progress in Photovoltaics: Research and Applications*, vol.18, pp. 233-239(2010).

[110] D.J. Eaglesham and M. Cerullo, "Dislocation-free Stranski-Krastanow growth of Ge on Si (100)," *Physical Review Letters*, vol. 64, p. 1943, 1990.

[111] N. Sustersic, L. Nataraj, C. Weiland, M. Coppinger, M.V. Shaleev, A.V. Novikov, R. Opila, S.G. Cloutier, and J. Kolodzey, "Effects of boron and phosphorus doping on the photoluminescence of self-assembled germanium quantum dots," *Applied Physics Letters*, vol. 94, p. 183103, 2009.

[112] S. Ketharanathan, S. Sinha, J. Shumway, and J. Drucker, "Electron charging in epitaxial Ge quantum dots on Si(100)," *Journal of Applied Physics*, vol. 105,p. 044312, 2009.

[113] D. Grützmacher, T. Fromherz, C. Dais, J. Stangl, E. Müller, Y. Ekinci, H.H. Solak, H. Sigg, R.T. Lechner, E. Wintersberger, S. Birner, V. Holý, and G. Bauer, "Three-Dimensional Si/Ge Quantum Dot Crystals," *Nano Letters*, vol. 7, pp. 3150-3156, 2007.

[114] C. G. Van de Walle, "Band lineups and deformation potentials in the model-solid theory," *Physical Review B*, vol. 39, no. 3, p. 1871, 1989.

[115] M. El Kurdi, S. Sauvage, G. Fishman, and P. Boucaud, "Band-edge alignment of SiGe/Si quantum wells and SiGe/Si self-assembled islands," *Physical Review B*, vol. 73, no. 19, p. 195327, 2006.

[116] S.-S. Li, J.-B. Xia, Z.L. Yuan, Z.Y. Xu, W. Ge, X.R. Wang, Y. Wang, J. Wang, and L.L. Chang, "Effective-mass theory for InAs/GaAs strained coupled quantum dots," *Physical Review B*, vol. 54, p. 11575, 1996.

[117] D. Gershoni, H. Temkin, G.J. Dolan, J. Dunsmuir, S.N.G. Chu, and M.B. Panish, "Effects of two-dimensional confinement on the optical properties of InGaAs/InP quantum wire structures," *Applied Physics Letters*, vol. 53, p. 995, 1988.

[118] M. Califano and P. Harrison, "Quantum box energies as a route to the ground state levels of self-assembled InAs pyramidal dots," *Journal of Applied Physics*, vol. 88, p. 5870, 2000.

[119] M. Califano, P. Harrison, "Presentation and experimental validation of a single-band, constant-potential model for self-assembled InAs/GaAs quantum dots," *Phys. Rev. B* vol 61, p. 10959, 2000.

[120] C. Pryor, "Eight-band calculations of strained InAs/GaAs quantum dots compared with one-, four-, and six-band approximations," *Physical Review B*, vol. 57, no. 12, p. 7190, 1998.

[121] K.-Y. Ban, W.-K. Hong, S.P. Bremner, S.N. Dahal, H. McFelea, and C.B. Honsberg, "Controllability of the subband occupation of InAs quantum

dots on a delta-doped GaAsSb barrier," *Journal of Applied Physics*, vol. 109, p. 014312, 2011.

[122] C.H. Chan, H.S. Chen, C.W. Kao, H.P. Hsu, Y.S. Huang, and J.S. Wang, "Investigation of multilayer electronic vertically coupled InAs/GaAs quantum dot structures using surface photovoltage spectroscopy," *Applied Physics Letters*, vol. 89, p. 022114, 2006.

[123] A. Marti, L. Cuadra, and A. Luque, " quantum dot intermediate band solar cell," *twenty-eighth IEEE Photovoltaic Specialists Conference*, Anchorage, AK, USA, pp. 940-943, 2000.

[124] N Lǒpez, A. Martí, A. Luque, C. Stanley, C. Farmer, P. Diaz, "Experimental analysis of the operation of quantum dot intermediate band solar cells," *Journal of Solar Energy Engineering*, vol. 129, pp. 319-322, 2007.

[125] Y. Okada, R. Oshima, and A. Takata, "Characteristics of InAs/GaNAs strain-compensated quantum dot solar cell," *Journal of Applied Physics*, vol. 106, p. 024306, 2009.

[126] G. Jolley, H.F. Lu, L. Fu, H.H. Tan, and C. Jagadish, "Electron-hole recombination properties of $In_{0.5}Ga_{0.5}As$/GaAs quantum dot solar cells and the influence on the open circuit voltage," *Applied Physics Letters*, vol. 97, p. 123505, 2010.

[127] D. Alonso-Álvarez, A. G. Taboada, J.M Ripalda, B. Alén, Y. González, L. González, J.M García,, F Briones, A. Martí, A. Luque, A.M. Sánchez, and S.I. Molina, "Carier recombination effect in strain compensated quantum dot stacks embedded in solar cell," *Applied Physics Letters*, vol 93, 123114, 2008.

[128] S.M. Hubbard, C.D Cress, C.G. Bailey, R.P. Raffaelle, S.G. Bailey, and D.M Wilt, " Effect of strain compensation on quantum dot enhanced GaAs solar cells," *Applied Physics Letters* vol. 92, 123512, 2008.

[129] Voicu Popescu, Gabriel Bester, Mark C. Hanna, Andrew G. Norman, and Alex Zunger, "Theoretical and experimental examination of the intermediate-band concept for strain-balanced (In, Ga) As/Ga (As, P) quantum dot solar cell," *Physical review B* Vol. 78, 205321, 2008.

[130] P. Harrison, *Quantum Wells, Wires and Dots*. Chihester, UK, John Wiley & Sons, Ltd, 2005.

[131] A. Marti, E. Antolin, C. R. Stanley, C. D. Farmer, N. Lopez, P. Diaz, E. Canovas, P.G. Linares, and A. Luque, "Production of photocurrent due to

intermediate-to-conduction-band transitions: a demonstration of a key operating principle of the intermediate-band solar cell," *Physical Review Letters*, vol. 97, no. 24, pp. 247701-1, 2006.

[132] Masakazu Sugiyama, Yunpeng Wang, Kentaroh Watanabe, Takayuki Morioka, Yoshitaka Okada, Yoshiaki Nakano, "Photocurrent generation by two-step photon absorption with quantum well superlattice cell," *37th IEEE photovoltaic specialists conference*, Seattle, WA, June 19-24, 2011.

[133] D. Bimberg, M. Grundmann, N. N. Ledentsov *Quantum Dot Heterostructures*, New York, Wiley, 1999.

[134] A. Rastelli, M. Kummer, H. von Kanel, "Reversible shape evolution of Ge islands on Si (001)," *Physical Review Letters*, vol 87(25), p.256101, 2001.

[135] C.G.Van de Walle, "Band lineups and deformation potentials in the model-solid theory," *Physical Review B*, vol. 39,p.1871, 1989.

[136] A.M. Noori, R.S. Sandhu, S.L.Hayashi, E.D. Meserole, V. Hardev, A. Cavus, M. Lange, C. Monier, R. Hsing, D. Sawdai, M.Wojtowicz, T.R. Block, A. Gutierrez-Aitken and M.S. Goorsky, "Strain relaxation and surface roughness of $In_xAl_{1-x}As$ graded buffer layers grown on InP for 6.05 Å applications," *Journal of Vacuum Science & Technology B*, vol.22(5), pp.2303-2308(2004).

[137] Lin-Wang Wang, Jeongnim Kim, and Alex Zunger, "Electronic structures of [110]-faceted self-assembled pyramidal InAs/GaAs quantum dots," *Physical Review B* vol 59, p. 5678, 1999.

[138] Fermi golden rule for rate of transitions:

$$W = \frac{2\pi}{\hbar}\left|\left\langle f\left|H'(r)\right|i\right\rangle\right|^2 \delta\left(E_i - E_f - \hbar\omega\right)$$

$$\frac{1}{\tau} = W = \frac{2\pi}{\hbar}\left|\left\langle f\left|H'(r)\right|i\right\rangle\right|^2 \delta\left(E_i - E_f - \hbar\omega\right).$$

[139] W. A. Harrison, "Elementary theory of heterojunctions," *Journal of Vacuum Science and Technology*, vol. 14, no. 4, p. 1016, 1977.

[140] J. Tersoff, "Theory of semiconductor heterojunctions: The role of quantum dipoles," *Physical Review B*, vol. 30, no. 8, p. 4874, 1984.

[141] C. G. Van de Walle and R. M. Martin, "Theoretical study of band offsets at semiconductor interfaces," *Physical Review B*, vol. 35, no. 15, p. 8154, 1987.

[142] C. W. Snyder, J. F. Mansfield, and B. G. Orr, " Kinetically controlled critical thickness for coherent islanding and thick highly strained pseudomorphic films of $In_xGa_{1-x}As$ on GaAs(100)," *Physical Rev. B* vol 46, p. 9551, 1992.

[143] K. Kamath, P. Bhattacharya, and J. Phillips, "Room temperature luminescence from self-organized quantum dots with high size uniformity," *Journal of Crystal Growth*, vol. 175-176, pp. 720-724, 1997.

[144] R. Leon, S. Fafard, D. Leonard, J.L. Merz, and P.M. Petroff, "Visible luminescence from semiconductor quantum dots in large ensembles," *Applied Physics Letters*, vol. 67, p. 521, 1995.

[145] M.Y Levy and C. Honsberg, "Nanostructured absorbers for multiple transitions solar cells," *IEEE Transaction on electron devices*, vol. 55, pp. 706-711, 2008.

[146] S.P. Bremner, M.Y. Levy, and C.B. Honsberg, "Limiting efficiency of an intermediate band solar cell under a terrestrial spectrum," *Applied Physics Letters*, vol. 92, p. 171110, 2008.

[147] S.Fuchi, S .Miyake, S, Kawarura, W.S. Lee, T. Ujihara and Y. Takeda, "Effects of absorbed group-V atoms on the size distribution and optical properties of InAsP quantum dots fabricated by droplet hetero-epitaxy," *Journal of Crystal Growth*, vol.310, pp.2239-2243, 2008.

[148] E. Ribeiro, R.L. Maltez, W. Carvalho, Jr., D. Ugarte, and G. Medeiros-Ribeiro, "Optical and structural properties of InAsP ternary self-assembled quantum dots embedded in GaAs," *Applied Physics Letters*, vol. 81, pp.2953-2955, 2002.

[149] Y. Qiu and D. Uhl, "Self-Assembled InAsSb quantum dots on (001) InP substrates," *Applied Physics Letters*; vol. 84, pp. 1510-1512, 2004.

[150] D. Drews, A. Schneider, T .Werninghaus, A. Behres, M .Heuken, K. Heime, D.R.T .Zahn, "Characterization of MOVPE grown InPSb/InAs heterostructures," *Applied Surface Science*; vol.123/124 pp.746-750, 1998.

[151] M. Heuken, C. V. Eichel-Streiber, A. Behres, B. Schineller, K. Heime, C. Mendorf, G. Brockt and H. Lanker, "MOVPE growth of InPSb/InAs heterostructures for mid-infrared emitters," *Journal of Electronic Materials*; Vol. 26**,** pp.1221-1224, 1997.

[152] F.A. Zhao, Y.H. Chen, X.L. Ye, P. Jin, B. Xu, Z.G. Wang, and C.L. Zhang, "Growth of nanostructures on composition-modulated InAlAs surfaces," *Journal of Physics: Condensed Matter*, vol. 16, pp. 7603-7610, 2004.

[153] J. Brault, M. Gendry, G. Grenet, G. Hollinger, Y. Desières, and T. Benyattou, "Role of buffer surface morphology and alloying effects on the properties of InAs nanostructures grown on InP(001)," *Applied Physics Letters*, vol. 73, p. 2932, 1998.

[154] J. Brault, M. Gendry, G. Grenet, G. Hollinger, J. Olivares, B. Salem, T. Benyattou, and G. Bremond, "Surface effects on shape, self-organization and photoluminescence of InAs islands grown on InAlAs/InP(001)," *Journal of Applied Physics*, vol. 92, p. 506, 2002.

APPENDIX A

EXPRESSIONS FOR THE STRESS FIELD OF PYRAMID SHAPED QUANTUM DOT WITH ARBITRARY DEGREE OF TRUNCATION IN AN INFINITE MATRIX

The integration of integral (2.22) in section 2.2 can be expressed analytically in the simplified form. As mentioned in section 2.4 and shown in figure 2.4 the origin of the coordinate system is assumed to be center of thee base of the pyramid and the z-axis is the growth direction. The stress component σ_{xx} is expressed as,

$$\sigma_{xx} = -4\pi\Lambda\chi + \Lambda \sum_{\substack{p=\pm1 \\ q=\pm1 \\ n=2,3}} H_1(-1)^n \left\{ aB\ln\gamma - hq \ \arctan\left[\frac{\beta_{xx}}{\alpha_{xx}}\right] + \frac{aq}{2}\ln\left[\alpha_{xx}^2 + \beta_{xx}^2\right]\right\} \quad \text{(A.1)}$$

In equation (A1), $\Lambda = \dfrac{\varepsilon_0 E}{4\pi(1-\nu)}$, with ε_0 as the isotropic misfit strain, E as Young's modulus and ν as Poisson ratio. Equation (A 1), written in compact form, has eightfold summation with p, q and n. the quantities in (A1) are:

$$\alpha_{xx} = \frac{X_n C_{xx} + Z_n D_{xx}}{X_n^2 + Z_n^2}, \quad \beta_{xx} = p\frac{Z_n C_{xx} + X_n D_{xx}}{X_n^2 + Z_n^2}, \quad H_1 = \frac{h}{a^2 + h^2},$$

$$\gamma = -paX_n - qBY_n - \frac{hZ_n}{\sqrt{a^2 + b^2 + h^2}} + S, \quad S = \sqrt{X_n^2 + Y_n^2 + Z_n^2},$$

$$A = \frac{a}{\sqrt{a^2 + b^2 + h^2}}, \qquad B = \frac{b}{\sqrt{a^2 + b^2 + h^2}},$$

$$C_{xx} = X_1 X_n + Y_1\left(Y_n + S\right), \qquad D_{xx} = X_1 Z_n + \left(\frac{qbx - pay}{h}\right)\left(Y_n + S\right);$$

$$X_1 = x + pa\left(1 - \frac{z}{h}\right), \quad X_2 = x + pa(1-f), \quad \mathrm{X}_3 = x + pa,$$

$$Y_1 = y + qb\left(1 - \frac{z}{h}\right), \quad Y_2 = y + qb(1-f), \quad Y_3 = y + qb,$$

$$Z_2 = z - hf, \quad \mathrm{Z}_3 = z,$$

Similarly , the expressions for sigma σ_{yy} can be written as,

$$\sigma_{yy} = -4\pi\Lambda\chi + \Lambda \sum_{\substack{p=\pm1 \\ q=\pm1 \\ n=2,3}} H_2(-1)^n \left\{ bA\ln\gamma - hq \ \arctan\left[\frac{\beta_{yy}}{\alpha_{yy}}\right] + \frac{b}{2}\ln\left[\alpha_{yy}^2 + \beta_{yy}^2\right]\right\}, \qquad \text{(A.2)}$$

With,

$$\alpha_{yy} = \frac{Y_n C_{yy} + Z_n D_{yy}}{Y_n^2 + Z_n^2}, \quad \beta_{yy} = \frac{Z_n C_{yy} - X_n D_{yy}}{X_n^2 + Z_n^2}, \quad H_2 = \frac{h}{b^2 + h^2},$$

$$C_{yy} = Y_1 Y_n + X_1\left(X_n + pS\right), \qquad D_{yy} = Y_1 Z_n + \left(\frac{qbx - pay}{h}\right)\left(X_n + pS\right);$$

The other component of plane stress, σ_{zz} is obtained from the expression of hydrostatic stress as,

$$\sigma_{xx} + \sigma_{yy} + \sigma_{zz} = 8\pi\Lambda\chi \qquad \text{(A.3)}$$

The components of shear stress σ_{ij} (i≠ j) are expressed following

$$\sigma_{xy} = \Lambda \sum_{\substack{p=\pm1 \\ q=\pm1 \\ n=2,3}} \frac{pqh}{\sqrt{a^2 + b^2 + h^2}} (-1)^n \ln(\gamma) \qquad \text{(A.4)}$$

$$\sigma_{yz} = -\Lambda \sum_{\substack{p=\pm1 \\ q=\pm1 \\ n=2,3}} H_2(-1)^n \left\{ qhA\ln(\gamma) + b\arctan\left[\frac{\beta_{yz}}{\alpha_{yz}}\right] + \frac{hq}{2}\ln\left[\alpha_{yx}^2 + \beta_{yz}^2\right]\right\}, \qquad \text{(A.5)}$$

$$\sigma_{xz} = \Lambda \sum_{\substack{p=\pm1 \\ q=\pm1 \\ n=2,3}} H_1(-1)^n \left\{ hB\ln(\gamma) + a\arctan\left[\frac{\beta_{xz}}{\alpha_{xz}}\right] - \frac{h}{2}\ln\left[\alpha_{xz}^2 + \beta_{xz}^2\right]\right\}, \qquad \text{(A.6)}$$

In equation (A.4), (A.5) and (A.6), the expressions on the right hand side are given by,

$$\alpha_{yz} = \frac{Y_n C_{yz} + Z_n D_{yz}}{Y_n^2 + Z_n^2}, \qquad \beta_{yz} = \frac{Z_n C_{yz} - X_n D_{yz}}{X_n^2 + Z_n^2},$$

$$C_{yz} = Y_1 Y_n + X_1 \left(X_n + pS \right), \qquad D_{yz} = Y_1 Z_n - \left(\frac{qbx - pay}{h} \right) \left(X_n + pS \right);$$

$$\alpha_{xz} = \frac{Y_n C_{xz} + Z_n D_{xz}}{Y_n^2 + Z_n^2}, \qquad \beta_{xz} = -p \frac{Z_n C_{xz} - X_n D_{xz}}{X_n^2 + Z_n^2},$$

$$C_{xz} = X_1 X_n + Y_1 \left(Y_n - qS \right), \qquad D_{xz} = X_1 Z_n + \left(\frac{qbx - pay}{h} \right) \left(Y_n - qS \right);$$

The expressions for stress from (A.1) to (A.6) are used to calculate the stress distribution due to lattice mismatch in section 2.4 and 2.5 of this dissertation.